The Dissertation Committee for Ping-Hsiang Su certifies that this is the approved version of the following dissertation:

Exploring Novel Properties of Atomically Smooth Metal Films as an Ideal Platform for Nano Photonics

Committee:

Chih-Kang Shih, Supervisor

Alejandro de Lozanne

Alexander Demkov

Xiaoqin Li

Edward T. Yu

Exploring Novel Properties of Atomically Smooth Metal Films as an Ideal Platform for Nano Photonics

by

Ping-Hsiang Su, B.S.

Dissertation

Presented to the Faculty of the Graduate School of

The University of Texas at Austin

in Partial Fulfillment

of the Requirements

for the Degree of

Doctor of Philosophy

The University of Texas at Austin

December, 2016

Dedicated to My Family,

My Father Wu-Jung Su, My Mother Chiu-Chu Wu,

My Brother Kuan-Ming Su, and My Sister Ching-Ting Su

My Heart is with Them

A shooting star,

A clouding of the sight,

A lamp, an illusion, a drop of dew, a bubble, a dream,

A lightning's flash

A thunder cloud

This is the way one shall see the conditioned

Diamond Sutra

Acknowledgements

First of all I am going to thank my supervisor, Professor Chih-Kang Shih. I am so grateful that Dr. Shih gave me the opportunity to work on important projects exploring the beauty of thin film growth and its applications in plasmonics. A lot of time I made awful mistakes and felt too intimidated to go on with my project but Dr. Shih always finds the best way to encourage me. He tried so hard to tailor the research project best suited to my capability but still bearing equal significance as other important projects in the lab. I am not only gaining good training in the profession, but also learning from him the gumption and passion as an experimentalist who always aims, fearlessly, to attack the most difficult subjects with realistic and promising methods to crack them.

I will thank my dissertation committee members, Dr. Alejandro de Lozanne, Dr. Alexander Demkov, Dr. Xiaoqin Li, and Dr. Edward T. Yu. They are brilliant scientists. They gave me very valuable advice and discussed with me potential development for the future research based on my study I reported in the defense talk. I am also grateful that they spent precious time reading my dissertation.

I owe a lot to former lab members, Dr. Jisun Kim, Dr. Huan Li, Dr. Christopher W. Mann, Dr. Charlotte E. Sanders, and Dr. Chendong Zhang. When I was junior in the lab with no idea about ultra high vacuum (UHV) systems, Jisun was the first one who taught me UHV101 with her great patience and friendliness. Chris and Charlotte, with all their warmth and sincerity, gave me very valuable advice about future career. Charlotte also helped me revise my resume and curriculum vitae to make them look more professional. I will express special thanks to Chengdong "Chad" Zhang. Chad is my mentor in the lab, introducing me into the beautiful world of thin film studies and training me on all important techniques about UHV and molecular beam epitaxy thin film growth. He is always very patient and very friendly, and is always prepared to assist me any time I make mis-

takes or mess up with the machine. I can always find support from him every time I struggle with my inexperience and poor experimental skills.

I will thank current lab members, Dr. Fei Cheng, Dr. Hyoungdo Nam, Dr. Yutsung Tsai, Dr. Siyuan Zhu, Yuxuan Chen, Matthew Dwyer, Madisen Holbrook, Alexander Johnson, and Qiang Zhang. I worked very closely with Fei. Fei helped me realize important applications in plasmonics of my high-quality metal films. Hyoungdo is a very good practitioner of scanning tunneling microscopy. He is very friendly and gives me very helpful advice on scientific instrument design and experimental skills. We also worked very closely on the project of aluminum (Al) thin film superconductivity study. I am very happy to work with Qiang. He is very friendly all the time even if he is under great pressure with his project. He helped me realize the new method of thick silver (Ag) film growth with post-growth annealing at elevated temperature. I worked with him very comfortably. Particularly, I am going to thank Alex Johnson. We are very close friends in the lab. It is the best moment in the lab every time I chatted with Alex while temporarily escaping from my stressful work. We talked diversified issues, from research to sexism to same sex marriage. We shared experience of each other's life. We crossed the barrier of culture difference and genuinely embraced each other's life stories. My English also gets tremendous progress. It is the gift he gave me from our invaluable friendship.

I will thank Dr. Xiaoqin Li and her group, especially Thomas Hartsfield and Junho Choi. They are very close collaborators. Tom demonstrated that our atomically smooth Ag films are superb for quantum dot applications and Junho helped us measure intrinsic optical constants of our high-quality Al films. It is these newly measured data which give the study high impact.

I am going to thank all staff members in the machine shop, especially Allan Schroeder and Jack Clifford. They are always very friendly and very willing to help stu-

dents deal with difficult situations about scientific instruments. Without them I cannot fix a lot of troubles I encountered in my machine.

I will thank my friends in Taiwan, especially Sheng-Wei Huang and Tsung-Cheng Tsai. We are friends for more than a decade. Every time when I feel so upset, they always give me the warmest support from Taiwan. Distance is definitely not able to lessen our friendship.

Finally, also the most importantly, I will thank my family. My Father and Mother, and my younger brother and sister. My parents worked hard to give children the best and warmest family. I grew up with best ever childhood. My parents always encourage us children to pursue our dreams, and never fail to dream big in life. They gave us freedom to do whatever we like to try. They accompanied children through the roughest years of restive teenage ages with their endless love, patience, and wisdom. I thank my siblings. We grew up together. We have the best memories with each other of our breezy, carefree, sweet and blessed childhood. I can never give enough thanks to my parents. If I achieve anything, it is because of them. This dissertation is dedicated to my family, my beloved Father and Mother, brother and sister.

PING-HSIANG SU

The University of Texas at Austin

Nov. 2016, Thanksgiving

Exploring Novel Properties of Atomically Smooth Metal Films as an Ideal Platform for Nano Photonics

Ping-Hsiang Su, Ph.D.

The University of Texas at Austin, 2016

Supervisor: Chih-Kang Shih

Plasmonics is the science of manipulating light at the metal and dielectric interface. Therefore, a high-quality metal film plays a critical role in this exciting frontier of research. Among available plasmonic metals, silver (Ag) and aluminum (Al) is of particular interest. Ag is a widely used plasmonic material because of its intrinsic low loss. However, conventional thermal Ag films usually show rough surfaces (root-mean-square roughness is as large as several nanometers) and polycrystalline structures with grain boundaries. These features lead to significant plasmonic loss. Preparing an atomically smooth epitaxial Ag film is thus a very critical step in the developement of plasmonics. However, due to the pinning of grain boundaries by contaminants and the propensity to dewetting from commonly used semiconductor substrates (such as Si and GaAs), Ag is a very unforgiving material in the perspective of film growth. In this dissertation we are going to report novel methods to overcome these difficulties and realize the epitaxial growth of atomically smooth Ag films on Si(111). We will show that our films possess excellent optical properties with extraordinarily low loss. The significantly narrow distribution of the lifetime of giant quantum dots placed on our Ag film is another demonstration that our films perfectly apply to, and thus facilitate, the research in plasmonics and quantum photonics.

In recent years Al is demonstrated to be an excellent platform for ultraviolet (UV) plasmonics. However, Al is highly reactive with oxygen and can be rapidly oxidized once exposed to even a low partial pressure of oxygen (10^{-8} Torr). Therefore it will be very challenging to prepare high-purity Al films. In this dissertation we are going to demonstrate the epitaxial growth of high-purity, atomically smooth Al films on Si(111) with different growth methods accompanied by an optimally controlled, ultraclean method of oxidation. Our epitaxial Al films demonstrate considerable loss reduction in the UV spectral range, in comparison to the polycrystalline Al films. These high-quality epitaxial Al films provide an ideal platform for UV plasmonics. Moreover, the availability of newly-obtained intrinsic optical constants on our single-crystalline Al films from the spectroscopic ellipsometry measurement enables a more accurate theoretical prediction in the design of nano-plasmonic devices.

Table of Contents

List of Tables

List of Figures

Chapter 1: Molecular Beam Epitaxy (MBE) - Background and Review

1.1 Introduction

Molecular beam epitaxy (MBE) is an epitaxial method for thin-film deposition of single crystals. The invention of MBE was closely related to the development of semiconductor devices since these devices were highly critically dependent on the growth of very perfect and extremely pure semiconductor crystals. Because of its operation in an extremely clean environment (ultrahigh vacuum, UHV) with highly pure, controllable atomic or molecular beam flux, MBE provides a superior solution to preparing such a high-quality semiconductor thin films. [1 - 6]

"Epitaxy" refers to the growth of a crystalline overlayer (film) on a crystalline substrate. In other words, if the film has a crystalline structure that is ordered with respect to the crystalline structure of the underlying substrate, it is considered as an "epitaxial" film. An epitaxial film can be grown on a substrate of the same material, which is called "homoepitaxy." If the film is grown on a substrate of a different material, the growth of such a film is called "heteroepitaxial growth".

MBE growth can be simply imagined as "spray painting" the substrate with vapors of atoms or molecules. The growth of semiconductor thin films from the vapor source was not a new idea, but prior to 1970s films prepared by such a method suffered from ill quality such as highly polycrystalline or ill-ordered structures. Not until late 1960s did the growth of expitaxial compound semiconductor thin films be realized. [1 - 6] Since then MBE continued its tremendous development to growing a wide variety of materials, including metals, graphene and topological insulators, to name a few, on myriads of crystalline metal or semiconductor substrates. [7] Nowadays, MBE is employed to

grow not only thin films, but a number of nano-structures such as nanowires [8] and quantum dots [9 - 11].

Basically, MBE involves evaporating the source material into a vapor of atomic or molecular beam in a UHV chamber (10^{-9} - 10^{-11} Torr) while the substrate is placed in the path of the beam for the source material to deposit onto the substrate surface. In the UHV environment the beam atoms or molecules travel in a nearly collision-free path until arriving either at the substrate surface or the chamber wall. Because of this nearly collision-free steady flux of the source material, the deposition rate can be precisely controlled. The UHV environment also provides another essential advantage to MBE growth - minimization of contamination of the growth surface.

In a typical MBE operation, the start or stop of growth can be easily controlled by opening or closing a shutter which is interposed in the path of the beam. Since the time to grow a single layer of atoms or molecules (a monolayer, ML) is typically much longer than the time to open or close the shutter, the growth of a film can be precisely controlled to be within the range of a single layer. With the suitable choice of the substrate material, the proper preparation and cleaning of the substrate prior to growth, and appropriate controlling of the substrate temperature (which will be called "growth temperature" alternately in this dissertation), the film grown on the substrate can crystallize (therefore, the so-called "epitaxial growth"). Moreover, the growth in an UHV environment from a clean source on a well-prepared substrate assures the atomically sharp and clean interface between the substrate and the film, if there are no chemical reactions or intermixing between substrate atoms and source atoms/molecules.

Before concluding this section, it is worthwhile emphasizing how important UHV is to the success of MBE growth. [1, 12] First we define the impinging rate $\dot{z}$ (unit: $cm^{-2}s^{-1}$)

as the number of residual gas particles hitting on a unit area (1 cm^2) per second. The relationship between $\dot{z}$ and the vacuum pressure P is:

$$\dot{z} = \frac{P}{\sqrt{2\pi m k_B T}} \tag{1.1}$$

where m is the atomic mass of the gas particles, T is the temperature in Kelvin (K) and k_B the Boltzmann constant. If the vacuum pressure is measured in Torr and atomic mass m is converted to molecular weight M in grams, Eq. (1.1) can be written as

$$\dot{z} = 3.5 \times 10^{22} \frac{P(Torr)}{\sqrt{MT}} \quad cm^{-2}s^{-1} \tag{1.2}$$

For air at 300 K, the gas arrival rate is about $(3.8 \times 10^{20}) \times P$ (in Torr) $cm^{-2}s^{-1}$. For a pressure of 10^{-6} Torr the arrival rate is 3.8×10^{14} $cm^{-2}s^{-1}$. The number of atoms in a cm^2 of the cube face of Si is about 3.2×10^{14}. Thus the number of atoms arriving in a second at 10^{-6} Torr is almost the same as the number of Si atoms occupying a surface of 1 cm^2! Here we define 1 Langmuir (1 L) as the dosage corresponding to the exposure to a gas pressure of 10^{-6} Torr for one second. If the sticking coefficient of a gas species to a surface is unity, 1 L exposure to the gas will produce a coverage of about one monolayer! It shows how quickly the surface can get contaminated. Even for a good UHV in the order of 10^{-10} Torr, a clean surface can be badly contaminated just in a few hours. Therefore a qualified surface scientist should always try his/her best to prepare a vacuum which can reach 10^{-11} Torr or even 10^{-12} Torr.

1.2 Review of Atomically Flat Silver Film Growth

An important reason for us to search for novel growth methods to prepare single-crystalline metal films with atomic flatness is for applications in the exciting research field of plamonics and nano-photonics. As will be explained in detail in Chapter 2, a

highly pure, single-crystalline metal film with atomic smoothness is key to the successful development of plasmonic nano-devices. Silver (Ag) is extensively used in this field because of its low-loss property in the regime of infrared and visible light. Study of Ag films on semiconductor substrate was a hot subject of research for decades because of its compatibility with the long-established capability of device manufacturing in semiconductor industry. In this section I am going to review growth mechanism of Ag uncovered by decades of endeavor of surface scientists.

1.2.1 *Growth Mechanism in a Nutshell*

Descriptions of growth mechanisms are largely based on the terrace-step-kink (TSK) model of a surface (see **Fig. 1.1**). [13] *Terraces* represent portions of low-index planes. Terraces are separated by *steps*. An *adatom* is an atom adsorbed on the surface. A *vacancy* is a defect on the terrace where a terrace atom disappears. A *kink* is a portion of the step which is not straight, but cornered. An *island* is the agglomeration of atoms on a terrace. These terms will be used repetitively in this dissertation.

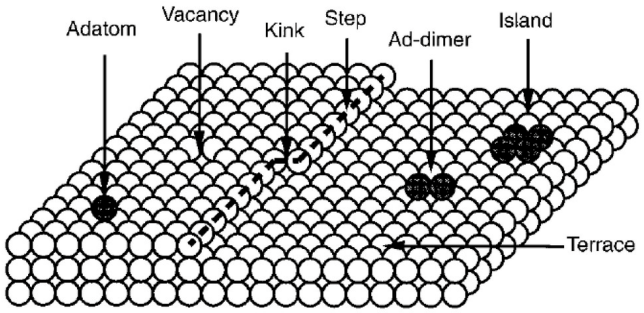

Figure 1.1 From [13]. The TSK model of a surface defined for a simple cubic crystal. White balls represent atoms of the substrate. The dashed line indicates a step separating the upper and lower terraces. Black balls represent adatoms adsorbed on the surface.

The film growth can be categorized into 3 modes: (1) Frank-van der Merve (FM) mode, (2) Vollmer-Weber (VW) mode, and (3) Stransky-Krastanov (SK) mode. See **Fig. 1.2**.

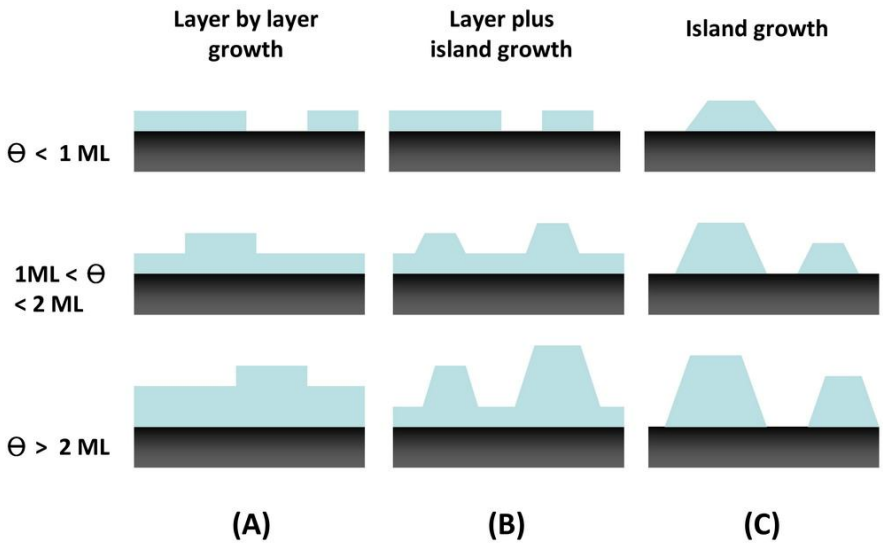

Figure 1.2 Schematics of three different growth modes of a thin film. **(A)** Frank-van der Merve (FM). **(B)** Stranski-Krastanov (SK). **(C)** Vollmer-Weber (VW).

In the FM mode, the film is grown in a layer-by-layer fashion, *i.e.*, a layer will be completed before the start of the growth of the next layer. In the FM mode the interaction between the substrate and adatoms is stronger than between neighboring adatoms. Due to the desirability of flat films, researchers designed different methods in order to achieve the growth following the FM mode, in which the two-dimensional (2D) film can be realized.

The VW mode is the opposite to the FM mode. In the VW mode, the interaction between neighboring adatoms is stronger than the interaction between substrate and adatoms, which will lead to growth of three-dimensional (3D) adatom clusters or islands.

The film formed in the VW mode will show a rough surface with multi-layer islands and the bare substrate is exposed between islands. This growth phenomenon is described as "non-wetting" since the film does not fully cover, in a sense, "wet" the substrate. Ag grown on GaAs(110) at room temperature (RT) follows this mode since Ag is non-wetting on GaAs(110). [14]

The SK mode is an intermediary process between the FM mode and VM mode. It is characterized by initial 2D layer growth followed by 3D island formation. In this mode, first, one or several complete monolayers will form on the substrate. But the growth is followed by 3D islands appearing on top of the first full layer(s). Ag deposited on Si(111) at RT or higher temperatures follows this mode. [15, 16] An important factor leading to the SK mode of Ag growth on Si(111) is the lattice mismatch between Ag and Si, as will be discussed below.

For heteroepitaxial growth, lattice match is one of the most important factors that determine whether a particular epitaxial structure can be grown on a specific substrate and which growth mode to follow. If lattice mismatch happens, there will be two possible consequences: (1) Strain will be induced in the overlayer lattice structure. Or (2) the lattice mismatch will be adjusted by interface dislocations while the overlayer structure suffers no strain. [12] Since the system we encountered the most will belong to case (1), I will continue the discussion when there is strain in the overlayer due to lattice mismatch.

According to J. Tersoff and F. K. LeGoues [17], the strained epitaxial layers can relax by two competing mechanisms: (1) Surface becomes rough by the formation of islands and/or pits. (2) The strain relieves by nucleation of dislocations before the surface becomes rough. Their theoretical calculation showed that surface roughening is a thermally activated process, with a barrier which scales with mismatch ε as ε^{-4}. In contrast, the barrier for dislocation formation scales as ε^{-1}. Therefore for a large mismatch, the bar-

rier for surface roughening will drop quickly because of ε^{-4} dependence. This will allow the occurrence of surface roughening. When the mismatch is small, the barrier for dislocations will be smaller than that for surface roughening, so the strain will be relieved by formation of dislocations before surface becomes rough. There is a critical mismatch ε_c at which the barriers for two mechanisms are equal. In other words, when $\varepsilon < \varepsilon_c$, the strain will relax via formation of dislocations and when $\varepsilon > \varepsilon_c$, the surface will become rough in order to relieve the strain.

Several groups showed that Ag deposited on a clean, well-reconstructed Si(111)-(7 × 7) substrate follows the SK mode, in which one-atomic-high wetting layer of Ag will be established at the beginning of growth, followed by islands grown on top of the wetting layer. [15, 16, 18] Ag wetting layer is a mesh-like structure, whose discontinuous character might be effective to completely relieve the strain. But further deposition will make the strain large enough to dramatically reduce the barrier for surface roughening. The consequence is that 3D Ag islands will form on top of the wetting layer to relieve the strain. Pavel Sobotík *et al.* showed by STM images that the island top was atomically flat without dislocations - a manifestation that strain was greatly released in the island. [16] It is debatable how strain was relieved via the island formation. Yiyao Chen *et al.* showed, from their X-ray specular reflectivity measurement, that Ag islands "consume" the wetting layer underneath them, *i.e.* when an Ag island grows on top of the wetting layer, the wetting layer will be transformed to the same face-cubic centered (FCC) structure as the island, which means that the island contacts the substrate directly without the mediation of a wetting layer between them. The Ag island is completely incommesurate with Si substrate and suffers no strain at all. [15]

Lattice mismatch presents a daunting task of preparing a flat film in the heteroepitaxial growth. In the same paper presented by J. Tersoff and F. K. LeGoues, they

offered several considerations to increase ε_c to realize the growth of flat films. [17] First, they proposed, by adding a surfactant can the surface free energy of either an island or a pit be manipulated to increase ε_c. Second, they showed that low temperature typically gives the maximum value of ε_c, while elevated-temperature deposition will usually lead to rough surface because high temperature can significantly reduce the surface free energy of an island or a pit, which favors the development of such rough surface features.

Even for homoepitaxial growth, in which lattice mismatch is eliminated, several factors still hinder the growth of flat films. Consider the formation of a layer in the case of layer-by-layer growth. First, single-layered islands will form on top of a newly grown layer. During the course of growth these islands shall be allowed to grow laterally and coalesce with each other when more and more atoms are deposited onto the surface until, eventually, a complete layer is finished. For such a case to take place, an adatom landed on top of an island needs to move down the island edge (step) to allow the lateral growth of the island. Unfortunately, there exists the step barrier which hinders the mobility of an atom from hopping down the step. Because of the step barrier it is more likely that atoms stay on top of an island and start to nucleate to form new islands before the underlying layer is completed. If the effect of the island-edge barrier is strong, 3D islands or mounds will develop and the growth mode is rough. The so-called "wedding-cake" structure of homoepitaxial Ag on a bulk Ag(111) single crystal is the manifestation of this effect. [18 - 20] Karsten Bromann *et al.* determined the step barrier of Ag on Ag(111) to be 120 ± 15 meV. Interestingly, in the heteroepitaxial growth of Ag on Pt(111) the barrier is much lowered - which is 30 ± 5 meV. [21]

Besides the step barrier, another factor which leads to rough growth, no matter in the homoepitaxial or heteroepitaxial growth, is ripening. In ripening, larger clusters grow

at the expense of smaller ones. Ripening happens mainly because of the increased mobility of atoms in and around an island when the surface temperature is elevated.

Thanks to enormous effort made by hard-working surface scientists, the exploration of growth mechanism as described above led to numerous designs of experimental methods to grow flat thin films. One urgent question raised naturally is: how to overcome the problem of the island-edge barrier? The straightforward solution is by reducing the island-edge barrier. If the barrier cannot be reduced, increasing the frequency of adatoms visiting the island edge by manipulating the island's morphology will be another choice. Consider, if one can grow high densities of small islands at the very beginning of growth, subsequent deposition of atoms on these islands will have more chance to visit the island edge due to the island's small size, and thus a higher probability for an adatom to hop down the island edge. Methods to grow high densities of small islands include lowering the substrate temperature and increasing the deposition rate to avoid island ripening. The other possibility to increase the frequency of adatoms visiting the island edge is by growing the fractal (dendritic) islands. Islands with this shape show a very long periphery and therefore make adatoms more frequent to hit the edge. The growth of dendritic islands can be realized by adding a surfactant [18] or reducing growth temperature [19], for both will lead to a lower mobility of adatoms.

Lowering growth temperature and adding in a surfactant are also effective methods to make the strain more "tolerable" in a heteroepitaxial system by increasing the critical mismatch of the system, ε_c. See the earlier discussion in this section. [17]

Overall, the recipe for the layer-by-layer growth of flat thin films is: (1) Reduction of the growth temperature. (2) High deposition rate. (3) Adding in appropriately chosen surfactants.

From the discussion of the growth mechanism, it is not surprising that Ag on Si(111) grown at RT or higher temperatures follow the SK mode and can never achieve the desired property of atomic smoothness.

1.2.2 *Electronic Growth Mode*

In the previous section we noted that growing films at low temperature is a promising method for flat film growth. But from the application perspective it is not realistic to keep the film at low temperature indefinitely. It is natural to ask what will happen if the film is allowed to warm up to room temperature (RT) after growth at low temperature. This leads to a striking discovery by former lab member Professor Arthur R. Smith and coworkers, published in *Science* in 1996, of growing a genuinely "atomically flat" Ag film on GaAs(110). [14] In this paper Dr. Smith and coworkers showed that the as-deposited (coverage = 15 Å) Ag at 135 K is composed of nanoclusters about 2 to 3 nm in size, which is consistent with the theory of growth mechanism (low mobility of adatoms at a low temperature). Upon subsequent annealing to RT, the film becomes atomically flat with a uniform thickness. **(Fig. 1.3**) The thickness can be determined by measuring the depth of a pit on the surface, which is 15 Å (about 6 ML). Furthermore, the authors found that when the coverage is less than 15 Å, the film will be broken into interconnected pieces with flat tops and a uniform thickness - also 15 Å. When the coverage is more than 15 Å, a universally atomically flat and fully covered overlayer will be achieved, with excess Ag atoms forming single-layer high 2D islands. (**Fig. 1.4**) Here they designated 15 Å (6 ML) as a critical thickness - when the deposition is less than 15 Å the film will be broken to approach this thickness and as the deposition is more than it a (meta)stable, atomic flat and fully covered film will form.

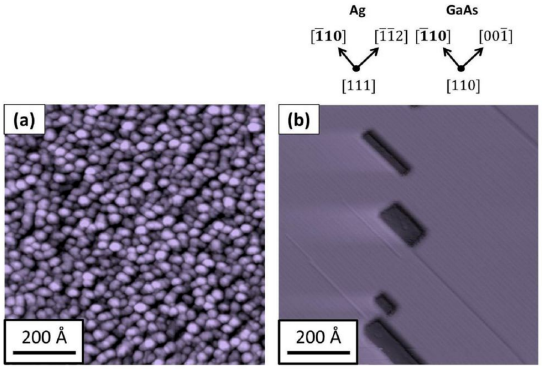

Figure 1.3 From [14]. **(a)** STM topographic image of as-deposited Ag clusters (coverage of 15 Å) on GaAs(110) at 135 K, before annealing. **(b)** STM topographic image showing atomically flat Ag film on GaAs(110) after annealing to room temperature. Square pits (15 Å in depth) in the image are voids extending down to the substrate.

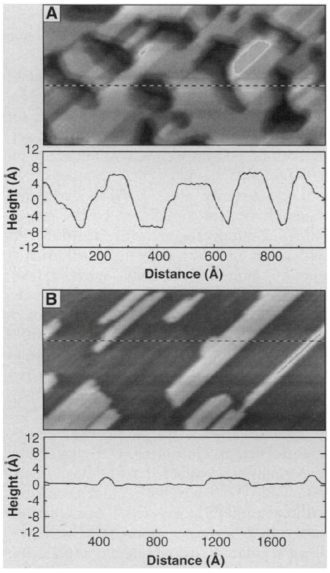

Figure 1.4 From [14]. **(A)** STM image of the morphology of film with coverage of 7.5 Å, which was deposited at 135 K and then annealed to RT. The line profile is along the dotted line. The heights of flat-top mesas are from 11 Å to 15 Å. **(B)** Flat Ag film with coverage of 22.5 Å, deposited at 135 K and annealed to RT. The line profile shows that the height of islands is single-layer.

Strong interest was triggered in theoretical discussion of growth mechanism behind this novel growth method, which does not follow any of the three modes discussed above. There are additional factors aiding in the growth of atomically flat metal films on semiconductor substrates. Zhenyu Zhang *et al*. proposed a new growth mechanism called "electronic growth mode" to explain the experimental results observed by Arthur R. Smith *et al*. [22] In the electronic growth mode, the electronic properties of materials play an important role in determining the film morphology and stability. Two factors play a major role in this model: quantum confinement due to quantum size effect and charge spilling from the metal film to the semiconductor substrate.

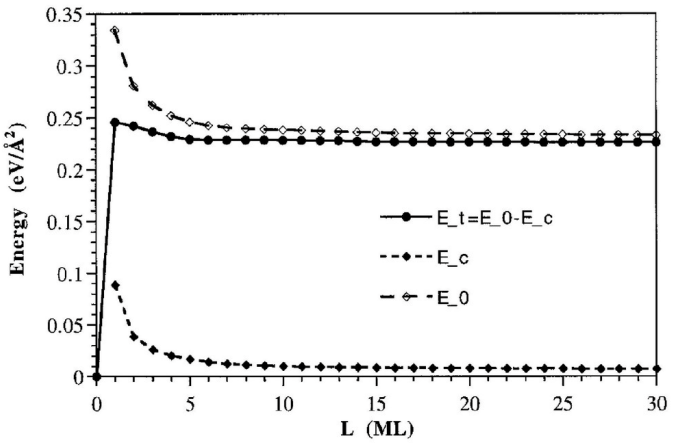

Figure 1.5 From [22]. Film thickness dependence of the film energies for Ag on GaAs(110). The dip at L = 5 ML defines the critical thickness for flat film growth.

Quantum confinement happened on electrons of the metal film which are confined in the direction perpendicular to the surface plane of the film. The confinement is due to the barriers of two interfaces: (1) Interface between the metal film and vacuum, and (2) interface between the metal and semiconductor substrate. In this model the potential bar-

rier of the interface between the film and substrate was treated as an infinite delta function to simplify the calculation. This infinite barrier will be removed when charge spilling is incorporated into the picture. The energy of the film $E_0(L)$ with respect to the film thickness L can be plotted as shown in **Fig. 1.5**. The curve bends up when the film becomes thinner because of the quantum size effect.

Quantum confinement acts as a stabilizing mediator in the thin film to reconcile an effective repulsive force between the film-substrate interface and the film surface. However, as the delta function barrier is removed, electrons spill across the metal-semiconductor interface to lower the system energy. The interface can be modeled as a capacitor, with a layer of negative charge on the semiconductor side and a layer of positive charge on the metal side. The energy lowering due to charge spilling can be estimated as

$$E_c = \frac{1}{2} C V^2 ,$$

which acts to destabilize the flat metal film.

The total energy of the metal film-semiconductor substrate $E_t(L)$ with respect to a film thickness L can be simply calculated as $E_t(L) = E_0(L) + E_c(L)$. **Fig. 1.5** shows the relationship between film energy and film thickness for Ag on GaAs(110). There is a clear dip at L = 5 ML, indicating that a flat film with this thickness is particularly stable. If we define a critical thickness L_c such that the film will be stable if $L \geqq L_c$ while unstable if $L < L_c$, then in Ag-GaAs(110) system L_c is 5 ML. Beyond this thickness the curve is still pretty flat, indicating that the film thicker than 5 ML will all be marginally stable. Despite the simplicity of the theoretical model, its predicted critical thickness is satisfactorily close to the experimental finding of 6 ML, which further corroborates the significance of the electronic contribution in thin film growth.

Although in early studies of quantum size effect (QSE) in thin metal films the pioneering researchers claimed that "it is unlikely that QSE will be observed in a laboratory" because the inclusion of a substrate simply washed out the "confinement" effect, the quantum size effect was manifested in a study of two-step growth by Luca Gvioli *et al*. [23] They showed that at low coverage (1 ML) of deposition of Ag on Si(111), Ag adatoms tended to form isolated islands on the wetting layer with a strongly preferred height (2 ML) and flat tops, rather than pyramid structures (if the growth follows the SK mode). When the coverage increases, such plateaus will extend laterally without changing height. Eventually they will form a percolated network. The preferred height selection can be satisfactorily explained by quantum size effect and charge spilling in the electronic growth mode.

Two-step method can be well described as a method to "circumvent" the kinetic growth following the SK or VW mode and instead, "embrace" the electronic growth mode, which eventually leads to atomically flat metal films.

As a metal film becomes thicker, the quantum size effect will diminish, and the electronic growth mode will thus play a weaker role in determining the morphology of the metal film. In the case of Ag on Si(111), the two-step-grown Ag film will become rougher as the thickness is beyond 20 ML (we will discuss the issue in detail soon). The resultant film morphology is determined by the competition between the electronic growth mode and the necessity to relieve the strain in the film due to lattice mismatch between Ag and Si. As the film grows thicker, the necessity for the film to relieve strain will overcome the electronic preference of drawing the film to a flat morphology by the electronic growth mechanism, thus leading to a rougher surface. This poses a dilemma in applying the two-step method to thick film growth (for most plasmonic films, a thickness at least of 40 nm - 50 nm, *i.e.* thicker than the skin depth of the metal, is required) since

the two-step method fails to promise an atomically smooth growth in the thick film regime. The relevant study about two-step-grown Ag films and other growth methods to prepare thick epitaxial Ag films without losing the desired property of atomic smoothness will be reported in Chapter 4.

1.2.3 *Study of Two-step-grown Ag on Si Substrate*

Because of the success of the two-step method of Ag on GaAs(110), researchers were inspired to explore Ag on different semiconductor substrates by the two-step method. One promising choice is Si(111) because of its intensive use in semiconductor industry and easiness to prepare (simply passing a high current through the wafer in UHV to make an atomically clean 7 × 7 reconstruction surface).

Ag grown on GaAs(110) is a relatively simple system. First, there is no Ag wetting layer on GaAs substrate. Second, the critical thickness of Ag on GaAs(110), which is about 6 ML, can be clearly defined (see discussion above). Ag on Si(111) is a more complicated situation. First, there is a wetting layer of Ag. Second, the critical thickness is harder to determine. It is more likely that there are two critical thicknesses for Ag on Si(111). [24] The first critical thickness is at about 2 ML. Coverage of less than 2 ML will lead to a surface composed of individual islands about 2 ML high (measured from the wetting layer), while coverage of more than 2 ML will give a film with an atomically flat top on the terrace, with pits down to the wetting layer. The film will not fully cover the substrate until the coverage is more than 6 ML. Deposition of more than 6 ML will produce an atomically flat film fully covering the substrate with single-layer islands formed by excess Ag atoms. [24 - 26] Therefore, the second critical thickness comes at 6 ML. Similar phenomena of Ag on Si(100) were also observed. [24]

The characteristic of two critical thicknesses of Ag on Si might originate from the surface states within the band gap of Si, which enhance charge spilling between Ag and Si. The enhancement of charge spilling might modify the total energy curve in the picture of the electronic growth mode to the way which favors two critical thicknesses.

Another important issue about the Ag-Si system is lattice mismatch. The strain on the Ag overlayer due to the lattice mismatch between Ag and Si (about 33 %) is the main reason that Ag on Si follows the SK mode. Even if the two-step method can circumvent this situation, the effect of strain will not be eliminated. Instead, it will lead to the formation of dislocations on the film surface.

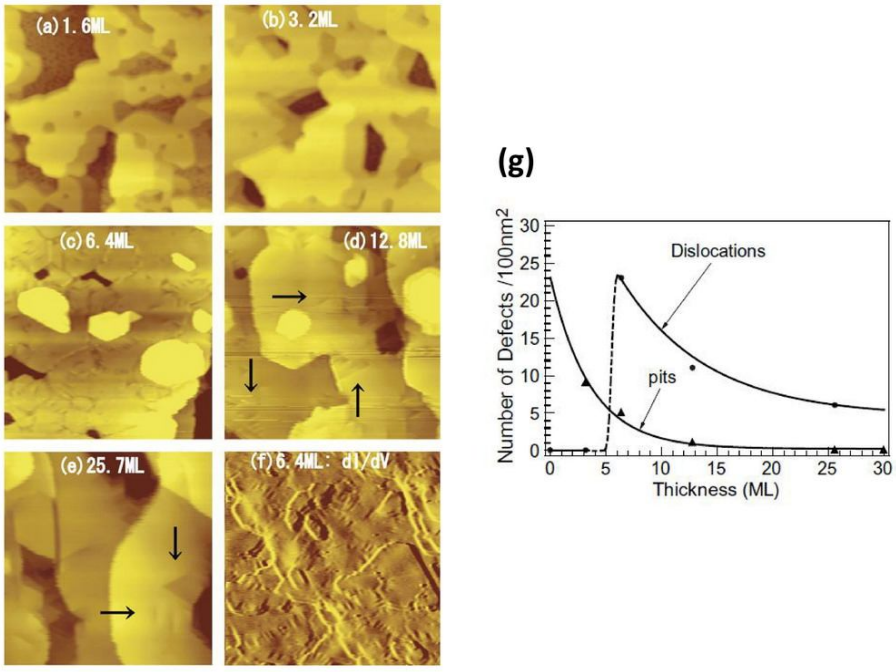

Figure 1.6 From [26]. **(a)** – **(e)** STM images of two-step Ag on Si(111) (deposition at 80 K and annealing to RT). Ag coverages are indicated in each image. Image size: 100 nm × 100 nm. **(f)** d*I*/d*V* image of 6.4 ML Ag by the two-step method. Image size: 100 nm × 100 nm. **(g)** Thickness dependence of pit and dislocation densities on the Ag film by the two-step growth.

Masaru Miyazaki *et al*. studied the growth of Ag with different amounts of coverage on Si(111), and they found an interesting relationship among Ag coverage, the number of pits, and the number of dislocations on the film surface. [26, 27] First, they found that deposition of less than 6 ML will lead to films interrupted by numerous pits extending down to the wetting layer, while the top of the film remains flat without the appearance of dislocations. When the coverage is higher than 6 ML, the film will become atomically flat with a dramatic reduction in the number of pits, but at the same time, shows a multiple of dislocations. More coverage will lead to the reduction of both pits and dislocations but the film quality will degrade too (multi-layer islands pile on the surface), as shown in **Fig. 1.6**.

From these observations the authors conjectured that, when the coverage is less than the critical thickness (6 ML, consistent with the earlier work by C. S. Jiang *et al*.), pits on the film can effectively relieve the strain in the film, while as the coverage approaches the critical thickness, the film will (almost) fully cover the substrate with no or very few pits, as the electronic growth mode predicts, so the strain needs to find other channels to relieve, which leads to the formation of dislocations on the surface. Increasing the coverage more, the electronic effect will weaken and the film will become rougher again (with multi-layer island formation) due to the kinetic mechanism of strain relieve.

In the same paper the authors also showed the influence of growth temperature (substrate temperature during deposition) on the morphology of the film. As shown in **Fig. 1.7**, When the growth temperature increased to 160 K, the film, after annealing to room temperature (RT), became rougher - multiple pits started to show up along the step edge. These pits became larger and more numerous as the growth temperature was elevated further. Eventually, when the film was deposited at RT, the pits joined to form continuous

grooves down to the wetting layer. This series of study again showed the competition between the electronic effect and the kinetic mechanism. As the deposition temperature increases, the thermally driven diffusion and nucleation of Ag atoms will gradually overcome the electronic preference to drive the film to become atomically flat upon annealing - thus leading to the formation of a rough film with deep grooves.

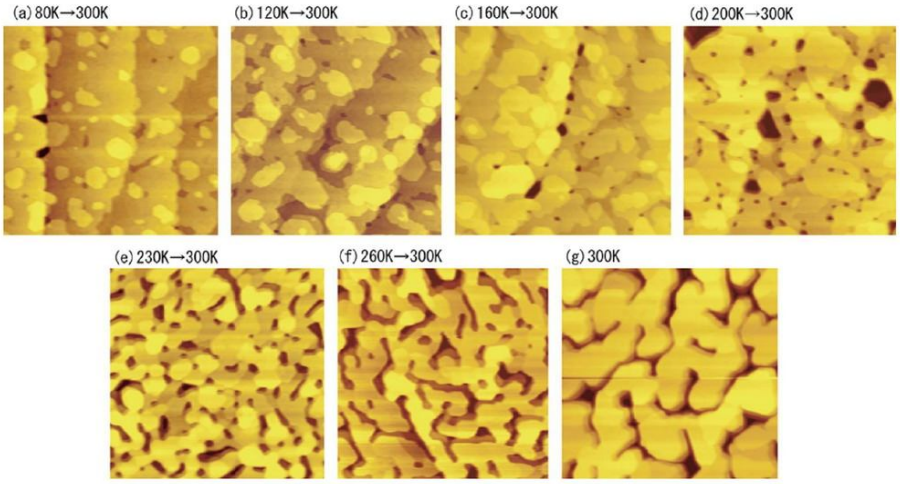

Figure 1.7 From [26]. Deposition temperature-dependent change of two-step grown Ag film on Si(111)-(7 × 7) substrate. Ag coverage is 6.4 ML. The deposition temperature is **(a)** 80 K. **(b)** 120 K. **(c)** 160 K. **(d)** 200 K. **(e)** 230 K. **(f)** 260 K. **(g)** 300 K. Image size: 300 nm × 300 nm.

Before concluding this subsection, we need to point out that conventional metal films prepared by thermal evaporation widely used in the plasmonic community usually show very poor quality - the films are polycrystalline and exhibit very rough surface with irregular grains separated by uneven grain boundaries. High-quality epitaxial metal films with atomic smoothness are thus sorely needed. Furthermore, metal films used in plasmonic research are usually very thick compared with a few monolayers in most two-step-growth studies - at least thicker than 40 nm for most plasmonic metals such as

Ag and Au operated in the visible light wavelength range in order to avoid radiation leakage (which will be discussed in detail in Chapter 2). Two-step growth seems a promising method to prepare atomically smooth films but it cannot guarantee smooth growth as films grow thicker due to diminished quantum size effect. Growing thick, atomically flat epitaxial metal films with good crystallinity can never be an easy job. Once the techniques to grow such high-quality metal films can be harnessed, they will give tremendous contribution to the plasmonic community. My research is mainly about searching for novel methods to realize the growth of thick, atomically smooth epitaxial metal (Ag and Al) films. The results will be reported in Chapter 4 (Ag) and Chapter 6 (Al).

1.3 Review of Atomically Flat Al Film Growth

In recent years aluminum (Al) is the choice for plasmonic applications in the ultraviolet (UV) range of the spectrum (see Chapter 2). To fulfill the potential demand for a premium Al platform in a more and more sought-after research field of Al plasmonics, I was dedicated to the study of epitaxial Al films, which will be reported in detail in Chapter 6. Before concluding this chapter I am going to briefly review the literature of Al growth.

As in the case of Ag, the two-step method can also be applied to Al. Hong Liu *et al.* conducted experiments in which they deposited Al at about 145 K with a very slow deposition rate of 0.17 ML/min onto a clean Si(111)-(7 × 7) reconstructed surface, with subsequent annealing of the film to room temperature. [28] Similar to the behavior of Ag on Si(111) by the two-step process, the growth of Al on Si(111) from a low to higher coverage will show a transition of the surface morphology from the irregular wetting layer to the lateral growth of flat islands with a preferred height, and eventually, to a universally flat 2D film fully covering the surface with single-layer islands on the terrace

formed by extra atoms. (**Fig. 1.8**) The critical thickness is about 5 ML - below which the film shows pits down to the wetting layer and above which the film will (almost) completely cover the substrate with an atomically smooth morphology. Since the lattice constant of Al (4.05 Å) is similar to that of Ag (4.09 Å), and since the Al overlayer formed on top of Si(111) also follows the (111)-(1 × 1) hexagonal close-packed orientation, the same as Ag on Si(111), it is not surprising that Al shows a similar growth behavior and critical thickness to Ag, considering the similar strain Ag and Al overlayers experience on a Si(111) substrate, although the "electronic growth model" introduced in the previous section shall also be incorporated to explain the growth behavior in both cases.

Hong Liu *et al.* also studied the deposition of Al on Si(111)-(7 × 7) at RT (with a coverage of 4 ML). Instead of lateral growth of flat islands with a preferred height, the growth follows the SK mode with the formation of 3D islands separated by deep grooves down to the wetting layer.

In brief, the two-step process still provides the best chance to realize the growth of atomically flat Al films. We will demonstrate in Chapter 6 that by repeated cycles of two-step growth, an atomically-smooth epitaxial Al film as thick as 100 ML can be achieved. However, considering the sophistication of the growth technique and prodigious amount of time required in this method, it is highly desirable to search for a more efficient method to prepare a smooth (if not as good as the two-step-grown film) epitaxial film with good crystallinity. Therefore, drawn on the general theory of growth mechanism discussed in the previous section, we believe that a high deposition rate will be the key to the smooth growth at room temperature (RT) of epitaxial Al films. In Chapter 6 we will demonstrate that RT growth combined with a high deposition rate indeed leads to smooth films (the root-mean-square roughness is comparable to that of two-step-grown films) with good crystallinity (evidenced in the sharp streaks of the RHEED pattern).

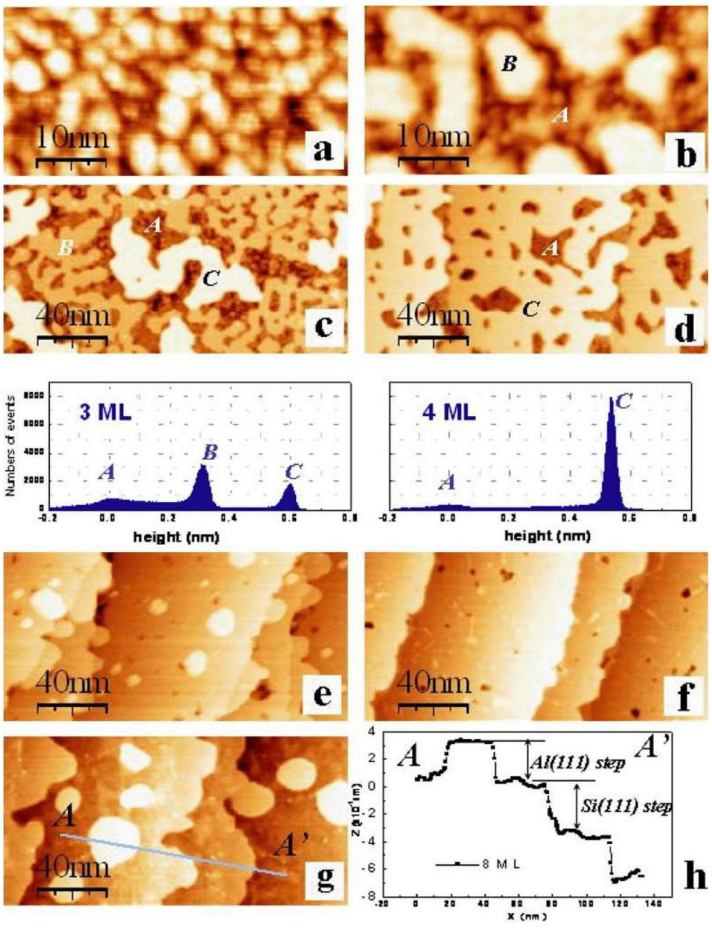

Figure 1.8 From [28]. STM images (at room temperature) for Al films at different coverage: **(a)** 1 ML, **(b)** 2 ML, **(c)** 3 ML, **(d)** 4 ML, **(e)** 5 ML, **(f)** 6 ML, and **(g)** 8 ML. **(b, c)** also include the corresponding height distribution. Peak A, B and C represent the wetting layer, the first Al(111) overlayer and the second Al (111) overlayer, respectively. **(h)** The height profile along the line AA' marked in **(g)**. A step of Si(111) substrate and a monolayer Al(111) are labeled.

Prior to our successful development of epitaxial growth of Al on Si(111), epitaxial growth of Al on GaAs has been achieved by Shi-Wei Lin *et al.* earlier. [29, 30] In their study, Shi-Wei Lin *et al.* deposited 60 nm Al on a clean GaAs(100) (carefully prepared to avoid oxidation) at about 0 °C with a very high deposition rate of 30 Å/min (the base

pressure of the growth chamber is about 3×10^{-10} Torr). The resultant film shows a good crystallinity, manifested in the X-ray diffraction (XRD) analysis in which only a sharp peak of Al(111) appears in the 2θ scanning profile (**Fig. 1.9a**). AFM image of the film shows a flat morphology (the RMS roughness is about 3.6 nm, **Fig. 1.9b**). In comparison, the authors prepared another film in a conventional thermal deposition chamber (base pressure is about 3×10^{-6} Torr) at RT with a very high deposition rate of 120 Å/min. The thermal film was deposited onto an intentionally oxidized GaAs(100) substrate. As expected, the XRD profile of the film shows multiple Al peaks (**Fig. 1.9c**), suggesting that the film is polycrystalline. The AFM image of the polycrystalline film shows a much rougher surface (RMS is 7.5 nm) than the epitaxial film (RMS is 3.6 nm). (**Fig. 1.9d**)

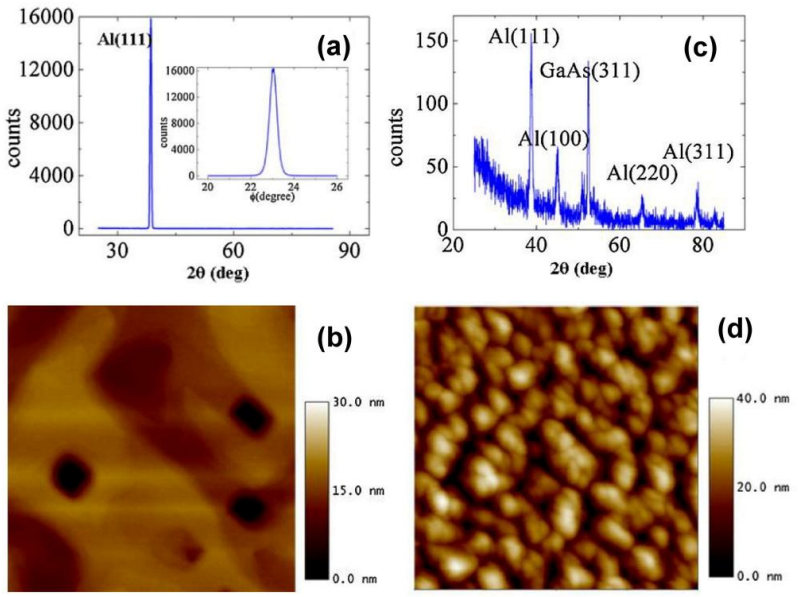

Figure 1.9 From [29]. **(a)** XRD 2θ scanning profile of the epitaxial Al film on GaAs(100). The inset shows the ψ scanning of the Al(111) peak of the same sample. **(b)** AFM image (image size: 1 μm × 1 μm) of the epitaxial Al film. **(c)** XRD 2θ scanning and **(d)** AFM image (image size: 1 μm × 1 μm) of the polycrystalline Al film grown on intentionally-oxidized GaAs(100).

The study demonstrated the importance of a clean, UHV environment and an immaculate, oxide-free substrate in the growth of a smooth epitaxial Al film. In our study, we successfully grew a much smoother Al film (the RMS roughness is an order lower than the epitaxial film from Shi-Wei Lin *et al.*) without resorting to the elaborate two-step method - only one-shot growth at RT with a high deposition rate works the magic. The relevant results will be discussed in Chapter 6.

Chapter 2: Plasmonics - Background and Theory

Plasmonics is a highly active research field in which light is manipulated in a nanostructure via the coupling between light and the surface plasmon of a metal platform. The main purpose of my research is to search for the best of such "platforms" - the single-crystalline and atomically flat metal films. In this chapter I am going to review the background knowledge of plasmonics and explain why finding the best platform is particularly essential in the success of plasmonic devices. I will also illustrate how my research contributes to the community of this exciting new research field.

A grand vision for plasmonics is that it will be the route to the ultimate innovation of nanometer-scale ultrafast circuitry. While modern electronics scales down to a few nanometers, electronic devices are intrinsically limited by the signal speed: Resistive and capacitive delay and dissipative loss make speed higher than GHz difficult to realize. In contrast, photonic devices can easily operate in the THz regime. But due to diffraction limit, the dimensions of such devices are required to be at least the same order of the wavelength in which they operate. Special designs based on unique plasmonic structures can indeed break the diffraction limit, which we will present in more detail in this chapter. As a result, a new generation of circuitry based on plasmonics could combine the advantages of electronics and photonics - the ultrafast operation with nanometer-scale device size can be realized! [31, 32]

2.1 A Beginner's Introduction to Plamonics

Surface plasmons (SPs) are the collective oscillatory motion of electrons on a conductor (usually metal) surface. There are two types to describe the coupling between the electromagnetic (EM) wave and the surface plasmons: the propagating mode, which

is called surface plasmon polaritons (SPPs), and the localized mode, which is called localized surface plasmons (LSPs). See **Fig. 2.1a and b**. [33, 34]

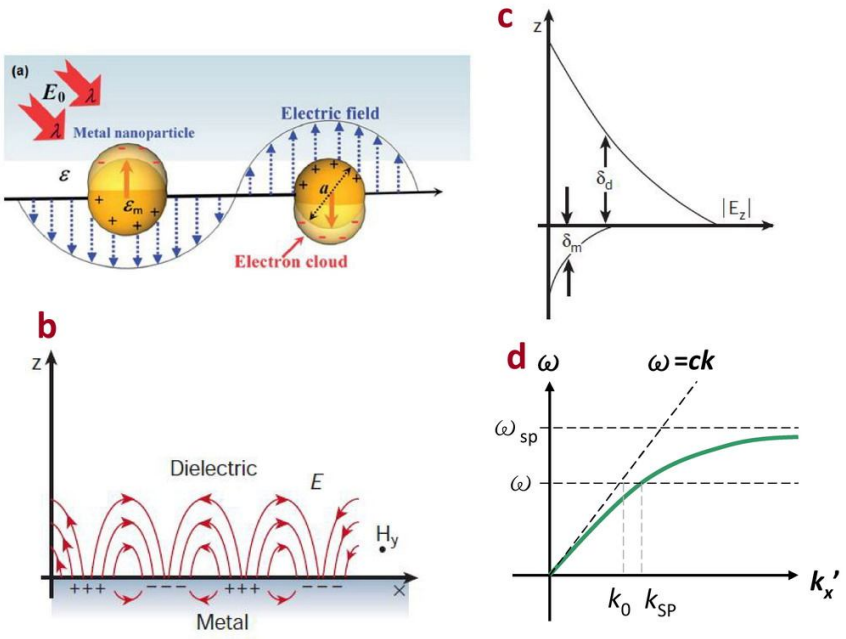

Figure 2.1 Schematic diagram illustrating **(a)** LSP (from [33]) and **(b)** SPP modes (from [34]). **(c)** From [34]. The field in the perpendicular direction is evanescent, reflecting the bound, non-radiative nature of SPPs, which prevents power from propagating away from the surface. **(d)** The dispersion curve of an SPP mode.

LSPs are associated with the collective oscillation of electrons confined locally by a metal nanostructure. The most representative example of LSPs is metal nano-particles (NPs). The particle plasmons are excited when the frequency of the incident light matches the resonant frequency of the NPs. One unique feature of LSPs is the localized enhancement of the EM field as a result of the strong resonance coupling between light and localized plasmon, leading to high efficiency of light concentration. Because the excited

plasmon are localized and cannot propagate along the nano-structures, this process is called localized surface plasmon resonances (LSPRs). [33]

SPPs are waves propagating along the surface of a conductor, usually a metal. To be more precise, they are EM waves confined to the conductor surface because of their interaction with free electrons in the conductor. In this interaction, the free electrons respond collectively by oscillating in resonance with the EM wave. [34]

Before introducing mathematical formulation in plasmonic theory (I will focus on SPPs in the next section), we might quickly go through a brief review of basic plasmon theory based on Drude model from a first-year physics graduate student's course on electromagnetic theory (adopted from Jackson's textbook. See Ref. [35]).

2.1.1 *A Simple Plasma Model of Metal*

First, we consider the equation of motion for an electron of charge -*e* bound by a harmonic force and acted on by an electric field $\tilde{\vec{E}}(\vec{x},t)$:

$$m(\ddot{\tilde{\vec{x}}} + \gamma\dot{\tilde{\vec{x}}} + {\omega_0}^2\tilde{\vec{x}}) = -e\tilde{\vec{E}}(\vec{x},t) \tag{2.1}$$

Here γ measures the damping force and ω_0 is the frequency of oscillation of the electron about the equilibrium. Suppose the field and the motion of the electron varies harmonically in time with frequency ω: $\tilde{\vec{E}}(\vec{x},t) = e^{-i\omega t}\vec{E}(\vec{x})$ and $\tilde{\vec{x}} = e^{-i\omega t}\vec{x}$, the dipole moment contributed by one electron is:

$$\vec{p} = -e\vec{x} = \frac{e^2}{m}\frac{1}{{\omega_0}^2 - \omega^2 - i\omega\gamma}\vec{E} \tag{2.2}$$

If there are *n* electrons per unit volume in the metal, Eq. (2.2) can be written as

$$\vec{P} = \frac{ne^2}{m}\frac{1}{{\omega_0}^2 - \omega^2 - i\omega\gamma}\vec{E} \tag{2.3}$$

Here $\vec{P}$ is the electric polarization (dipole moment per unit volume), $\vec{P} = \varepsilon_0 \chi_e \vec{E}$, ε_0 is the permittivity of free space, and χ_e is the electric susceptibility of the medium. Recalling the relationship between displacement, $\vec{D}$, and electric field, $\vec{E}$:

$$\vec{D} = \varepsilon_0 \vec{E} + \vec{P} = \varepsilon_0 \vec{E} + \varepsilon_0 \chi_e \vec{E} = \varepsilon_0 (1 + \chi_e) \vec{E} = \varepsilon \vec{E},$$

we have

$$\chi_e = \frac{\varepsilon}{\varepsilon_0} - 1.$$

Here ε is the electric permittivity. Now we have:

$$\vec{P} = \varepsilon_0 \left(\frac{\varepsilon}{\varepsilon_0} - 1 \right) \vec{E} \tag{2.4}$$

Comparing Eq. (2.3) with Eq. (2.4), we immediately have:

$$\frac{\varepsilon}{\varepsilon_0} = 1 + \frac{ne^2}{\varepsilon_0 m} \frac{1}{\omega_0^{\,2} - \omega^2 - i\omega\gamma} \tag{2.5}$$

For metals the electrons are free so we set $\omega_0 = 0$. We also replace m with m^*, the effective mass of conduction electrons. Now we define the plasma frequency of a metal as

$$\omega_p^{\,2} \equiv \frac{ne^2}{\varepsilon_0 m^*},$$

and Eq. (2.5) can be rewritten as

$$\frac{\varepsilon}{\varepsilon_0} = 1 - \frac{\omega_p^{\,2}}{\omega^2 + i\omega\gamma} \tag{2.6}$$

In Jackson's textbook, the author defined the dielectric function as $\frac{\varepsilon}{\varepsilon_0}$. Here we express the dielectric function of metal as

$$\varepsilon_m \equiv \frac{\varepsilon}{\varepsilon_0}$$

We may also need to consider the contribution of interband transitions (ε_{int}) to the dielectric function and rewrite Eq. (2.6) as

$$\varepsilon_m = \varepsilon_{\text{int}} - \frac{{\omega_p}^2}{\omega^2 + i\omega\gamma} \tag{2.7}$$

Eq. (2.7) is a full description of the dielectric function of a metal in this simplified model. Alternatively, if we ignore interband transitions and damping effects, we have:

$$\varepsilon_m = 1 - \frac{{\omega_p}^2}{\omega^2} \tag{2.8}$$

For light with frequency $\omega < \omega_p$ incident to the metal, it can only penetrate a very short distance into the metal (the "skin-dpeth") and is almost entirely reflected. But when the frequency is increased into the domain where $\varepsilon_m > 0$, the metal suddenly can transmit light and its reflectivity changes drastically. This typically occurs in the ultraviolet and is termed as "ultraviolet transparency of metal." Since both LSPs and SPPs are associated with the confinement of light with metal, it is required that ε_m is negative. *i.e.* the light utilized to excite LSPs or SPPs should not see the metal as "transparent", but as almost impenetrable in order for the plasmonic mode to be well confined to the surface of the metal. The first lesson for plasmonics is that, since metals tend to have large plasma frequencies, they are traditionally the choice for plasmonics.

2.1.2 *Surface Plasmon Polaritons (SPPs)*

Since a large part of research interest in plamonics is dedicated to the applications related to SPPs, we are going to illustrate the unique properties of SPPs in more detail in this subsection. In this subsection I heavily consulted the content from Ref. [36] and [37]. Here we only consider the simplest SPP waveguide, which is in a single metal-dielectric

interface (**Fig 2.1a**). Since SPPs are the mode of EM waves coupled to the collective oscillation of free electrons in a metal, the properties of SPPs are closely related to the permittivity of the dielectric material (lossless medium), $\varepsilon_d(\omega)$, and the dielectric function of the metal (lossy medium), $\varepsilon_m(\omega)$. Dielectric material's permittivity, $\varepsilon_d(\omega)$, is a positive real function of the frequency ω. The dielectric function of a metal $\varepsilon_m(\omega)$ can be expressed as a complex function of the frequency ω, $\varepsilon_m(\omega) = \varepsilon_m'(\omega) + \varepsilon_m''(\omega)$. The real part of the dielectric function $\varepsilon_m'(\omega)$ describes the strength of the polarization induced by an external electric field, and the imaginary part $\varepsilon_m''(\omega)$ describes the losses encountered in polarizing the material. Also note by separating the metal's dielectric function into the real and imaginary part, Eq. (2.8) needs to be written as

$$\varepsilon_m' = 1 - \frac{\omega_p^{\,2}}{\omega^2} \tag{2.9}$$

to be consistent with the notation.

In the case of a planar interface (**Fig. 2.1a**), to excite an SPP wave at the metal-dielectric interface, the incident optical wave must be transverse magnetic (TM)-polarized with respect to the incident plane. The SPP mode excited is also TM-polarized in character ($\vec{H}$ is in the y direction. The longitudinal component of the magnetic field $H_x = 0$). After considering appropriate interface boundary conditions we can derive basic relationships defining this system as follows:

$$k_x = k_x' + ik_x'' = k_0\sqrt{\frac{\varepsilon_m\varepsilon_d}{\varepsilon_m + \varepsilon_d}} \tag{2.10}$$

$$k_z^{(m)} = k_0\sqrt{\frac{\varepsilon_m^{\,2}}{\varepsilon_m + \varepsilon_d}} \tag{2.11a}$$

$$k_z^{(d)} = k_0 \sqrt{\frac{\varepsilon_d^{\,2}}{\varepsilon_m + \varepsilon_d}} \tag{2.11b}$$

Here $k_0 = \omega/c$ is the wavevector (wave number) in the free space. The derivation of these equations is fully explained in many textbooks. For example, see Ref. [38]. To obtain a propagating SPP solution, both k_x' and k_x" need to be real numbers. Here k_x' determines the SPP wavelength, while k_x" accounts for the damping of SPP. Moreover, to obtain a "bound" solution, both $k_z^{(m)}$ and $k_z^{(d)}$ need to be purely imaginary. For most metals (including Ag and Au) in the wavelength range of interest, say, from near infrared, through visible light, to the ultraviolet regime, ε_m' is negative as a prerequisite for SPP coupling between light and metal (see discussion in section 2.1.1). We also assume $\varepsilon_m" << |\varepsilon_m'|$. Then we have:

$$k_x = k_0 \sqrt{\frac{\varepsilon_m \varepsilon_d}{\varepsilon_m + \varepsilon_d}} = k_0 \sqrt{\frac{(\varepsilon_m' + i\varepsilon_m")\varepsilon_d}{\varepsilon_m' + i\varepsilon_m" + \varepsilon_d}} = k_0 \sqrt{\frac{\varepsilon_m' \varepsilon_d}{\varepsilon_m' + \varepsilon_d}} \sqrt{\frac{\varepsilon_m' + \varepsilon_d}{\varepsilon_m' \varepsilon_d} \frac{\varepsilon_m' \varepsilon_d + i\varepsilon_m" \varepsilon_d}{\varepsilon_m' + \varepsilon_d + i\varepsilon_m"}}$$

$$= k_0 \sqrt{\frac{\varepsilon_m' \varepsilon_d}{\varepsilon_m' + \varepsilon_d}} \left(1 + i\frac{\varepsilon_m"}{\varepsilon_m'}\right)^{1/2} \left(1 + i\frac{\varepsilon_m"}{\varepsilon_m' + \varepsilon_d}\right)^{-1/2} \approx k_0 \sqrt{\frac{\varepsilon_m' \varepsilon_d}{\varepsilon_m' + \varepsilon_d}} \left(1 + i\frac{1}{2}\frac{\varepsilon_m"}{\varepsilon_m'}\right)\left(1 - i\frac{1}{2}\frac{\varepsilon_m"}{\varepsilon_m' + \varepsilon_d}\right)$$

$$= k_0 \sqrt{\frac{\varepsilon_m' \varepsilon_d}{\varepsilon_m' + \varepsilon_d}} \left[1 + i\frac{1}{2}\frac{\varepsilon_m" \varepsilon_d}{\varepsilon_m'(\varepsilon_m' + \varepsilon_d)}\right]$$

Now we can separate the real part and the imaginary part of k_x:

$$k_x' \approx k_0 \sqrt{\frac{\varepsilon_m' \varepsilon_d}{\varepsilon_m' + \varepsilon_d}} \tag{2.12a}$$

$$k_x" \approx k_0 \left(\frac{\varepsilon_m' \varepsilon_d}{\varepsilon_m' + \varepsilon_d}\right)^{3/2} \frac{\varepsilon_m"}{2(\varepsilon_m')^2} \tag{2.12b}$$

Since $\varepsilon_m' < 0$, we see that the requirement for k_x' and k_x" to be real is

$$\varepsilon_m'(\omega) + \varepsilon_d(\omega) < 0 \tag{2.13}$$

Therefore, the second lesson for plasmonics is that, for SPP to occur, the absolute value of the real part of the metal's dielectric function should be larger than the dielectric material's dielectric function, *i.e.* $|\varepsilon_m'(\omega)| > \varepsilon_d(\omega)$. Most dielectric materials have the dielectric function close to 1. Noble metals are the choice for plasmonics because $|\varepsilon_m'(\omega)|$ of noble metals in the visible and near-infrared regions are usually larger than 1. See **Fig. 2.2a**. [32, 39, 40]

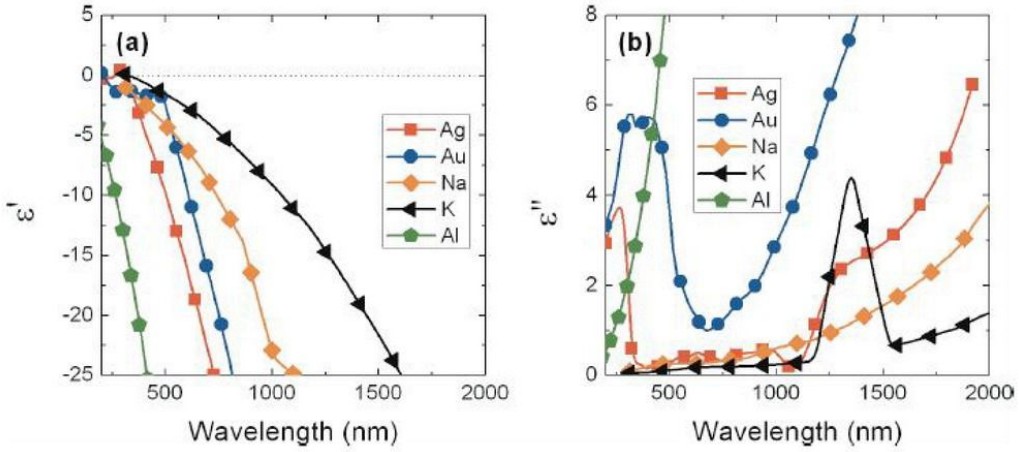

Figure 2.2 From [32]. Real **(a)** and imaginary **(b)** parts of the dielectric funtions of Ag, Au, Na, K and Al.

The non-radiative nature of SPPs can be described by $k_z^{(m)}$ and $k_z^{(d)}$, which represent the wave vectors of the evanescent field into the metal and into the dielectric material, respectively. Both of them are perpendicular to the metal-dielectric interface (z direction in our geometry in **Fig. 2.1a**). They illustrate the bound, non-radiative nature of SPPs. As we mentioned, for such bound solutions to exist, both $k_z^{(m)}$ and $k_z^{(d)}$ should be purely imaginary. Using the similar method of approximation to derive Eq. (2.12a) and (2.12b), we obtain the expression for $k_z^{(m)}$ and $k_z^{(d)}$ as follows:

$$k_z^{(m)} \approx ik_0 \sqrt{\frac{(\varepsilon_m')^2}{|\varepsilon_m' + \varepsilon_d|}} \tag{2.14a}$$

$$k_z^{(d)} \approx ik_0 \sqrt{\frac{\varepsilon_d^{\,2}}{|\varepsilon_m' + \varepsilon_d|}} \tag{2.14b}$$

The SPP electric field decays exponentially with the distance from the interface, either into the metal or the dielectric material. The decay length into the metal (the so-called "skin depth") δ_m and into the dielectric δ_d can be characterized by $k_z^{(m)}$ and $k_z^{(d)}$ respectively, as follows:

$$\delta_m = \frac{1}{\left|k_z^{(m)}\right|} \tag{2.15a}$$

$$\delta_d = \frac{1}{\left|k_z^{(d)}\right|} \tag{2.15b}$$

$$\frac{\delta_m}{\delta_d} = \frac{\left|k_z^{(d)}\right|}{\left|k_z^{(m)}\right|} = \frac{\varepsilon_d}{-\varepsilon_m'} \tag{2.15c}$$

The illustration of δ_m and δ_d is shown in **Fig. 2.1c**. [34] Now with all characteristic parameters for SPPs in readiness, we are going to discuss the dispersion curve of SPPs based on Eq. (2.12a). Here we temporarily ignore damping effect. **Fig. 2.1d** shows the dispersion curve of an SPP mode. We note that as k_x' becomes very large, the curve will asymptotically approach the surface plasmon frequency (ω_{SP}). Also note when k_x' becomes large, $|\varepsilon_m'| \approx \varepsilon_d$. We simply replace ε_m' with $-\varepsilon_d$ and ω with ω_{SP} in Eq. (2.9), and we have

$$\omega_{SP} = \frac{\omega_p}{\sqrt{1+\varepsilon_d}} \tag{2.16}$$

For $\varepsilon_d \approx 1, \omega_{SP} \approx \omega_p / \sqrt{2}$. In the regime of large k_x' (when the frequency is close to ω_{SP}), the electric field penetration into metal will be similar to that into dielectric, as expected by Eq. (2.15c). In this scenario the penetration in both materials reaches a minimum, representing a good confinement for the SPP mode.

In contrast, if k_x' is very small, we have $|\varepsilon_m'| >> \varepsilon_d$, and it will reach the regime where $k_x' \approx k_0$, in which $\delta_d >> \delta_m$. In this situation the SPP mode is poorly confined and largely propagates like an uncoupled EM wave, which will be seriously subjected to diffraction limit.

The third lesson of plasmonics is that for the good confinement of an SPP mode, we would like to operate the mode at high k_x' with frequency approaching ω_{SP}.

The divergence of the SPP dispersion curve from the free-traveling light as k_x' increases posts a dilemma: k_0 is smaller than k_x' for a fixed ω, and the discrepancy will become larger as ω approaches ω_{SP}. (See **Fig. 2.1d**) Therefore, direct coupling between a freely propagating EM mode and a SPP mode is forbidden by conservation of momentum. Some techniques were developed to overcome this problem of "momentum mismatch", including the use of prism to enhance the momentum of the incident light [41], and periodic patterning on the surface of the conductor [42, 43].

2.1.3 *Plasmonic Damping*

So far we have not yet incorporated damping (or loss) effect in our discussion in order to extract essential properties of SPPs with a simplified model. Since damping effect plays a critical role in the performance of SPPs, we will give a detailed discussion of damping effect and methods to reduce it in this subsection.

Because most loss in an SPP mode occurs in the metal , we will focus on metal exclusively in this subsection. First, damping effect in a metal is phenomenologically collected as γ in Eq. (2.7). Damping effect is manifested in the imaginary part of the metal's dielectric function, ε_m". When γ is large, ε_m" will also be large accordingly.

To discuss the effect of damping on SPPs we may consider the propagating electric field of an SPP mode $E(x)$ along the $+x$ direction:

$$E(x) = E_0 e^{i(k_x' + ik_x'')x - i\omega t}$$

The electric field intensity $I(x)$ can be expressed as

$$I(x) = |E(x)|^2 = I_0 e^{-2k_x'' x} \equiv I_0 \exp\left(-\frac{x}{L_{SP}}\right) \tag{2.17}$$

Here L_{SP} is the propagation length of the SPP (the distance the mode can travel before its intensity is attenuated to less than $1/e$ of its original intensity). Again, we assume $\varepsilon_m'' << |\varepsilon_m'|$. By conjuring up Eq. (2.12b) we can extract the expression for L_{SP}:

$$L_{SP} = \frac{1}{2k_x''} \approx \frac{1}{k_0}\left(\frac{\varepsilon_m' + \varepsilon_d}{\varepsilon_m' \varepsilon_d}\right)^{3/2} \frac{(\varepsilon_m')^2}{\varepsilon_m''} \tag{2.18}$$

Apparently in order to obtain a long propagation length we require that $|\varepsilon_m'|$ be large and ε_m" small. If ε_m" has already approached its intrinsic limit and cannot be reduced further, the strategy to increase L_{SP} is by choosing a metal with a large negative value of ε_m'. But if $|\varepsilon_m'|$ is large, it means that the SPP mode will be poorly confined as already discussed (in which k_x' is small and $\delta_d >> \delta_m$). This "trade-off" between plasmonic confinement and loss is typical for plasmonic systems. In other words, it is not possible to possess a good confinement and long propagation length at the same time though both are

desired properties for SPP operation. Considering this dilemma, the best strategy for the success of plasmonic devices is by use of low-loss materials.

Thus our forth lesson for plasmonics is that finding a metal with low ε_m" is crucial to the success of plasmonic devices.

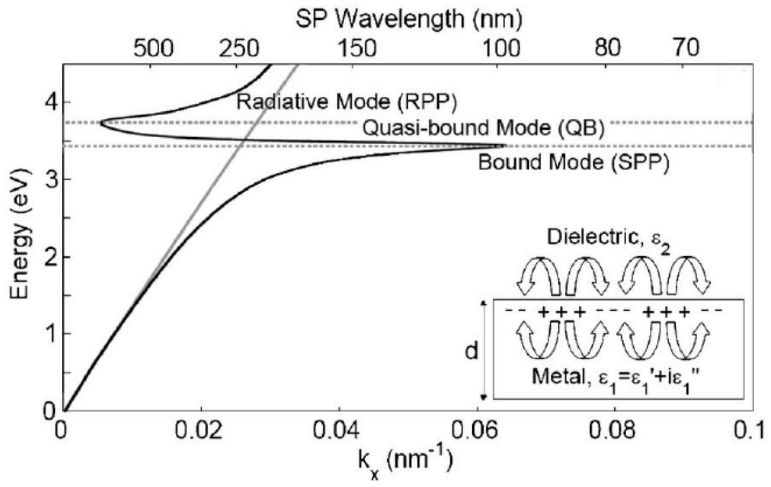

Figure 2.3 From [36, 44]. Surface plasmon dispersion relation for the Ag/SiO_2 geometry using the experimental Ag data (the damping effect is included).

If damping effect is considered, the SPP dispersion relation will be completely different from the simplified lossless curve (**Fig. 2.1d**) discussed in the previous section. As shown in **Fig 2.3**, [36, 44] instead of infinitely approaching ω_{SP} as k_x' becomes larger and larger, the dispersion curve "bends back" at a specific point of k_x'. It means that an SPP mode cannot be infinitely confined - the best confinement occurs at the point of the largest possible k_x' before the curve bends back. The damping effect not only sets restrictions on the best confinement an SPP mode can achieve, it also causes tremendous loss when an SPP mode is operated at its best confinement condition. In other words, by operating at a frequency approaching ω_{SP}, an SPP mode can be possibly confined below dif-

fraction limit, but the propagation length L_{SP} will be extremely short due to tremendous plasmonic loss.

Since the trade-off between confinement and loss is a serious problem every researcher in plasmonics must face, it is imperative to find plasmonic materials with the lowest loss, in order to produce an SPP mode with desired confinement below the diffraction limit, and at the same time preserving a reasonably long propagation length, to realize the fabrication of plasmonic devices.

In SPP modes the electromagnetic (EM) wave is coupled to the surface plasma of the metal. The electric field of the EM wave drives the oscillation of free electrons in the metal, resulting in Ohmic loss in the metal. Ohmic loss is mostly due to electron-electron scattering, electron-phonon scattering, and electron scattering by lattice defects and grain boundaries. [32] All these factors can be summed up in the damping parameter γ (which showed up in Eq. (2.1), at the very beginning of our discussion of plasma theory). Intrinsically low-loss materials with a small value of γ, such as Ag and Au (in the visible wavelength range) are no doubt the ideal candidates for plasmonics.

Damping due to grain boundaries and lattice defects can cause significant loss! With better fabrication techniques of materials, such as the fabrication of high-quality, single-crystalline epitaxial Ag films, the number of defects and grain boundaries in the crystal structure can be minimized, leading to significant reduction of plasmonic loss. [45]

The other channel of enormous loss in the metal is interband transitions. They occur when electrons in the metal jump to higher, empty energy states by absorption of incident photons. [32] Operations at frequencies higher than the onset frequency of a conductor's interband transition can cause significant plasmonic loss. For example, the inter-

band transition of Au occurs at 2.3 eV (about 540 nm, green light), so Au can support low-loss SPP propagation only in the infrared regime.

Not only Ohmic loss and interband transitions in the metal cause significant plasmonic loss, rough surface is also an important source of loss. The wavelength of typical SPP modes is short (in a scale of tens to hundreds of nanometers). Therefore an SPP mode propagating along the interface between metal and dielectric can be largely scattered due to rough surface features on the metal film such as islands and pits with a dimension of tens to hundreds of nanometers. Producing an atomically smooth film, on which rough surface features can be largely eliminated, is the key to the realization of a low-loss plasmonic platform.

Finally, radiation leakage can cause serious plasmonic loss. This occurs when SPPs propagate along the surface of a metal film whose thickness is similar to or less than the skin depth of the metal. For such a thin film, the electric field of the SPP will extend through the film and into the substrate. The plasmonic loss due to radiation leakage can significantly reduce the propagation length of the SPP. [45] Therefore, the films for plasmonic study must be thicker than the skin depth of the corresponding spectral range of operation. For example, the thickness of an Ag film for visible wavelength applications needs to be thicker than 40 nm in order to fully support SPP propagation.

In summary, I am dedicated to the growth of thick, atomically smooth, single-crstalline epitaxial films to realize the production of ideal plasmonic platforms with significant low loss in comparison with conventional polycrystalline films produced by thermal evaporation widely used in Optics community.

2.1.4 *Metal-Insulator-Semiconductor (MIS) Structure*

To solve the dilemma of the trade-off between good confinement and significant loss to the SPP propagation, a careful selection of a low-loss metal is the primary consideration, but through proper designs of plasmonic structures one can still allow SPPs to propagate long distances within strong confinement. It is therefore natural to consider the incorporation of optical gain material for loss compensation. Most of such materials are semiconductors such as CdS [46, 47], InGaN [48, 49], GaN [50], ZnO [51, 52], and GaAs [53].

Based on this idea, R. F. Oulton *et al.* proposed a model of hybrid optical wave guides consisting of a semiconductor nanowire separated from a metal surface by a nano-scale dielectric gap, the so-called "metal-insulator-semiconductor (MIS)" nanostructure. [46] From the results of their simulation the authors showed that when the semiconductor nanowire (gain medium) was brought closer to the metal surface by reducing the dielectric gap to the nanometer scale, the SPP mode would be primarily confined to a small mode area in this narrow dielectric gap. Interestingly, despite this strong confinement, the hybrid mode's propagation length exceeds that of SPPs confined at the equivalent metal-semiconductor interface.

The nanometer-thin dielectric gap (also called "spacer") plays a critical role in the MIS structure: (1) It supports the SPP mode in a metal-dielectric structure. (2) The spacer provides the means to store electromagnetic energy, leading to subwavelength optical waveguides with low loss. Since the mode is mainly propagating in the low-permittivity dielectric region rather than spreading into metal it is possibly the reason why the hybrid mode's propagation length is longer than that of SPPs at the equivalent metal-semiconductor interface.

In 2009 R. F. Oulton *et al.* published a paper in Nature in which they experimentally demonstrated the plasmon lasers at deep subwavelength scale based on the results they published in 2008 of the MIS design. [47] In that paper they indicated that the technical challenge of constructing plasmonic nanolasers lies in ensuring the good contact between the nanowire and the planar plasmonic film. Therefore the success of MIS devices largely depends on the fabrication of an atomically flat metal film with a universally uniform capping of the dielectric spacer. Such challenges were largely overcome in Shih Lab and coworkers by producing atomically flat metal films capped by a universally uniform dielectric layer. [48, 49] The results of study of atomically flat films will be presented in Chapter 4 (Ag) and Chapter 6 (Al). Capping techniques will be discussed in Chapter 5.

2.1.5 *Quality Factor (Q Factor)*

The literature and handbooks for optics and plasmonics communities often present data of materials by quality factors (Q factors). Q factors of a surface plasmon mode typically range from 10 to 100, which roughly corresponds to the number of electron oscillation that occur coherently. Q factor represents the capability of the plasmonic mode to sustain its phase and accumulate energy from the external excitation (pumping) field. The expression of Q factors involve both the real part and imaginary part of the metal's dielectric function. Generally, Q factors can be defined as:

$$Q \equiv \text{Enhanced local field / Incident field}$$

For a sphere nano-particle, the quality factor for the LSPR is given by

$$Q_{LSPR}(\omega) = \frac{-\varepsilon_m'(\omega)}{\varepsilon_m''(\omega)} \tag{2.19}$$

The Q factor for SPPs can be defined as the ratio of the real part (k_x') to the imaginary part (k_x") of the propagation wavevector. By using Eq. (2.12a) and (2.12b) we have

$$Q_{SPP}(\omega) = \frac{k_x'(\omega)}{k_x''(\omega)} = \frac{\varepsilon_m'(\omega) + \varepsilon_d(\omega)}{\varepsilon_m'(\omega)\varepsilon_d(\omega)} \frac{2[\varepsilon_m'(\omega)]^2}{\varepsilon_m''(\omega)} \tag{2.20}$$

Considering that $|\varepsilon_m'|$ is usually much larger than ε_d so that

$$\frac{\varepsilon_m'(\omega) + \varepsilon_d(\omega)}{\varepsilon_m'(\omega)\varepsilon_d(\omega)} \approx 1,$$

Eq. (2.20) can be simplified as

$$Q_{SPP}(\omega) \approx \frac{[\varepsilon_m'(\omega)]^2}{\varepsilon_m''(\omega)} \tag{2.21}$$

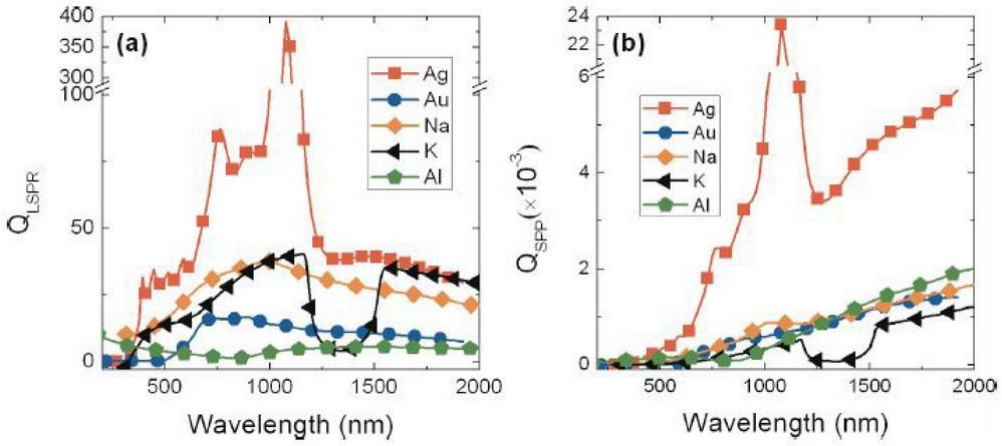

Figure 2.4 From [32]. Quality factors for **(a)** localized surface plasmon resonance (Q_{LSPR}) and **(b)** surface plasmon polariton (Q_{SPP}).

Both Q_{LSPR} and Q_{SPP} become large when a material has a large, negative ε_m' and small ε_m". A large quality factor is usually desired. From **Fig. 2.4** we see that both Q_{LSPR} and Q_{SPP} are large for Ag in the optical spectral range, illustrating why it is widely used in

the plasmonic community. [32] But we need to give a caveat here: if a large quality factor mainly comes from a large, negative value of ε_m' then it will cause poor confinement in the SPP mode, as already discussed, which is not desired for the design of nanometer-scale plasmonic devices. Therefore, the quality factor should be carefully interpreted. Generally, the larger it is, the better, because it usually indicates that the material is low-loss and the plasmonic mode supported by it sustains longer propagation length. But if a large value of quality factor is also contributed from a large value of ε_m' we need to consider whether it will cause poor confinement to the plasmonic mode.

2.1.6 *Summary*

In summary, for the SPP mode to be properly operated in the spectral range of interest, the following criteria should be carefully concerned:

(1) $\varepsilon_m' < 0$.

(2) $|\varepsilon_m'| > \varepsilon_d$.

(3) To operate the SPP mode at $\omega \rightarrow \omega_{SP}$, the best confinement can be achieved, but plasmonic loss will also be significant.

(4) For the plasmonic metal, choose a material with large ε_m' and small ε_m" (*i.e.* high Q factor) in order to increase L_{SP}. But ε_m' cannot overshoot or it will cause poor confinement to the SPP mode.

(5) Design proper plasmonic structures such as MIS nanostructures to compensate for the plasmonic loss due to strong confinement.

2.2 Materials for Plasmonic Applications

Since the main loss in SPP propagation occurs in metal, and since the properties of metal play a critical role in the SPP-based nano-photonics devices, I am going to focus

on metals in the discussion of plasmonic materials. The use of the term "materials" in this section will exclusively mean "metal materials". The dielectric part of the SPP structure will also be introduced in this section as we progress to the discussion of capping layers and their role as dielectric spacers.

Based on the discussion of basic knowledge on plasmonics, and the practical consideration of how easy a material is to prepare and work with, I listed the criteria below as to how to choose materials appropriate for plasmonic research:

(1) The materials should be low-loss (small ε_m"). Factors leading to small ε_m" include:

1-A. Intrinsically low-loss material. Intrinsic loss is mainly summed up in the damping factor γ, so we are going to find a material with the minimal value of γ.

1-B. Minimal effects by defects and grain boundaries. It means single-crystalline material will be much better than polycrystalline material.

1-C. Atomically smooth films to largely reduce SPP scattering due to rough surfaces.

1-D. No interband transition. We need to carefully check whether the interband transition will occur within the spectral range of interest. Choose a material whose interband transition will occur at a frequency higher than the frequencies in the range of operation.

1-E. No radiation leakage. If the plasmonic platform is a metal film, the thickness of the film should be thicker than the skin depth of the material to allow full support of the SPP mode.

(2) The real part of the dielectric function of the material, ε_m', shall be negative.

(3) Reactivity. The material should be stable in a convenient environment of operation, such as in the atmosphere and room temperature. A stable and inert material is preferred because it is easier to prepare and work with.

First, we are going to search for materials with high conductivity because their intrinsic loss will be low. Materials such as Ag, Au, Cu and Al will be ideal candidates considering their low values of γ. When we take a look of **Fig. 2.2**, we see that alkali metals such as Na and K also have low ε_m" in the visible to infrared range. Unfortunately alkali metals are extremely reactive to air and water so they are prohibitive in the perspective of practical consideration of fabrication and device operation.

Table 2.1 From [32]. Drude model parameters for metals. ω_{int} is the frequency of onset for interband transitions.

	ε_{int}	ω_p (eV)	γ (eV)	ω_{int} (eV)
Ag [39, 64, 65]	3.7	9.2	0.02	3.9
Au [39, 65]	6.9	8.9	0.07	2.3
Cu [39, 64, 65]	6.7	8.7	0.07	2.1
Al [66, 67]	0.7	12.7	0.13	1.41

The relevant data of ε_{int}, ω_p, γ, and ω_{int} (the frequency of onset for interband transitions) of Ag, Au, Cu and Al are listed in **Table 2.1** (from Ref. [32]) as a convenient reference to the following discussion of picking out superior plasmonic materials.

Next, we note that interband transition of Au and Cu occurs in a relatively low frequency, In Au, it is 2.3 eV and in Cu. it is about 2.1 eV. Interband transitions occur in both materials at about the green light range of the spectrum, making their applications mostly restricted to the infrared regime. Interband tansition occurs at 3.9 eV in Ag, which is at the ultraviolet (UV) range. With its low loss in the infrared to visible range, Ag is an ideal material for plasmonic devices operated in the range from infrared to visible light.

Al is a very interesting material. The interband transition of Al occurs at a low frequency of 1.41 eV (about 800 nm, near infrared), so it seems that Al is inappropriate to

work in the whole optical range. Intriguingly, the imaginary part of the dielectric function of Al drops steadily as the wavelength shortens (towards UV range). The crossover occurs at about 420 nm againt Au and about 310 nm against Ag. See **Fig. 2.2b**. When the wavelength plunges to the UV range, the real part of the dielectric function of Al is still negative while that of most other materials scrambles to zero and even positive values (it is because Al has an extraordinarily high plasma frequency). These features make Al appropriate for UV applications.

In brief, Ag is an ideal material from infrared to visible range and Al is a promising material for the UV plasmonics. It is why I am fully dedicated to the study of these two materials.

To further push the realization of nearly perfect plasmonic materials, I put great effort in preparing single-crystalline and atomically flat Ag and Al films which can greatly eliminate the detrimental effects from defects and grain boundaries. But Ag and Al are notorious due to their high reactivity and sensitivity to contaminants. It is known that Ag can easily degrade via oxidation and sulfidation, [54 - 57] and Al can immediately get oxidized even under very low exposure to oxygen. [58 - 61] These properties make the fabrication of plasmonic platforms based on these two materials particularly challenging.

Let's take Ag first. In their recipe of preparing better plasmonic films, Kevin M. MaPeak *et al.* wrote "Ag is the most unforgiving of the four metals (Al, Cu, Ag and Au) to deposit...Ag is susceptible to dewetting and grain-boundary pinning." [62] In their work, the authors found that if the pressure in the growth chamber was higher than 10^{-7} Torr the Ag films grown in such an environment would show pinholes and irregular grain boundaries and such poor films would inevitably lead to higher ε_m".

For Al, it is highly reactive to oxygen. Even in the best vacuum condition for a conventional thermal deposition facility (about 10^{-8} Torr), Al can still easily get oxidized. The remedy proposed by Kevin M. MaPeak *et al.* is by depositing Al at extremely high deposition rate (150 Å/s) to countervail the influence by residual gases. [62]

Fortunately the problems considering the reactivity of the source material can be best solved by an MBE system operated in the UHV environment (the base pressure of my system is 3×10^{-11} Torr). Because of this extremely clean environment the trouble of Ag film grain boundary pinning can be largely eliminated. By growing the film on a carefully flashed Si(111)-(7 × 7) surface can one further assure that the film will form a uniform single-crystalline structure (epitaxial growth).

For Al, a good UHV environment (good 10^{-11} Torr) can prevent it from oxidation (though a very tiny amount of oxide might not be fully excluded), assuring a high-purity deposition of the material onto the substrate.

However, even if the troubles originating from the source material's reactivity can be satisfactorily removed in a UHV environment, a plethora of other problems come up before we achieve a nearly perfect and workable metal platform for plasmonics.

The first issue concerns the flatness of the epitaxial film. As discussed in Chapter 1, over decades surface scientists struggled to develop techniques of growing atomically flat metal films. Eventually a novel method to achieve this is called the "two-step method", *i.e.* depositing the film at a low temperature with a subsequent annealing to room temperature. By this method flat Ag films can be grown on GaAs(110) [14, 63], Si(100) [24] and Si(111) [24 - 26], and flat Al films on Si(111) [28]. But for plasmonic film preparation, two-step method poses a serious limitation - so far it was mainly employed to study very thin films (a few MLs). For plasmonic films, they should be fairly thick (thicker than the skin depth of the metal, mostly > 30 nm) to avoid radiation leakage.

Therefore one of my main jobs focused on finding novel methods to prepare thick, while still atomically smooth, Ag and Al films for plasmonics applications. See Chapter 4 for Ag and Chapter 6 for Al.

Secondly, we need to deal with the problem of dewetting of the film. A well-prepared Ag film can be safely stored in UHV without degradation, but it can quickly deteriorate once removed from UHV (see Chapter 5 for dewetting study). In Shih Lab we developed several methods to cap and stabilize the film. An extensively utilized one is by capping the film with a thin (about 3 nm) Ge layer. The capping layer can naturally serve as a dielectric spacer in the MIS structure. In this context, a successful capping technique needs to satisfy a number of requirements: (1) It shall stabilize the underlying film it is supposed to protect. (2) It should be universally uniform, with excellent conformity to the morphology of the underlying film. (3) It shall be lossless to the plamonic mode.

Summing up all these considerations Ge will not be a good candidate to cap a plasmonic metal film because it is a narrow bandgap semiconductor, which may cause unexpected absorption in the optical spectral range. In order to produce a well-functioning MIS nanolaser by using a Ge-capped Ag film, Y.-J. Lu *et al.* further deposited 5 nm SiO_2 onto the Ge-capped film before placing InGaN-GaN core-shell nanowires on this metal-dielectric platform. [48] The thin SiO_2 layer, rather than Ge, serves as the dielectric spacer and it is unknown whether Ge causes unwanted attenuation to the plasmonic mode of the nanolaser. Such considerations motivate me to search for a better capping material, which can adequately cap the Ag film and also suitably work as a good dielectric spacer. Eventually I found that a thin capping layer of AlO_x can fulfill the purpose - I will introduce the technique in Chapter 5.

For Al, it can be naturally passivated once exposed to the atmosphere by spontaneously forming an oxide layer with a self-determined thickness. This native oxide layer

may readily serve as the capping layer and the dielectric spacer at the same time. But instead of subjecting the film to the uncontrollably naturally-occurring oxidation process in the ambient environment, which might introduce unwanted contaminants to the surface and cause dewetting, I oxidized the film *in-situ* with a well-controlled flow of high-purity oxygen gas. The detail will be discussed in Chapter 6.

Chapter 3: Experimental Methods

3.1 Home-built MBE System and Silicon Substrate Preparation

To facilitate the study of epitaxial growth of high-quality metal films for plasmonic applications, former lab member Dr. Charlotte E. Sanders was dedicated to the design and building of the MBE system I am currently using. With Dr. Jisun Kim and Dr. Chendong Zhang's assistance, they incorporated the MBE chamber into a grand UHV ensemble including a low-temperature scanning tunneling microscopy (LT-STM) system and a low energy electron diffraction (LEED) analysis chamber (**Fig. 3.1**). Thus the sample can be grown in an extremely clean deposition environment and then transfer *in-situ* without breaking vacuum to carry out LEED and STM study.

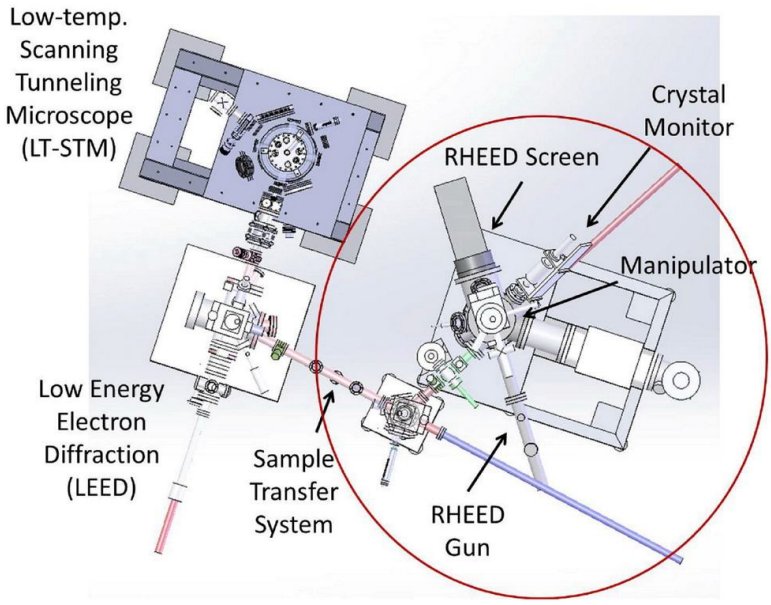

Figure 3.1 From [37]. Schematic of MBE chamber coupled with STM and LEED analysis chambers.

The MBE chamber, in which the base pressure can reach 3×10^{-11} Torr, is built around a four-port, water-cooled MBE growth flange based on the design by former lab member Professor Arthur Smith and by SVT Associates, Inc. Each of the flange's four ports can comfortably accommodate either an effusion cell or an electron-beam evaporator mounted on a 2.75" CF flange, and each is shielded by its own shutter. We use commercially Knudsen effusion cells ("K-cells") purchased from SVT Associates. Each effusion cell includes a crucible loaded with the source material and a C-type thermocouple for temperature monitoring. We use a pyrolytic boron nitride (PBN) crucible in each K-cell because PBN is a highly stable material, merited with its high-purity, chemically inert, thermally stable, low-outgassing, and non-wetting characteristics and long lifetime to be an ideal material as an MBE crucible.

The source temperature is carefully controlled by Eurotherm 2408 programmable proportional-integral-derivative (PID) controller that allows the temperature of the source material to be controlled to within 1 °C. The precise control of the source temperature is essential to the highly stable and reproducible deposition rate. Chilling water (about 4 °C) is continuously flowed through the interior of the growth flange and through the jacket around each growth port by a closed-cycle chilling system. Chilling water is crucial to maintain the vacuum in the growth chamber at or better than 10^{-10} Torr during deposition in which the source material is heated up to a high temperature. The chamber is equipped with an iced-water-cooled quartz crystal monitor (Maxtec, Inc. sensor crystal on Au, 6 MHz), which allows for deposition calibration prior to the growth of the film. A commercial reflection high energy electron diffraction (RHEED) system by Staib Instruments allows for *in-situ* characterization of the film and can also be used for growth calibration by continuously monitoring the sample during growth. RHEED data are collected and analyzed by kSA400 RHEED software by k-Space Associates, Inc. The sample growth stage

is home-built (see **Fig. 3.2** for the schematic of the design). It allows for direct heating and also for the sample to be cooled to about 90 K using a continuous flow of liquid N_2. The temperature of the growth stage is monitored by a pair of K-type thermocouples. The growth stage is attached to a commercial manipulator from Thermionics Inc., which features a precise control of *x*, *y* and *z* motion and a differentially pumped rotational platform so that the sample can be rotated during RHEED analysis (see section 4.4.3 for the need to rotate the sample during RHEED operation).

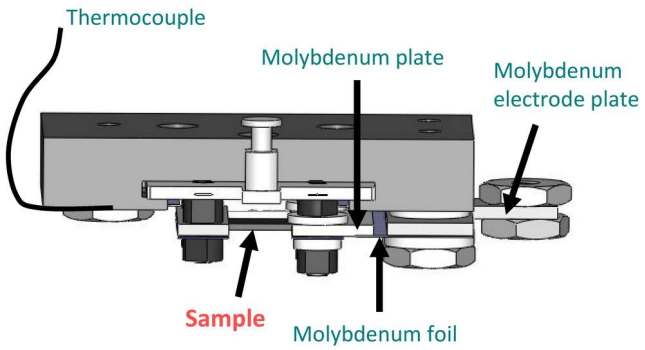

Figure 3.2 Growth stage installed in the MBE system. The stage provides good thermal conductivity, able to cool the sample down to 90 K using liquid N_2 cooling. It is also designed to allow direct heating of the sample by passing a direct electric current through the sample. Thus it allows the treatment of the highly-doped Si wafer to be carried out *in-situ* (see text).

In summary, out system delivers a couple of advantages which allow us to make great advancement in the study of epitaxial thin films:

(1) The base pressure of the chamber is 3×10^{-11} Torr. Even during growth the pressure can be kept no higher than 1.5×10^{-10} Torr. The worst pressure occurs when the room-temperature growth of Al with a high deposition rate (~ 5 Å/min) is carried out. In this situation the pressure can rise to about 5×10^{-10} Torr, still much better than

most growth systems. Such a clean growth environment eliminates a lot of detrimental effects of impurities and contaminants on the quality of the film (see discussion in Chapter 2).

(2) The K-cell provides a stable deposition with plenty of source materials. In other words, much more than a few depositions can be carried out in a perfectly reproducible setting of growth procedure before source materials run out. By this manner the growth can be run without being interrupted by the necessity to constantly refill source materials, and hence the growth efficiency can be tremendously promoted. This is particularly important for thick film (> 50 nm) growth. Moreover, the four-port growth flange allows the installation of 4 effusion cells, expanding the capability to study different materials in a chamber.

(3) The substrate preparation (which will be discussed below) and film growth can be monitored *in-situ* by RHEED, which allows a close assessment of the film quality before the sample is removed from UHV. Moreover, the film can be further analyzed by LEED and STM without breaking the vacuum during sample transfer. These powerful analysis tools allow us to design different growth methods (different substrates, coverage, growth temperatures, deposition rates...*et al.*) and study the resultant films more handily.

The Ag and Al films we studied in this dissertation are all grown on Si(111). Si(111) is the substrate of choice because of its intensive use in semiconductor industry and its compatibility with device manufacturing. Experimentally, Si(111) has a very appealing feature: The native oxide layer on its surface can be easily removed by simply flashing it to about 1200 °C in UHV. It is crucial to remove the oxide layer and expose the pristine Si surface prior to film deposition since a film grown on top of the oxide layer will be polycrystalline with a very rough surface morphology (the relevant data will be

presented in Chapter 6. A similar study on GaAs was reported by Shi-Wei Lin *et al*. See Chapter 1). A Si(111) substrate flashed in an appropriate condition is not only cleared of the oxide, but also shows a well-reconstructed 7 × 7 surface. Such a well-defined and "atomically clean" surface is essential for the subsequent growth of an epitaxial film. In our study, we followed a well-established procedure to prepare a high-quality Si(111)-(7 × 7) surface: First, we outgas the substrate by gradually passing a direct current through the substrate to about 2 A, which will heat up the sample to about 600 °C. After a few hours of outgassing, we flash the substrate to about 1200 °C by passing a high current (12 A - 16 A, depending on the size of the sample) through it within a short period of time (a few seconds) followed by a quick decrease of the current. The cycle of quickly increasing and decreasing the current is repeated a few times to thoroughly remove the surface oxide and expose a well-reconstructed 7 × 7 surface. The resultant Si(111)-(7 × 7) surface can be confirmed by RHEED and STM (STM image is from Ref. [68]), as shown in **Fig. 3.3**.

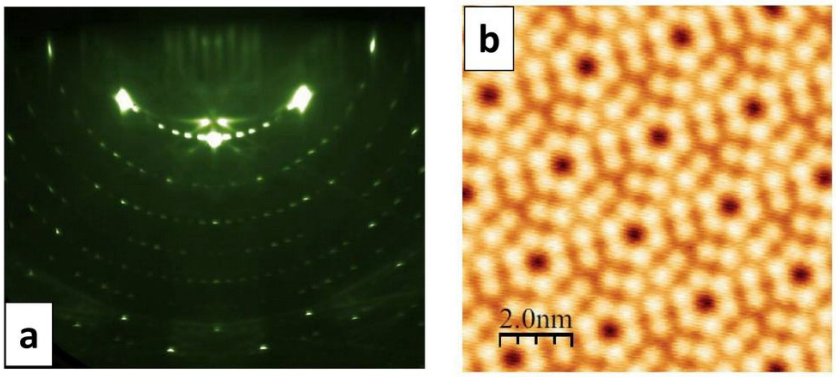

Figure 3.3 **(a)** RHEED and **(b)** STM image of a Si(111) wafer with a well reconstructed (7 × 7) surface. All films I studied in this dissertation are grown on such a well-reconstructed Si(111)-(7 × 7) substrate. STM image is from Ref. [68].

The use of fast direct-current heating during the whole process of flashing allows for localized heating of the sample with the minimal heat-up on the sample holder and surrounding growth stage; thus, the chamber pressure can remain in the 10^{-10} Torr regime throughout the process, guaranteeing the least contamination to the Si surface. Since a newly prepared Si(111)-(7 × 7) surface is dense with highly reactive dangling bonds, the growth of a metal film shall be carried out within hours after the substrate is carefully flashed.

3.2 Atomic Force Microscopy (AFM)

Like STM, atomic force microscopy (AFM) is a surface-sensitive technique capable of atomic resolution. AFM was developed by G. Binnig and C. F. Quate in 1986 to circumvent STM's requirements for sample conductivity (see next section for the introduction of STM). [69] AFM detects tip-sample force interactions (primarily van der Waals though a variety of magnetic and electrostatic forces can be probed), and unlike STM, does not normally provide information about electronic structures.

The surface is probed by the atomically sharp tip etched at the end of the flexible cantilever. There are many possible modes of operation. The most used among these operations can be broadly categorized as "contact" or "tapping". Contact mode is operated in which the tip "contacts" the surface of the sample, drags itself over the surface while recording deflection of the cantilever as a function of lateral position. The disadvantage of the contact mode for many applications is that the tip can damage the sample.

When operated in tapping mode, a piezoelectric element drives the cantilever near its resonant frequency (usually about 5 % offset from the resonant peak, as will be explained later in this section). The tip is brought near the surface of the sample where tip-sample interactions modify the resonant frequency as well as the resonant amplitude

of the tip without the tip actually touching the sample. The motion of the cantilever - in particular, its frequency and amplitude of vibration - is monitored, and the tip height is adjusted by feedback electronics which maintain a setpoint amplitude chosen by the user. By this manner the tip tracks the sample's topographical features, and control software records tip height z along a variety of parameters including oscillation amplitude, frequency, and phase shift as a function of lateral position (x,y).

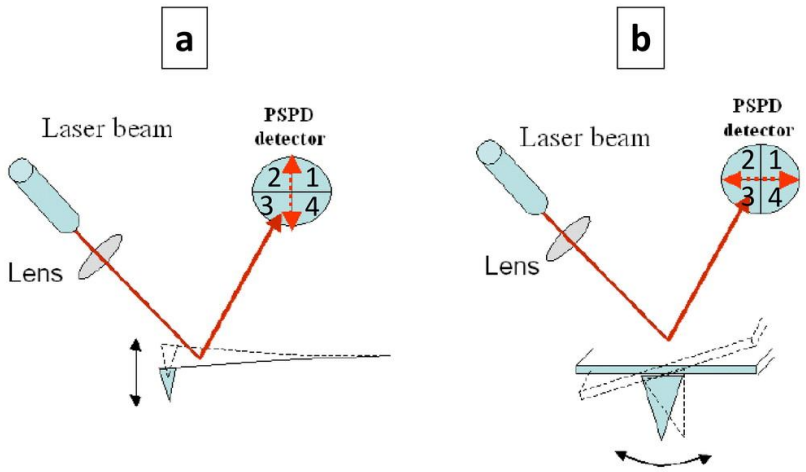

Figure 3.4 Adapted from [72]. Schematic of the setup to detect the motion of an AFM tip. The setup is composed of laser and a photodiode detector. **(a)** Detection of the flexural (or tapping) motion of the tip. **(b)** Detection of the torsional motion of the tip. The four quadrants of the photodiode are labeled as 1, 2, 3, and 4, respectively.

The most common means of detecting cantilever position is optical: a laser is focused on the back of the cantilever, which is polished to a mirror finish or coated with a highly reflective material for this purpose. The laser's angle of incidence is adjusted so that when the cantilever is in its neutral, unflexed position, the reflected laser spot falls on the center of a circular photodiode detector divided into four quadrants. At the cantilever moves, the laser spot moves up and down or left and right from its neutral position at the

center, thus changing the voltages detected at each of the four quadrants in a manner that allows the cantilever's motion to be determined by a computer processor. If the four quadrants of the photodiode is labeled as 1, 2, 3, and 4 (see **Fig. 3.4**), the vertical motion of the cantilever can be determined as $(V_1+V_2)-(V_3+V_4)$ and the horizontal motion as $(V_1+V_4)-(V_2+V_3)$.Vertical cantilever motion is with the primary interest since most applications by the tapping mode are based on the measurement of the vertical motion of the cantilever. The measurement of the horizontal motion is mostly used in the torsional movement of the cantilever, which is also developed to cover a variety of research fields. [70, 71]

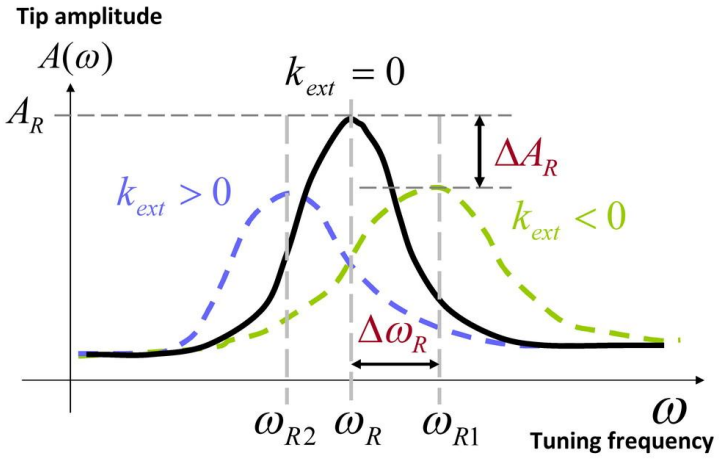

Figure 3.5 The relationship of tip's amplitude $A(\omega)$ versus tuning frequency ω with and without the external force. Note how the external force changes tip's resonant amplitude A_R and frequency ω_R.

In my study I exclusively use tapping mode to probe the surface morphology of the sample in the ambient environment since tapping mode provides a very stable scan in the atmosphere with the minimal risk of damaging the sample. As mentioned, in tapping mode, an AFM tip is driven to oscillate near its resonant frequency. For typical operation,

we first "tune" the tip in a chosen interval of frequencies, *i.e.* obtain the relationship between the tip's amplitude $A(\omega)$ and tuning frequency ω in the chosen window of frequencies and determine a frequency near the resonant peak at which the tip is driven to oscillate. Once the tip is brought near the surface of the sample, the external force resulting from the tip-sample interaction will modify the resonant amplitude and frequency of the tip, as shown in **Fig. 3.5**.

The influence of the external force on the oscillation of an AFM tip can be summarized in simple equations below (the derivation of these equations can be found in Ref. [72]):

$$\Delta\omega_R \approx -\frac{\omega_0 k_{ext}}{2k_e} \tag{3.1}$$

$$\Delta A_R \approx -A_R\left[1-\frac{1}{\sqrt{1+\frac{{k_{ext}}^2 Q^2}{2{k_e}^2}}}\right] \tag{3.2}$$

Here $\Delta\omega_R$ and ΔA_R are the shift of resonant frequency and resonant amplitude of the tip under the influence of the external force, respectively (see **Fig. 3.5**). A_R is the tip's resonant amplitude without the external force. k_e is the equivalent spring constant of the cantilever and ω_0 is the natural frequency of the cantilever,

$$\omega_0 = \sqrt{\frac{k_e}{m_e}}$$

(where m_e is the equivalent mass of the tip). Q is the quality factor of the oscillation, defined as

$$Q \equiv \frac{\omega_0}{2\beta}$$

(where β is the damping factor of the oscillation). k_{ext} is the gradient of the external force (F_{ext}) along the z direction:

$$k_{ext} \equiv \left.\frac{\partial F_{ext}}{\partial z}\right|_{z=z_0} \tag{3.3}$$

Here z_0 is the tip's balanced position where the spring force of the cantilever is equal to the external force, $F_{ext}(z_0) = k_e z_o$. From Eq. (3.1) and (3.2), we note that it is the gradient of the external force, k_{ext}, which modifies the resonant frequency and amplitude of the tip. The resonant frequency shifts to a higher value (ω_{R1} in **Fig. 3.5**) when the force gradient $k_{ext} < 0$ and to a lower value (ω_{R2} in **Fig. 3.5**) as the force gradient k_{ext} is positive. The amplitude will become smaller whether the force gradient k_{ext} is positive or negative.

For tapping mode to operate in the optimal condition, the frequency is not chosen at the resonant frequency ω_0, but at a frequency ω_m which gives the steepest slope in the tuning curve of the tip (the curve of $A(\omega)$ versus ω), where (see Ref. [73])

$$\omega_m \cong \omega_0\left(1 \pm \frac{1}{\sqrt{8Q}}\right) \tag{3.4}$$

Fig. 3.6 demonstrates the idea of making tapping mode work at ω_m. When the tip is far from the sample, its vibration amplitude at ω_m is A. When it is brought close to the surface, the amplitude is shifted to A' due to the tip-sample interaction. The amplitude shift at frequency ω_m, $\Delta A = A - A'$, is the largest compared with that at other frequencies. Since the sensitivity in terms of the amount of amplitude shifted by the external force is the largest at ω_m rather than other frequencies, the tip position can be better controlled to stably track the surface morphology of the sample. For the tapping-mode tip I used in my research (from Bruker, Model TESP, with specified resonant frequency between 306 and

350 kHz and spring constant 20 - 80 N/m), Q is about 600, so the frequency chosen for tapping mode is about 6 % offset of the resonant frequency ω_0.

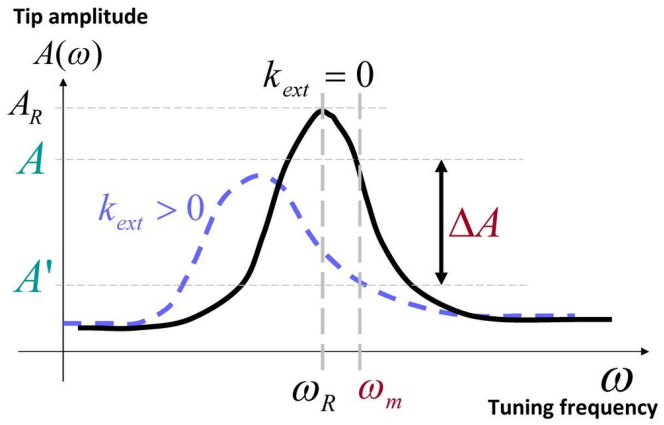

Figure 3.6 Illustration demonstrating the benefit of choosing the tapping-mode frequency at ω_m, at which the amplitude shows the steepest slope.

There are a lot of factors which can seriously interfere with the operation of AFM in the ambient environment. The most significant among them is the capillary force produced by a thin layer of water molecules covering the surface of the sample. The setpoint should be carefully adjusted during the operation to avoid the tip from "snapping to" the surface by this strong attractive force. Generally, the interactions between the tip and sample is very complicated, and one must increase or decrease the separation between tip and sample to take account of cantilever elasticity and the magnitude and range of the forces involved. [74]

AFM is a very important tool to help us interrogate the surface morphology of the sample. The information about the roughness of the sample can be extracted from the AFM image. To better understand the concept of roughness, we first assume that the height on each point of a surface "mesh" is expressed as $h = h(x_i, y_j)$, with $i = 1, 2, 3, ..., m$ and $j = 1, 2, 3, ..., n$. The average (or mean) of the height, μ (the "mean plane"), is simply

$$\mu = \frac{1}{mn}\sum_{i=1}^{m}\sum_{j=1}^{n} h(x_i, y_j) \tag{3.5}$$

If the surface is exactly on the mean plane, it will be perfectly flat. Any deviation on the surface from the mean plane is the original of the roughness of the surface. To quantify the roughness, we define the root-mean-square (RMS) roughness, R_q, by using the square of the deviation of the height from the mean plane at each point on the surface:

$$R_q \equiv \sqrt{\frac{1}{mn}\sum_{i=1}^{m}\sum_{j=1}^{n}\left[h(x_i, y_j) - \mu\right]^2} \tag{3.6}$$

However, we need to carefully interpret the value of R_q. Similar values of R_q do not necessarily mean similar roughness. The morphology of the surface should also be taken into account before giving a conclusion about the surface quality. For example, sine-wave-like and saw-tooth-like surfaces can have the same RMS roughness, but their roughness can be very different due to their different morphologies. For most samples we studied, the roughness mainly comes from islands, pits, grooves, clumps and mounds, all in nanometer scales, so RMS roughness is sufficient to reflect the quality of the surface in terms of the roughness contributed from these surface features.

3.3 Scanning Tunneling Microscopy (STM)

Scanning tunneling microscopy (STM), developed and first implemented by G. Binnig, H. Rohrer, Ch. Gerber, and E. Weibel at IBM Zurich in 1982, is a surface science technique to probe a sample's topography and electronic structures with atomic resolution. [75] It is typically used to investigate conductive, solid-state structures in a UHV environment. When an atomically sharp conductive tip is brought sufficiently close to the surface of the sample, typically within a few Å, the electron wavefunctions in the tip overlap electron wavefunctions in the sample surface. A finite tunneling conductance is

generated. By applying a bias voltage between the tip and the sample, a tunneling current I_t is generated. The magnitude of this current (typically in the order of 1 - 100 pA) is a function of tip-sample separation, as well as of the local electronic structure of the sample near the tip.

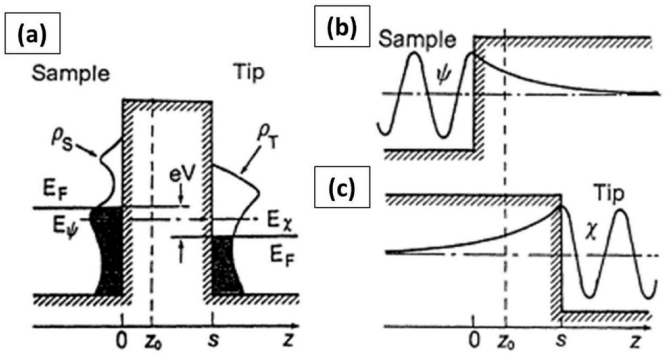

Figure 3.7 From [76]. Original caption: The Bardeen approach to tunneling theory. Instead of solving the Schrodinger equation for the coupled system, **(a)**, Bardeen (1960) makes clever use of perturbation theory. Starting with two free subsystems, **(b)** and **(c)**, the tunneling current is calculated through the overlap of the wavefunctions of free systems using the Fermi golden rule.

In order to achieve sub-atomic positioning, tips are mounted on a piezoelectric scanner. Typically, quarted tube scanners are utilized for STM. [76] For a tube-type scanner, voltages are applied between an inner electrode and one outer quarted electrode to achieve x, y, and z motions. In order to measure I_t, the output from the tunneling junction is sent to a current amplifier, typically with a gain of 1 V / 1 nA. The voltage value is then sent to the control module. Once I_t is measured, a negative feedback loop is established with I_t as the setpoint. During scanning, the feedback will keep I_t at the setpoint value. This is the most used mode among STM operations, called *constant current imaging*. During the scan, the scanner moves along the fast scan direction forward and backward,

then moves one unit forward in the slow scan direction. The procedure is repeated until a full image is attained. During scanning, the tip height is adjusted by feedback electronics which maintain the tunneling current at the setpoint. By this manner the tip tracks the sample's topographical features, and the image of the topography under constant current can be obtained.

The greatest power of STM lies not so much in topographic as in spectroscopic analysis - i.e. the scanning tunneling spectroscopy (STS). Interpretation of STM and STS data requires a theoretical understanding of tunneling current. The Bardeen approach is among the most frequently used [77], and it is set forth clearly by C. J. Chen. [76] Following Chen's exposition, **Fig. 3.7** illustrates Bardeen's approach, which side-steps the difficulty of solving Schrödinger equation for the complete tip-sample system by treating the tip and sample as two separate subsystems. As shown in **Fig. 3.7b and c**, ψ and χ represent the wavefunctions of stationary electronic states in the sample and tip, respectively, corresponding to eigenenergies E_ψ and E_χ. By utilizing the perturbation theory Bardeen argued that the probability of tunneling between any two particular states ψ and χ is determined by the overlap of their wavefuntions at a separation surface $z = z_0$ inside the tunneling barrier. In this treatment he defined a *tunneling matrix element* as

$$M \equiv \frac{\hbar^2}{2m} \int_{z=z_0} \left[\psi \frac{\partial \chi^*}{\partial z} - \chi^* \frac{\partial \psi}{\partial z} \right] dxdy \tag{3.7}$$

where m is the mass of the electron and the integration is run over the surface $z = z_0$.

Fermi's Golden Rule states that the probability, p, of an electron in the state ψ (the sample) at energy E_ψ tunneling to a state χ (the tip) with energy E_χ can be expressed as:

$$p = \frac{2\pi}{\hbar} |M|^2 \delta\left(E_\psi - E_\chi\right) \tag{3.8}$$

The Delta function in Eq. (3.8) ensures that only states with the same energy in both electrodes participate in the tunneling process. Thus, the tunneling current depends on how many states in the tip an electron in the sample can effectively tunnel into. Therefore, the tunneling current will depend on the *density of states (DOS) of the tip*, $\rho_T(E)$, with energy near that of a state in the sample. The number of available states in the sample is defined by the *density of states of the sample*, $\rho_S(E)$. If the density of states of the tip and sample does not vary appreciably near the Fermi level on the range of the applied bias V, the tunneling current can be expressed as

$$I = \frac{2\pi e^2 V}{\hbar} |M|^2 \rho_S(E_F)\rho_T(E_F) \tag{3.9}$$

The derivation of Eq. (3.9) can be found in C. J. Chen's book (Ref. [76]).

Using Eq. (3.9), the tunneling current at a bias voltage V can be evaluated by summing over all relevant states. At finite temperature the electrons in both the sample and tip follow the Fermi distribution:

$$F(E) = \frac{1}{1+\exp\left(\frac{E-E_F}{K_B T}\right)},$$

where k_B is the Boltzmann constant. With a bias voltage V, the total tunneling current is

$$I = \frac{4\pi e}{\hbar}\int_{-\infty}^{+\infty} d\varepsilon\left[F(E_F - eV + \varepsilon) - F\left(E_F + \varepsilon\right)\right] \times |M|^2 \rho_S(E_F - eV + \varepsilon)\rho_T(E_F + \varepsilon)$$

Since $k_B T$ is usually much smaller than the energy resolution required in the measurement, the Fermi distribution can be approximated by a step function, and the expression for the tunneling current can be simplified to

$$I = \frac{4\pi e}{\hbar}\int_{0}^{eV} d\varepsilon |M|^2 \rho_S(E_F - eV + \varepsilon)\rho_T(E_F + \varepsilon) \tag{3.10}$$

Here Bardeen further assumed that the magnitude of the tunneling matrix element does not change appreciably in the energy interval of interest. Then, the tunneling current is determined simply by the convolution of the *DOS* of the sample and the tip:

$$I \propto \frac{4\pi e}{\hbar}\int_0^{eV} d\varepsilon \rho_S(E_F - eV + \varepsilon)\rho_T(E_F + \varepsilon) \tag{3.11}$$

For a metallic STM tip, we can assume that the *DOS* of the tip is nearly constant. Therefore, there is a nice interpretation of the derivative of the tunneling current with respect to a changing voltage:

$$\frac{dI}{dV} \propto \rho_S(E_F - eV) \tag{3.12}$$

Eq. (3.12) tells us that change in the tunneling current I with respect to the bias V is directly proportional to the local density of states of the sample. By mapping the change in the tunneling current I in response to changes in applied bias V, it is possible to map the local density of states. This is the operating principle of scanning tunneling spectroscopy.

For both AFM and STM images the data analysis and imaging processing are carried out by Gwyddion, an SPM analysis software package developed by Department of Nanometrology Czech Metrology Institute. Data of scanning tunneling spectroscopy are processed with MATLAB developed by MathWorks.

3.4 Electron Diffraction Techniques

3.4.1 *Fundamental Concepts of Electron Diffraction*

In modern physics, scattering experiments are an important source to probe the surface structure in surface and thin film research. Such experiments tell us information about the symmetry and the geometric arrangement of atoms near the surface. An impor-

tant consideration for such techniques is that the incident particles shall not penetrate too deeply into the bulk of the solid. They shall only interact with the outermost atoms on the surface. Electron beams are an available source for such a purpose. With improved vacuum environment and better preparation of sample surface, the electron diffraction techniques, in which low energy electron diffraction (LEED) and reflection high energy electron diffraction (RHEED) are among the most commonly used, come into play as important probing tools in surface science.

To understand the essential concepts behind LEED and RHEED, a simple treatment of the surface scattering process within the framework of single-scattering events will be sufficient. This approach is called *kinematic theory*, which will lead to the most important concept to understand the physics behind LEED and RHEED - the *Ewald construction* in the reciprocal lattice space, as will be illustrated in this section. The theory is based on the assumption that the incident electron beam can be approximated as plane waves. This assumption is reasonable for many experimental setups if the electron gun is at least several centimeters away from the sample, considering that the interatomic dimension, where the diffraction occurs, is far smaller than the dimension of the experimental setup. A well explained treatment of the theory can be found in Ref. [12]. Here we only list important results from the kinematic theory:

(1) LEED and RHEED are mainly about the scattering (diffraction) of the incident electron beam by the surface atoms. All inelastic scattering can be neglected. Only elastic scattering, in which

$$E = E', \text{ or } \left|\vec{k}\right| = \left|\vec{k}'\right|, \tag{3.13}$$

needs to be considered. Here E and $\vec{k}$ are the energy and wave vector of the incident electrons, respectively. And E' and $\vec{k}'$ are the energy and wave vector of the diffracted

electrons, respectively. Since RHEED operates at very high energies (about 15 keV), elastic scattering dominates inelastic, so the negligence of inelastic scattering is justified. In LEED, inelastic scattering can be considerable, but the retarding grid (as will be discussed in more detail in the LEED section below) prevents inelastically scattered electrons from contributing to the diffraction pattern.

(2) The diffraction obeys the two-dimensional (2D) Laue conditions:

$$\vec{K}_{\parallel} = \vec{k}_{\parallel} - \vec{k}'_{\parallel} = \vec{G}_{\parallel} \tag{3.14}$$

Here $\vec{k}_{\parallel}$ and $\vec{k}'_{\parallel}$ are the component of the incident and diffracted wave vectors parallel to the sample surface, respectively. $\vec{G}_{\parallel}$ is the 2D reciprocal lattice vectors. Note that the third Laue condition (along the *z* direction, or the direction perpendicular to the sample surface) is missing in the 2D case since the scattering of the electrons only occurs on the topmost layer of the sample.

The conditions for the occurrence of an elastic Bragg spot in the electron diffraction pattern is given by Eq. (3.13) and (3.14). In other words, the scattering vector component parallel to the surface ($\vec{K}_{\parallel} = \vec{k}_{\parallel} - \vec{k}'_{\parallel}$) must be a 2D reciprocal lattice vector $\vec{G}_{\parallel}$. This condition is valid only for the limiting case where only the topmost atomic layer is involved in scattering. Since the third Laue condition is missing in the 2D case, in order to extend the Ewald contruction to the 2D problem we simply extend a "rod" normal to the surface from each 2D reciprocal lattice point (*h*,*k*), as shown in **Fig. 3.8**. To graphically determine a constructive interference we first orient the wave vector of the incident beam $\vec{k}$ to a reciprocal lattice point, with its other end pinned as the origin to draw a circle of radius $\left|\vec{k}\right|$ (since the elastic scattering requires $\left|\vec{k}\right| = \left|\vec{k}'\right|$), as shown in **Fig. 3.8**. The condition $\vec{K}_{\parallel} = \vec{G}_{\parallel}$ is fulfilled for every point at which the sphere crosses a "reciprocal lattice rod". Therefore, to make a long story short, the electron diffraction pattern in

LEED and RHEED is basically the visualization of the 2D reciprocal lattice of the surface (which is visualized as the spots shown in the diffraction pattern in LEED or RHEED ,which are called the Bragg spots).

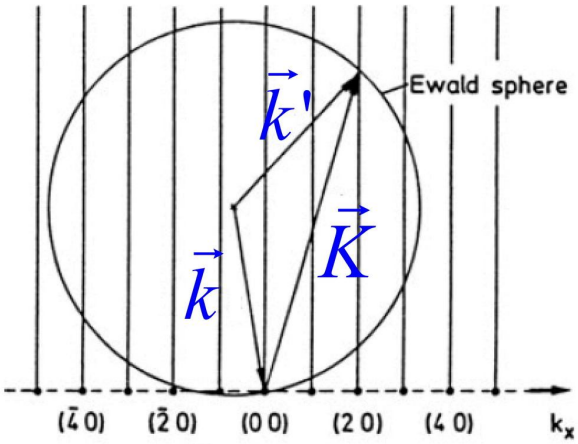

$$\vec{K}_{\parallel} = \vec{k}_{\parallel} - \vec{k}'_{\parallel} = \vec{G}_{\parallel} = \vec{G}_{20}$$

Figure 3.8 Adapted from [12]. Ewald construction for elastic scattering on a 2D lattice. The corresponding 2D reciprocal lattice points (h,k) are plotted on a cut along k_x. The figure shows the fulfillment of the Bragg diffraction for the reciprocal lattice point (h,k) = (2,0). A number of other Bragg points can be observed, depending on the size of the Ewald sphere.

However, these conditions are exact only in the limit of scattering from a true 2D network of atoms. In real experiments, however, electrons can penetrate several layers into the solid. The deeper the penetration is, the more significantly the scattering events in the z direction contribute to the electron diffraction pattern. This will lead to a modification of the "rod" structure in the 2D Ewald construction. Now, as shown in **Fig. 3.9**, due to more significance from z-direction scattering, each rod will be given periodically more intense spots. When the Ewald sphere crosses such an "intense" spot on the rod, the cor-

responding Bragg spot will be enhanced whereas the Bragg spot resulting from the crossing of the sphere with the insignificant portion of the rod will be weakened. If we change the primary energy of the incoming electrons, the radius of the Ewald sphere will change accordingly. The Ewald sphere will thus passes successively through stronger and weaker portions of the rod and the intensity of the Bragg spot will vary periodically.

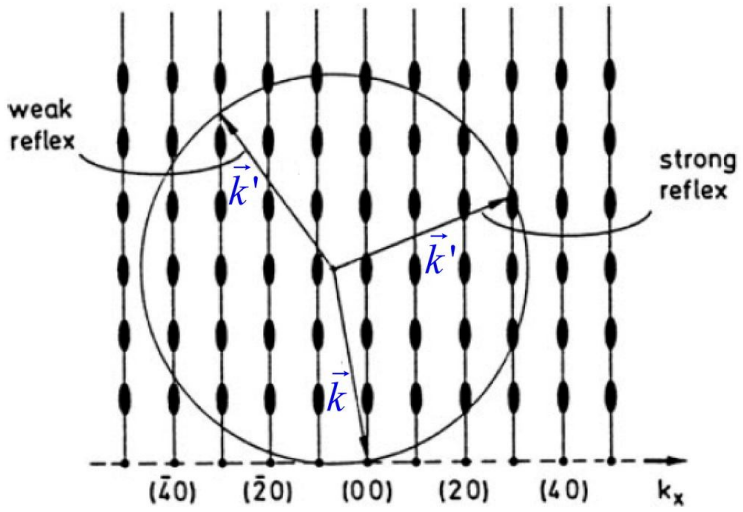

Figure 3.9 Adapted from [12]. Ewald construction for elastic scattering on a quasi-2D surface lattice. Now not only scattering from the topmost lattice plane, but also from a few underlying layers, is taken into account. The "thicker" spots on each rod arise from the third Laue condition (because of more penetration into the film, and consequently more scattering along the direction perpendicular to the surface). Correspondingly, the diffraction towards (3,0) will show a higher intensity than that towards $(\bar{3},0)$.

One very important consideration for both LEED and RHEED is that the primary electron beam may deviate from an ideal plane wave. It is actually a mixture of waves of slightly different energy and direction. These deviations from the ideal direction and energy thus result in an finite energy width (about 500 meV) and the angular spread of the

beam. Due to these imperfections, the electrons impinging on the crystal surface will exhibit slightly random variations in phase. If two spots on the surface have too large a separation, the incoming waves cannot be considered as coherent. In this situation the phases are not correlated and the outgoing waves cannot interfere to produce a diffraction pattern. In this context we define the coherent length of the electron beam such that atoms on the surface are considered to be illuminated by a simple plane wave if they are within the coherent length. Waves scattered from atoms separated more than the coherent length will add in intensity rather than amplitude; thus no surface feature on a scale larger than the coherent length can contribute to a diffraction pattern.

3.4.2 *Low Energy Electron Diffraction (LEED)*

The standard experimental setup for LEED consists of an electron gun to produce the electron beam with primary energy ranging from 20 to 500 eV and a display screen to show the Bragg diffraction spots. At the sample surface the incident beam can have a diameter on the order of mm but the coherent length is typically much less, potentially as small as several hundred Å. [12, 78] After interacting with the sample surface, the electrons scatter back to a phophorescent screen to produce the diffraction pattern.

A typical LEED system is exhibited in **Fig. 3.10.** [12] The unit of the electron gun consists of a direct or indirect heated filament with a Wehnelt cylinder followed by an electrostatic apertures A, B, C, and D. The accelerating energy is determined by the potential between the cathode (filament) and apertures A and D. Apertures B and C have potentials intermediate between A and D and are used to focus the electron beam. Initial collimation is achieved by the Wehnelt cylinder which has a negative bias with respect to the filament cathode. The last aperture D, also called the drift tube, is usually at the same (ground) potential as aperture A and the sample; the same is true for the first and last

grids in front of the fluorescent screen. By this way a field-free space is established between the sample and the display system through which electrons travel to the surface and back after scattering. The fluorescent screen itself is positively biased (about 5 kV) in order to accelerate and collect the scattered electrons. Only high-energy electrons from elastic scattering can be made visible on the screen. Besides elastic scattering, inelastic scattering also occurs at the sample surface. These electrons are scattered with wide angles and produce a relatively homogeneous background illumination of the phosphorescent screen. This background illumination is suppressed by giving the middle grid a negative bias (the "retarding" grid). The inelastically scattered electrons can thus be prevented from reaching the screen.

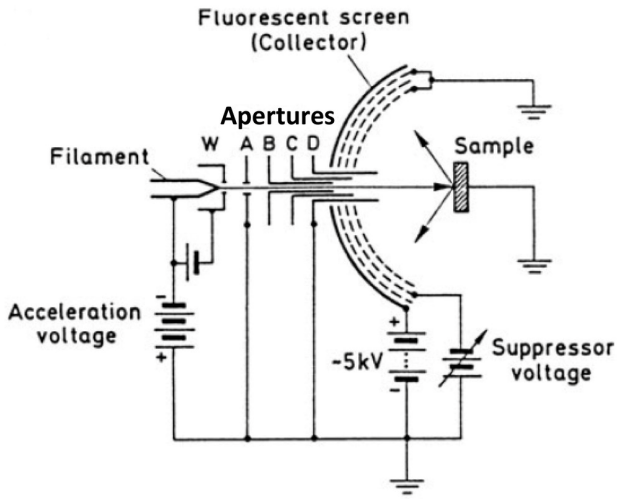

Figure 3.10 From [12]. Schematic of LEED. The integrated electron gun consists of a heated filament, a Wehnelt cylinder (W) and the electron optics containing apertures A, B, C, and D.

An example of LEED pattern is shown in **Fig. 3.11**, in which LEED is carried out on a 40 nm Ag film grown on Si(111) by the two-step method (the growth method will be

discussed in detail in Chapter 4). [45] The Ag film grown on a well-reconstructed Si(111)-(7 × 7) substrate exhibit a (111)-(1 × 1) hexagonal close packed crystalline structure. Its reciprocal lattice consists of hexagonal patterns, which can be well observed by LEED. We also note that the Bragg spots on the LEED pattern is very sharp, indicating a universally well-ordered crystalline structure of the surface. Interestingly, as will be shown in Chapter 6, the same pattern is also observed on the sample of Al(111)-(1 × 1) film grown on Si(111) at room temperature with a high deposition rate, suggesting that the epitaxial growth of films with good crystallinity can also be achieved at room temperature.

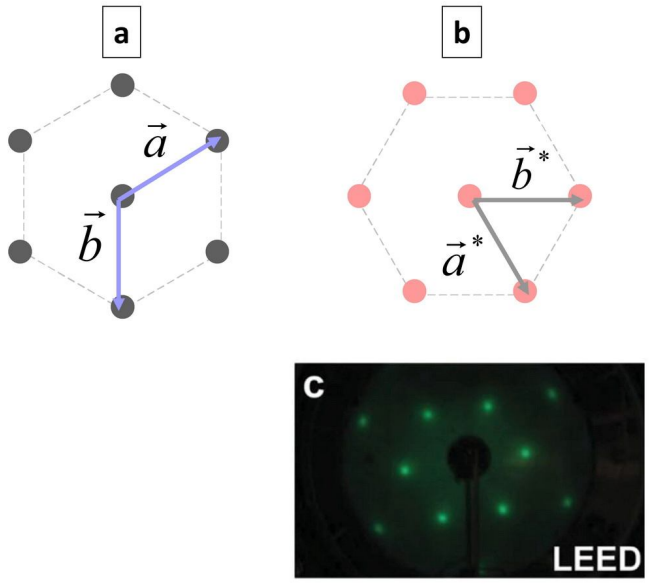

Figure 3.11 **(a)** (1 × 1) hexagonal-close-packed lattice structure of the Ag(111) plane in the real space, where $\vec{a}$ and $\vec{b}$ are primitive lattice vectors. **(b)** Reciprocal lattice points of the corresponding real-space lattice structure of **(a)**. Here $\vec{a}^*$ and $\vec{b}^*$ are reciprocal lattice primitive vectors. **(c)** From [45]. LEED taken on an epitaxial Ag film (45 nm thick) grown on Si(111) showing the hexagonal reciprocal lattice structure. See Chapter 4 for detailed discussion of the growth method.

3.4.3 *Reflection High Energy Electron Diffraction (RHEED)*

A RHHED setup is shown in **Fig. 3.12**. As in the case of LEED, an electron gun consisting of a cathode and a series of grids and focusing elements creates an electron beam with smaller angular divergence. Beam divergence on the order of 0.1 mrad. is adequate for most applications. [79] There are two key differences between RHEED and LEED:

(1) The beam energy - RHEED operates in the range of 12 - 15 keV, as opposed to a few hundreds of eV at most in LEED. The much higher voltages used in RHEED require special power supplies and vacuum feedthroughs. No acceleration of the electrons is necessary since the high primary energies are sufficient to produce fluorescence. The screen is usually planar and sometimes coated with a conducting film on the UHV side to prevent charge accumulation. No energy filtering of inelastic and secondary electrons is necessary since the diffracted beams are much more intense the back-ground.

(2) LEED features a relatively compact geometry: The angle of beam incidence on the sample in LEED is usually close to normal. RHEED, by contrast, has an open ge-ometry, as shown in **Fig. 3.12**. The beam encounters the sample at an oblique angle and the gun and screen are much farther from the sample than in LEED. The spatial separation between the electron gun and sample, and of sample and screen, can be as long as 50 cm. Therefore, RHEED can be easily incorporated in an MBE system, and one can monitor the sample *in-situ* by RHEED during MBE growth.

Since in RHEED, the electron beam interacts with the surface at a low glancing angle, RHEED patterns are highly sensitive to the azimuthal angles. For full symmetry of the surface to be seen, RHEED setup usually includes a sample holder that can be rotated

azimuthally. Like LEED, RHEED is operated under UHV to minimize accumulation of adsorbates on the sample surface. Good vacuum conditions are also important in RHEED because of the long beam path, along which defocusing can be problematic.

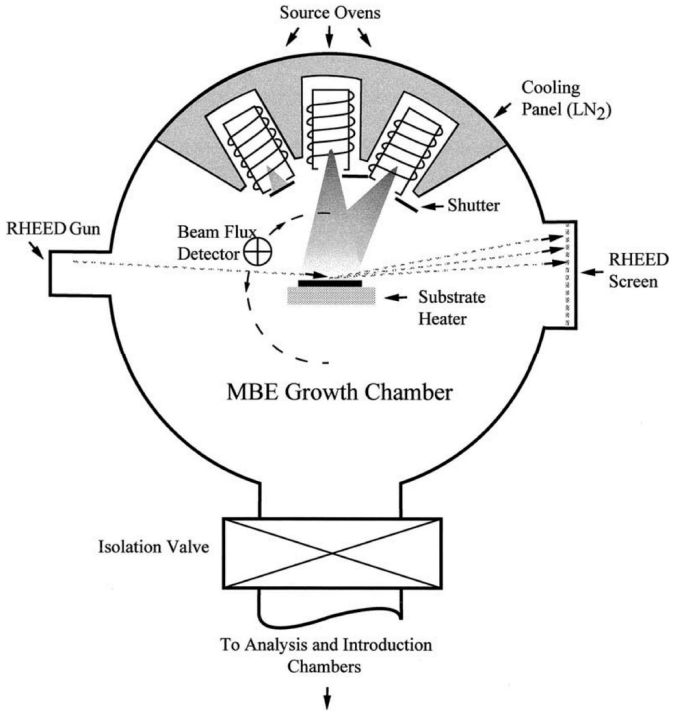

Figure 3.12 From [1]. Schematic of an MBE chamber equipped with a RHEED system.

Because of the low grazing angle, very flat surface is needed for RHEED. Strong deformation or "twisting" on the surface will shadow part of the diffraction pattern. Since RHEED is very sensitive to the surface quality and morphology, it is usually used as a primary tool to interrogate surface corrugation and growth mode during thin film deposition. However, it also means that RHEED patterns contain more information than simply the reciprocal lattice structure of the surface, and shall be interpreted carefully. I am going to explain RHEED patterns commonly observed in my study before concluding this chapter.

Fig. 3.13a shows the RHEED pattern on a 20 ML Ag film immediately after growth at 90 K. The film is grown on a Si(111) substrate. **Fig. 3.13b** is the RHEED pattern on the same film after it is annealed to room temperature.

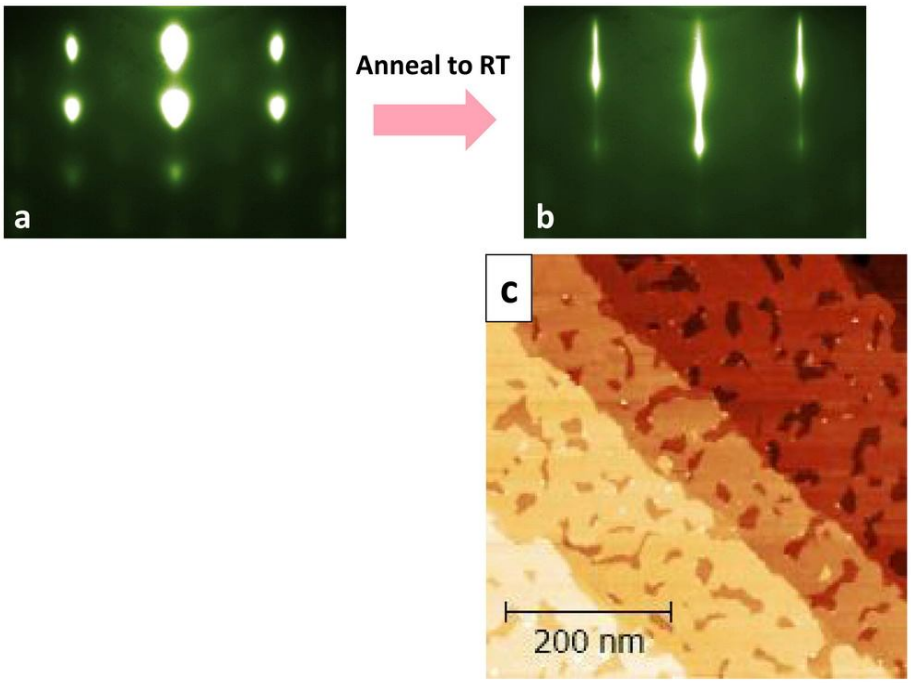

Figure 3.13 **(a)** RHEED taken, immediately after the growth is finished, on a 20 ML Ag film grown at 90 K on Si(111). **(b)** RHEED taken on the same film, after annealing to room temperature. **(c)** STM image of the film after it is annealed to room temperature. The image shows an atomically smooth morphology with pits on the terrace, which are single-layer lower than the terrace. These surface features give rise to the "*domains*" introduced in the main text to explain the RHEED pattern observed in **(b)**.

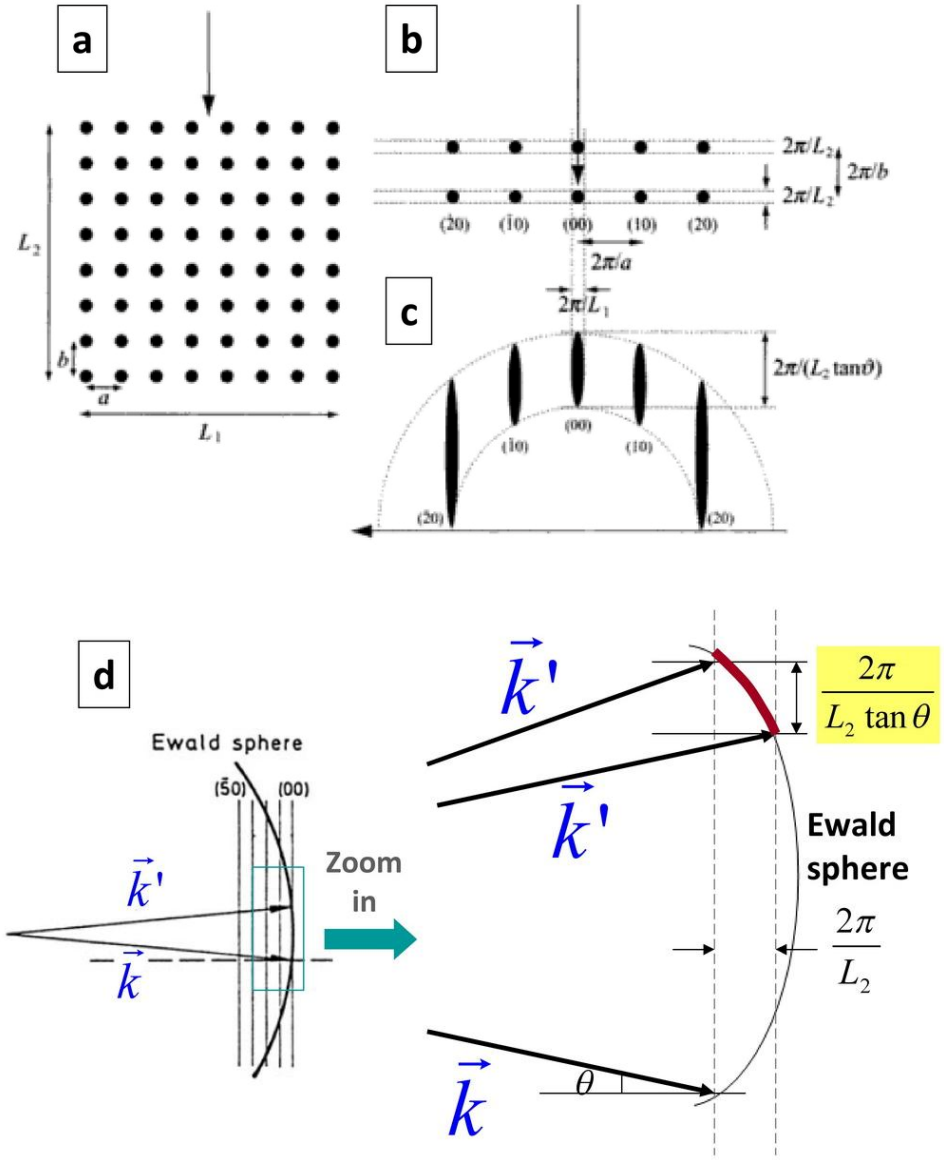

Figure 3.14 Schematic to explain the origin of streaks commonly observed in the RHEED pattern of thin films. **(a)** From [79]. Real-space lattice structure in a *domain*. **(b)** From [79]. Reciprocal lattice "spots" arising from the lattice structure and the finite *domain*. **(c)** From [79]. Schematic showing the elongated streaks because of these reciprocal lattice "spots". **(d)** Adapted from [12, 79]. A more detailed depiction to explain how reciprocal lattice spots are elongated into streaks in the RHEED pattern due to a very oblique glancing angle of the incident beam, θ.

The streak pattern in **Fig. 3.13b** is commonly observed in RHEED. **Fig. 3.14** is the schematic to explain the origin of the streak pattern. [12, 79] Consider a surface structure with a finite *domain* whose size is designated as L_1 and L_2. Due to the finite domain size, every reciprocal lattice point will be broadened into a spot with a dimension of $2\pi/L_1 \times 2\pi/L_2$. These broadened spots will form "cylindrical rods" (reciprocal lattice rods) instead of straight lines in **Fig. 3.8**. Furthermore, because of the low glancing angle, the intersection with the Ewald sphere of each reciprocal lattice rod is elongated into a streak whose length is extended from $2\pi/L_2$ to $2\pi/(L_2\tan\theta)$ (where θ is the glancing angle) while its width remains as $2\pi/L_1$. **Fig. 3.14d** shows in detail how the intersection of the Ewald sphere and the reciprocal lattice rod gives rise to the elongated streak pattern observed in **Fig. 3.13b**.

The streaks in **Fig. 3.13b** are narrow and sharp, indicating that the *domains* are large and each *domain* contains well-ordered crystalline structure. The *domains* described here in our sample mainly come from pits and the spacing between pits on the terrace, as evidenced in the STM image of the 20 ML Ag film after it is annealed to room temperature (**Fig. 3.13c**). The mean pit diameter as well as the space between pits determines an average *domain* size (in the order of about 20 - 50 nm in our sample) and hence the dimension of the RHEED streak.

Instead of the streak pattern, RHEED on the as-grown Ag film (taken at 90 K) (**Fig. 3.13a**) shows broadened, round blobs. This pattern indicates that the film, instead of a flat 2D structure with single-layer islands and pits, shows nanoclusters with size of tens of Å on the surface. We did not carry out STM on the as-grown film on Si(111). We believe that the structure shall look similar to the one which was imaged on an Ag film grown on GaAs(110) (see **Fig. 1.3a** in Chapter 1). Here, the incident beam can be scattered from planes further into the crystal in the z direction than it could on a flat surface,

as illustrated in **Fig. 3.15**. Scattering from several planes will strongly modulate the intensity along the reciprocal lattice rod, as shown in **Fig. 3.9**, giving rise to reciprocal lattice spots along the rod, which are intersected by the Ewald sphere and eventually lead to the formation of round spots observed in the RHEED pattern. The reciprocal lattice in this case consists of arrays of points along each reciprocal lattice rod. These points are broadened owing to the finite depth of penetration by the electron beam into the film. Consider a square (nanocluster) *domain* with a dimension $L \times L$ effectively penetrated by the electron beam with a finite depth L_z. It will give rise to reciprocal lattice rods of dimension $2\pi/L \times 2\pi/L$ plus spots with a dimension $2\pi/L_z$ lining along each rod. Since both L and L_z are small, it explains the broadened and round spots we observed in the RHEED pattern on the as-grown Ag film.

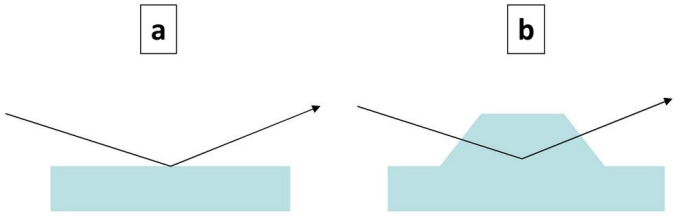

Figure 3.15 Two different scattering schemes on a highly enlarged surface area: **(a)** Surface scattering on a flat surface, and **(b)** bulk scattering by a three-dimensional crystalline island on top of the surface, assuming that the size of the island is below the coherent length of the electron beam.

The RHEED pattern of Si(111)-(7 × 7) shows a pattern with very sharp and clear spots, instead of elongated streaks, indicating that the surface is universally atomically well-ordered without being separated by *domains*. (**Fig. 3.3**) Moreover, the pattern shows straight lines radiating from the central diffraction spot, which are called Kikuchi lines. Sharp Kikuchi lines are obtained from crystals with perfect surfaces and perfect bulk lat-

tices. Kikuchi-line formation is due to inelastic scattering, which is most easily understood in the transmission electron diffraction scheme. [79] **Fig. 3.16** shows a schematic of the process. Electrons are scattered inelastically in all directions; their intensity generally decreases as the scattering angle increases. In some direction, for example, P_1, they will satisfy the Bragg condition for a set of lattice planes. These inelastically scattered electrons in the direction P_1 will act as pseudo-primary beam, which is then Bragg diffracted into a beam D_1. The intensity of P_1 decreases while the intensity of D_1 increases due to the diffraction. Overall, the inelastic intensity decreases with increasing scattering angle. Note for each set of planes there is a corresponding inelastic scattering direction, P_2, which also satisfies the Bragg diffraction condition to compensate for the intensity loss of P_1. However, the process P_2 is usually weaker than P_1 so the compensation is insufficient to replace the lost intensity. The result is that the scattering to the direction of D_1 is enhanced, which gives rise to the formation of Kikuchi lines. In short, for Kikuchi lines to form, an ordered crystal structure is a necessity for the Bragg condition to be satisfied in the inelastic scattering.

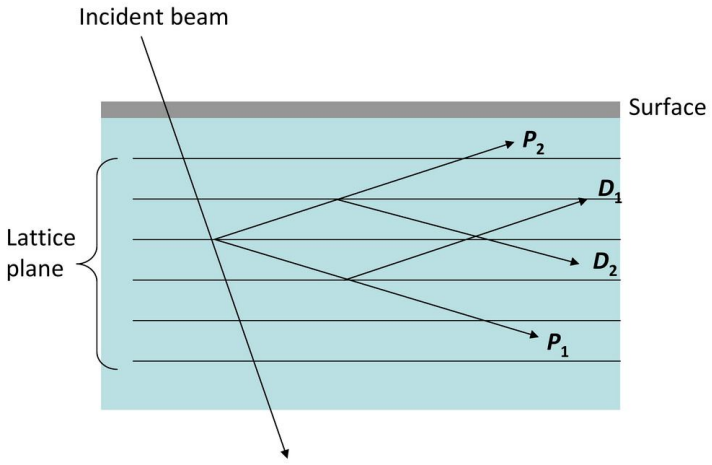

Figure 3.16 Adapted from [79]. Schematic showing the formation of Kikuchi lines.

Finally, when we grow metal films on an untreated Si(111) substrate, the resultant film will be polycrystalline. The RHEED pattern of a polycrystalline film emerges as concentric rings (See **Fig. 6.11a** in chapter 6). Since the polycrystalline film is composed of many different crystallites with different orientations, the film is thus usually rough. In this case, the electrons penetrate through crystallites (**Fig. 3.17a**) and a transmission electron diffraction pattern is formed. In a polycrystalline film all islands have their own crystal orientations which are not correlated to each other. The reciprocal space is therefore the sum of individual reciprocal spaces with different orientations. When the crystallites are randomly oriented, the resultant reciprocal lattice from the summation of unrelated individual reciprocal structures will be a set of concentric spheres. [80 - 82] As the Ewald sphere cuts through these concentric reciprocal lattice spheres the intersections will form the ring pattern accordingly. (**Fig. 3.17b and c**).

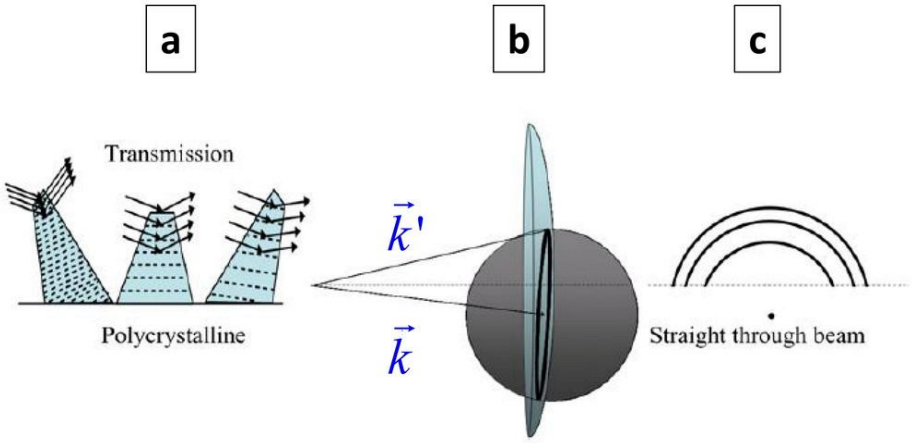

Figure 3.17 From [80]. Schematic showing electron scattering through a polycrystalline film. **(a)** A polycrystalline film. **(b)** Ewald construction for electron diffraction through a polycrystalline film. The dark shaded sphere represnts the reciprocal lattice structure from a polycrystalline film that contains randomly oriented crystallites. **(c)** The resultant ring pattern of RHEED taken on a polycrystalline film.

Chapter 4: Thick Ag Films as an Ideal Platform for Plasmonics*

As discussed in Chapter 1, growth of high-quality metal films with single crystallinity and atomic smoothness is a very challenging job in surface science. Nonetheless, it is a very important research topic. Its importance not only lies in helping surface scientists to understand complicated growth mechanism, but also in the field of plasmonics since it provides the technique to prepare high-quality plasmonic materials most plasmonic researchers are unable to achieve, thus helping tremendously in the progress of plasmonic research (see Chapter 2).

A magic method to prepare atomic flat metal films on semiconductor substrate is called the "two-step" method, *i.e.* growing the film at a low temperature with a subsequent annealing to room temperature (RT), as discussed in Chapter 1. But a difficulty in applying this method to the preparation of plasmonic metal films is that plasmonic films require a thickness more than the skin depth of the specified metal (usually thicker than 50 nm for commonly used plasmonic metals such as Ag and Au in the spectrum of visible light) but the study of two-step process rarely goes beyond a few monolayes. Therefore, even if the two-step method has already been proved to be capable of growing atomic flat epitaxial metal films on a variety of substrates, it does not necessarily mean that a thick film grown using this method can also be atomic smooth. Exploring new methods to grow thick, epitaxial Ag films with atomic smoothness is thus not a trivial quest, but plays an important role in advancing the development of Ag-based plasmonics. In this chapter I am going to report our progress in the growth of thick epitaxial Ag films with the desired atomic smoothness.

---

* Part of the work in this chapter was published. See Thomas Hartsfield *et al*. "Semiconductor Quantum Dot Lifetime Near an Atomically Smooth Ag Film Exhibits a Narrow Distribution" *ACS Photonics* **3**, 1085 (2016). In this work I prepared an atomically flat Ag film (40 nm thick) capped by Al_2O_3/MgO for the study of quantum dot lifetime.

4.1 Thick Films Grown by the Two-step Method

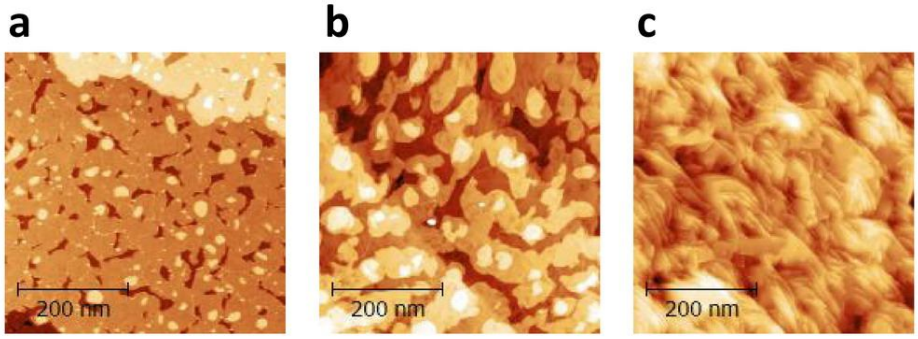

Figure 4.1 STM images of **(a)** 20 ML, **(b)** 40 ML, and **(c)** 80 ML Ag films grown on Si(111), all by the two-step method in one shot. The RMS roughness of each film is **(a)** 0.09 nm, **(b)** 0.11 nm, and **(c)** 0.21 nm, respectively.

In the literature review in Chapter 1 we note, as the two-step method applies to the growth of Ag on Si(111) with a coverage more than the critical thickness (6 ML Ag in this case), the resultant Ag film will form a complete overlayer on top of the Si substrate with an atomically smooth morphology - the film perfectly follows the step of the underlying substrate with 1 ML islands or pits on the terrace. But as the coverage increases further the film will gradually become rougher due to the lesser influence of the "electronic growth mechanism" when the film becomes thicker. A question arises naturally in this context: What thickness of the film one can grow using the two-step method before the film fully loses the atomic smoothness? To attack this question we designed a series of experiments in which we grew 20 ML, 40 ML, and 80 ML Ag on Si(111) using the two-step method (films are grown at 90 K in one shot with a subsequent annealing to RT). **Fig. 4.1** shows the STM images of these three films. 20 ML Ag perfectly preserves the atomic smoothness. 40 ML Ag is still atomic flat though it starts to show a little more complicated structures and multi-layer islands and pits. Interestingly, 80 ML Ag com-

pletely loses the atomic flatness - it shows a very different morphology than 20 ML and 40 ML films. It is also very different from the room-temperature-grown films following the SK mode (flat islands with meandering grooves down to the wetting layer).

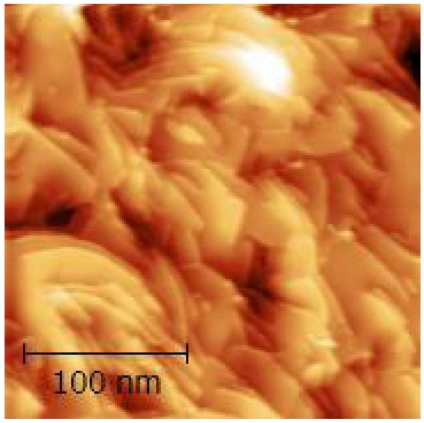

Figure 4.2 Zoom-in STM image of 80 ML Ag grown on Si(111) using the two-step method. The surface is very rough with high densities of dislocations and pits.

With a closer inspection of this film, as shown in **Fig. 4.2**, the zoom-in STM image, we see that the structure of the film is very rough, with a high density of pits and crevasses. Apparently the film does not follow the SK growth mode. Since the film is grown at 90 K, the low temperature limits the mobility of the Ag atoms to move kinetically to the thermodynamically stable state, *i.e.* the growth of 3D islands after the completion of the wetting layer. Instead, the atoms are "frozen" to where they land on the surface with a high density of nanoclusters. By this manner the low-temperature deposition cut off the route for the film to relieve the strain from the mismatch with the substrate through the formation of 3D islands. Thus, in the subsequent annealing to room temperature, the film needs to relieve the strain through other mechanisms, which lead to the creation of a highly rough structure and a high density of dislocations and pits. The cause of the un-

evenness of the film not only comes from the necessity of strain relief, but also from the fact that the electronic mechanism is much weakened in this thicker film, thus failing to stabilize the film and to maintain its flatness.

STM studies were carried out by my colleague Dr. Chendong Zhang. I express my gratitude to him.

This thickness-dependent experiment shows that it is not possible to grow an atomically smooth thick film using the two-step method. Beyond 80 ML (or some coverage less than 80 ML, considering that there might exist a "threshold thickness" located between 40 ML and 80 ML beyond which the film will lose atomic smoothness), the film grown by the two-step method will completely lose the atomic smoothness. However, one may avoid this "one-shot" growth, *i.e.* growing the film directly to its desired thickness, but instead, grow only 20 ML or 30 ML each time until the film reaches the desired thickness. Therefore, one method we conceive, still using the two-step method, is to grow the film no more than 30 ML at 90 K with a subsequent annealing to RT during a cycle of the two-step growth. The growth is repeated until the desired thickness is reached. In **Fig. 4.3**, the RHEED pattern of the 40 nm Ag (**Fig. 4.3b**) shows sharp streaks representing a long-range, well-crystallized nature of the film, and the AFM image (**Fig. 4.3c**) of the same film after being capped by Al_2O_3/MgO (the capping is crucial to preventing rapid degradation of epitaxial film due to surface oxidation in ambient conditions. See Chapter 5 for detailed discussion) shows a surface morphology of atomic smoothness, with a small RMS roughness (0.22 nm), both confirming the single-crystallinity and the atomic flatness of the film. However, it is noticeable that RHEED streaks on the 40 nm film (**Fig. 4.3b**) are broader than on the 20 ML film (**Fig. 4.3a**), indicating that the thick film is in general rougher than the thin film.

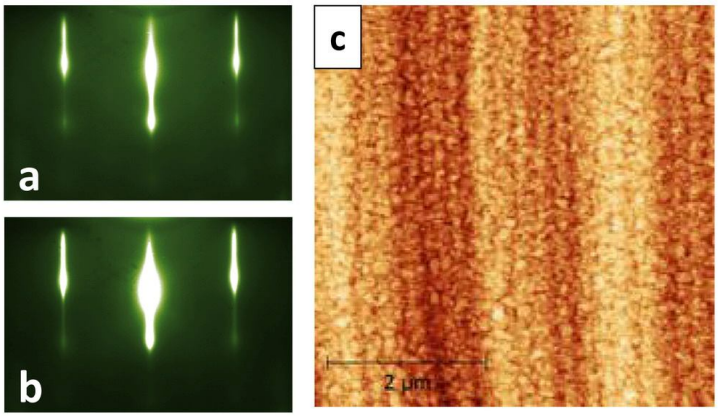

Figure 4.3 RHEED on **(a)** 20 ML Ag and **(b)** 40 nm Ag grown on Si(111). RHEED patterns of both are taken on the same film. The thick, 40 nm Ag film is grown by a repeated two-step manner, in which only 20 ML Ag (or less) is grown in each growth cycle until the desired thickness is reached. RHEED in **(a)** is taken after the first cycle of growth and RHEED in **(b)** is taken after the last cycle of growth. **(c)** AFM image of the 40 nm Ag capped by 2.0 nm Al_2O_3 and 1.5 nm MgO. The RMS roughness of the film is 0.22 nm.

Our refined two-step Ag films show excellent optical properties. Yanwen Wu *et al.* probe the film's intrinsic optical properties by using spectroscopic ellipsometry (SE). [45] **Fig. 4.4b** shows dielectric functions ε' and ε'' of the Ag film (thickness = 40 nm, without capping layers). The sharp rise in ε'' around 4 eV corresponds to the onset of the *d*-band transition in Ag. Also shown in the figure are reported values of ε'' by JC. JC data show the lowest reported plasmonic losses in Ag, [39] while the data from generally-cited Palik's handbook [40] are more realistic. **Fig. 4.4c and d** compared the measured results of ε'' for the epitaxial film (capped by Al_2O_3 and MgO) and that of the conventionally thermally evaporated film (thickness of both films = 45 nm). Not surprisingly, the thermal film shows higher ε'' than the epitaxial film due to its surface roughness and polycrystallinity (both contribute to more inelastic scattering). The significance in the measurement is that the ε'' values from our epitaxial film are even lower than those from JC data in the

visible light range. The capping layers (Al_2O_3 and MgO), as expected, have no significant effect on the film's intrinsic properties. Overall, SE measurements confirm that our epitaxial films have a significantly lower intrinsic damping than thermal films and that from widely-cited Palik's data. However, the most substantial consequence of low loss of our epitaxial films is that they significantly reduce the SPP scattering, which can be demonstrated by measuring the surface plasmon polariton (SPP) propagation length. The measurement was carried out on a 45 nm epitaxial Ag film by Yanwen Wu *et al.* The propagation length at 632 nm is measured to be 22 μm and at 880 nm the propagation length is 42 μm. Theoretical simulation shows that the propagation on a 200 nm thick Ag film is much longer (247 μm at 632 nm and 755 μm at 880 nm) than the measured values. This is because the thickness of the film, 45 nm, is close to the skin depth of Ag, and therefore for SPPs propagating in the film there is significant radiation leakage into the substrate.

To demonstrate the potential of our epitaxial, two-step-grown Ag films in plasmonic research, Thomas Hartsfield *et al.* carried out an experiment in which they placed CdSe/CdS core/thick-shell giant quantum dots (gQDs) on an atomically smooth epitaxial Ag film I prepared (the one in **Fig. 4.3**). [83] In comparison, gQDs were also transferred to a thermally evaporated rough Ag film (also 40 nm in thickness, RMS roughness = 3.57 nm) and a glass substrate. The lifetime measurement of gQDs on each of the three different substrates was carried out on many individual gQDs and the distribution of lifetime can be plotted accordingly, as shown in **Fig. 4.5**. The average gQD lifetime and standard deviation extracted from the statistical analysis of these measurements can be summarized as follows: 0.6 ± 0.2 ns (epitaxial Ag film), 6 ± 2 ns (rough thermal film), and 33 ± 11 ns (glass). Apparently the lifetime of gQDs placed on an atomically smooth epitaxial Ag film displays both a greater reduction in lifetime and a significantly narrower distribution of lifetime. This study demonstrates that atomically smooth epitaxial Ag films can

serve as an ideal platform for reliable control over the QD lifetime and may lead to improved photodetectors and light emitting devices requiring fast response or modulation.

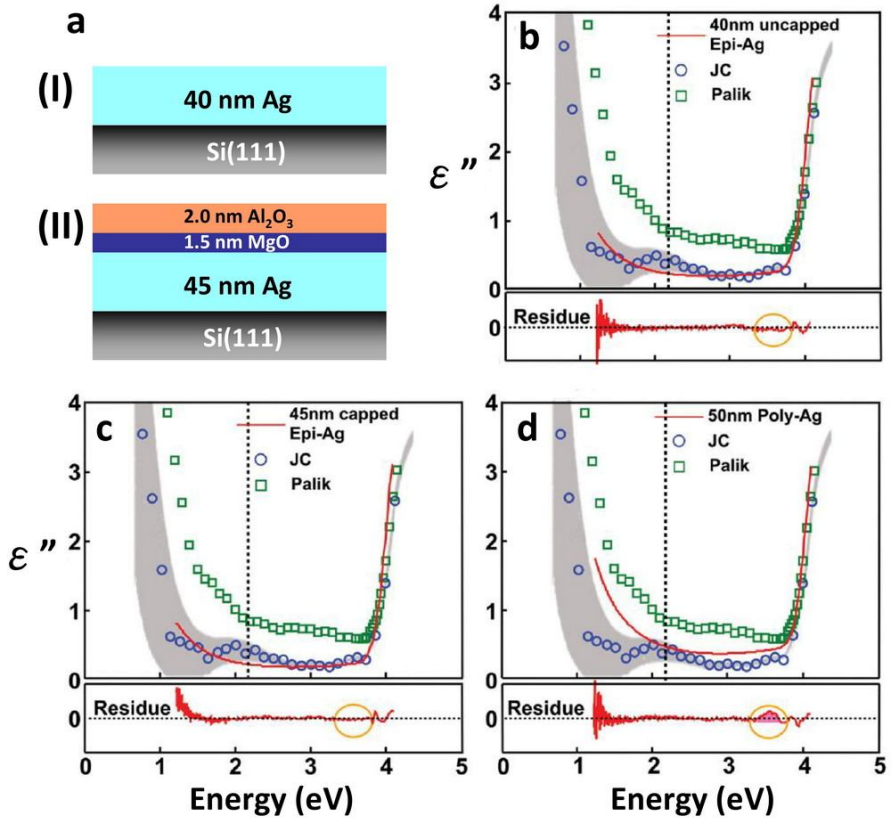

Figure 4.4 From [45]. **(a)** Schematic of two epitaxial Ag films. **(I)** is the 40 nm epitaxial Ag without capping. **(II)** is the 45 nm epitaxial Ag film capped by Al_2O_3/ MgO. **(b)** Energy dependence of the imaginary part of the dielectric function of Ag, ε", extracted from the SE measurement carried out on sample **(I)**, the uncapped 40 nm epitaxial Ag film. **(c)** ε" of Ag measured on sample **(II)**, the 45 nm epitaxial Ag film capped by Al_2O_3/ MgO. **(d)** ε" of Ag measured on an uncapped 50 nm thermal film deposited at a rate of 0.35 nm/s. The vertical dashed lines in **(b - d)** indicate the energy at which ε" for the epitaxial film is ~ 2 times smaller than that from JC's measurement. The light grey shade represents the errors in the JC data. Fitting residues are plotted below **(b)**, **(c)**, and **(d)**.

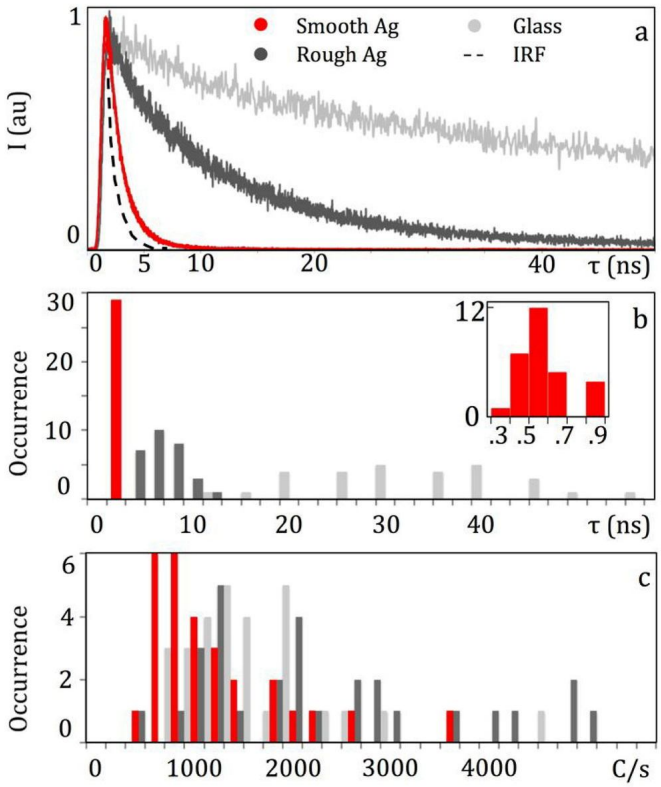

Figure 4.5 From [83]. Statistical analysis of photoluminescence (PL) of gQDs on glass, rough Ag and smooth Ag: **(a)** A typical PL lifetime measurement of a single gQD on each substrate. **(b)** Statistical distribution of gQD PL lifetimes on each substrate; inset shows a detailed distribution of gQD lifetimes on smooth Ag in ns. **(c)** Statistical distributions of average PL intensity on each substrate.

4.2 Thick Films Grown with an Efficient Method Combining Fast Deposition and Post Annealing

Although the repeated cycle of the two-step growth discussed in the previous section can successfully grow high-quality Ag films for plasmonic studies, it poses two serious shortcomings:

(1) It is very time-consuming. The growth of a new cycle should wait until the film is fully returned to the room temperature from the previous cycle. Mostly one can only run one or two cycles a day. Since each cycle allows very little coverage (less than 30 ML) to grow compared with the target thickness (more than 40 nm), a lot of cycles are needed before reaching the target thickness. If thicker films are to grow, such as one thicker than 100 nm, the days needed to prepare a sample will make this method completely infeasible.

(2) Even if the repeated running of the two-step method can achieve a high-quality film, it nonetheless cannot avoid the deterioration of the film quality after a few cycles of growth. The STM image of the 40 nm Ag (**Fig. 5.5c** in Chapter 5) shows a pretty "rough" surface with multi-layer islands and pits, compared with the genuinely "atomic smooth" film with only single-layer islands and pits, though such two-step films are still much better in the perspective of plasmonic research compared with commonly used thermal films in the field.

Due to these difficulties, growing an epitaxial Ag film of thickness in the range of 40 nm - 50 nm by the repeated two-step process can already be a very demanding task, and the growth of a much thicker film with thickness of several hundreds of nanometers will be unrealistic altogether. However, as demonstrated in the previous section, the SPP propagation length is serious limited on a 45 nm Ag film because the film is too thin to fully support the SPP mode - a significant loss occurs due to radiation leakage to the substrate. Therefore, it is imperative to grow a much thicker film than the ones we currently prepared by the two-step method if we are going to expand the applicability of the films in plasmonics. Due to these constrictions posed by the two-step method, we need to find a new, more efficient method to grow epitaxial films with thickness in the range of hun-

dreds of nanometers while the film quality (in terms of crystallinity and surface smoothness) can still be comparable to the two-step films.

Before designing a new method to realize the growth of thick, atomically smooth epitaxial films with significant reduction of preparation time, we may first go through literature about growth of thick Ag films and see what techniques learned from these earlier studies can help us design a new method.

Logeeswaran VJ *et al*. showed that a mediating Germanium (Ge) layer deposited onto a SiO_2/Si(100) (SiO_2 is the native oxide layer) prior to the deposition of Ag can significantly reduce the roughness of the film. [84] In the experiment they used a conventionally thermal deposition system (base pressure is about 10^{-6} Torr) equipped with E-beam evaporators. All depositions are carried out at room temperature. In the experiment they deposited 2 nm Ge onto the SiO_2/Si(100) substrate and then 15 nm Ag. To compare, they also prepared a sample with a direct deposition of 15 nm Ag onto SiO_2/Si(100). From AFM images and surface height distributions the authors showed that the Ge-mediated Ag film (RMS roughness is 0.6 - 0.8 nm) is far smoother than an Ag film directed deposited on the oxide substrate (RMS roughness is 6 - 8 nm).

Another method to produce smooth Ag films is by doping the film with a different material during film growth. Deen Gu *et al*. showed that an Ag film (thickness = 15 nm) grown on SiO_2/Si(100), with a continuous doping of aluminum (Al) during growth, exhibits far smoother morphology (RMS roughness is about 0.43 nm) than a pure Ag film (RMS roughness is 6.87 nm) of the same thickness also grown on SiO_2/Si(100). [85] Moreover, the authors also showed that the Al-doped Ag film (15 nm in thickness) is thermally stable - the film can endure an annealing temperature as high as 300 °C without dewetting due to a thin capping layer of aluminum oxide spontaneously formed on the surface of the film.

The mechanism to form a smooth Ag film by either Al doping or a Ge-mediating layer is possibly through the enhancement of the density of nucleation sites. However, both Al and Ge are not appropriate materials in the regime of visible wavelengths. Al will cause tremendous absorption of visible lights due to its interband transition at about 1.4 eV (~ 800 nm, in the infrared regime. See Chapter 2) and Ge, despite a semiconductor, has a narrow band gap (0.67 eV) [86] and can also cause unexpected absorption. Therefore we will not consider either method to grow thick films. But since both of them indicates the significance of preparing a smooth film by increasing the density of nucleation sites, an alternative we think can achieve the same purpose is by dramatically increasing the deposition rate (much higher than that employed in the two-step growth), as we learned from the general growth mechanism in Chapter 1.

Another novel method, called "template stripping", to prepare smooth Ag films (and high-definition nanostructures on the film) is developed by Dr. David J. Norris' group. [87, 88] First, the film of a desired plasmonic material such as Ag or Au is deposited onto a well-cleaned Si substrate (served as the "template"). Secondly, a layer of epoxy is deposited (coated) over the metal film. Finally, the entire film, along with the epoxy coating, can be peeled off from the Si template. The freshly exposed surface originally in contact with the template will have a much smoother morphology than the surface of a directly deposited film. Since our purpose is to grow a smooth film directly on the Si substrate, we will not consider this method, although this method may improve the surface quality of widely-used thermal films.

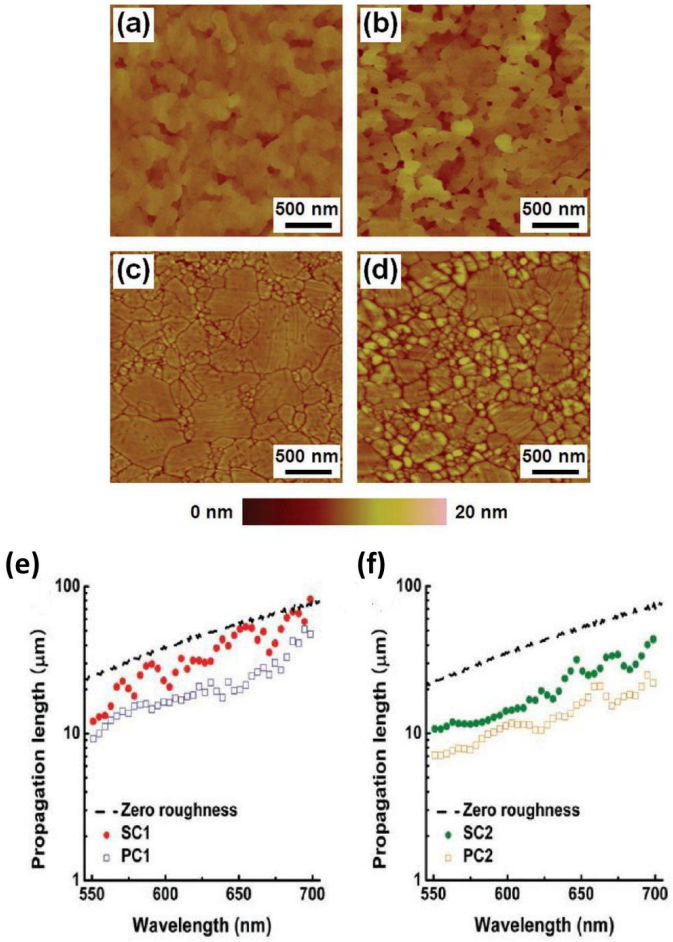

Figure 4.6 From [89]. AFM images of single-crystalline Ag films [**(a)** 100 nm, labeled as SC1 and **(b)** 200 nm, labeled as SC2 by the authors] and polycrystalline Ag films [both are 200 nm, engineered with different roughness qualities. **(c)** is labeled as PC1 and **(d)** is labeled as PC2 by the authors]. These films have RMS roughness of 0.82 nm, 1.30 nm, 0.81 nm, and 1.39 nm, respectively. **(e)** SPP propagation lengths on a single-crystalline Ag film (SC1) and poly-crystalline Ag film (PC1). The dashed line is the predicted propagation length using the measured dielectric function of SC1, as well as assuming only Ohmic losses and no roughness. **(f)** SPP propagation lengths on a single-crystalline Ag film (SC2) and poly-crystalline Ag film (PC2). The dashed line is the predicted propagation length using the measured dielectric function of SC2, as well as assuming only Ohmic losses and no roughness.

Interestingly, Dr. David J. Norris' group also explored methods to grow single-crystalline Ag films. [89] In this work Jong Hyuk Park *el al*. grew Ag films on mica in a sputtering system (base pressure is about 10^{-6} Torr). The deposition rate is set to the maximal value the system can cope with, which is 1.65 nm/s. The purpose of this intentional choice of the highest deposition rate is not only to increase the density of nucleation sites, but also to reduce the effect of grain boundary pinning due to relatively high concentration of impurities in the sputtering chamber. [62] To grow single-crystalline Ag films, the authors deposited Ag at a substrate temperature of 350 °C. Single-crystalline films can be grown as the substrate temperature is above 300 °C, but they found that the film can be particularly smooth as the substrate temperature is at 350 °C, rather than other temperatures. At a lower substrate temperature the mobility of Ag atoms may not be high enough to form a smooth surface while at a higher temperature the film may start to dewet. The resultant films, with thickness of 100 nm and 200 nm, have RMS roughness of 0.82 nm and 1.30 nm, respectively. It is noticeable that the authors also prepared polycrystalline films with similar roughness as single crystalline films for comparison. Although the RMS roughness is not different, AFM images of single crystalline films show much smoother morphology than those of polycrystalline films. (**Fig. 4.6a - d**) The propagation measurement, as expected, demonstrated that single crystalline films have longer propagation length (because of significantly reduced scattering by grain boundaries). The measurement is summarized in **Fig. 4.6e and f**.

I intensively searched for literature of thick film growth but unfortunately it seemed that no groups I surveyed so far did achieve the growth of atomically smooth films. However, we may still summarize what we learned from these earlier studies:

(1) Increasing the density of nucleation sites during growth shall improve the surface smoothness. Researchers achieve this by doping the Ag film with a different material

during growth or growing a mediating layer prior to Ag film growth. Instead of using either of these methods, we may simply increase the deposition rate to a much higher value than currently used one in the two-step growth (~ 1 Å/min).

(2) The substrate temperature is crucial to determine whether the film will be single crystalline or polycrystalline, as well as the smoothness of the film. In the study of Ag films grown on mica, the authors found that the best substrate temperature to grow a smooth single-crystalline Ag film is at 350 °C. To simplify the growth method, we decide to grow films at room temperature with a post-growth annealing at an elevated temperature. The choice of annealing temperature is tricky - it shall be high to allow Ag atoms enough mobility to "smooth out" the surface, but should not be too high or the film will be dewetted.

To help us design a feasible scheme of room temperature growth with a subsequent high-temperature annealing (all conducted in UHV), we also surveyed the published study of Ag film dewetting. Unfortunately most studies were carried out on very thin Ag films (a few monolayers). [57, 90] Charlotte E. Sanders *et al*. showed that a 10 ML Ag grown on Si(111) will dewet at an annealing temperature as low as 50 °C. [57]

To investigate the thermal stability of Ag films, H. C. Kim *et al*. used the *in-situ* four-point probe technique to monitor the resistivity of an Ag film while ramping up the temperature of the film. [91] The films were thermally deposited on SiO_2 using electron-beam evaporation. The resistivity measurement versus temperature shows a steep increase of resistivity of the film once the temperature is above some specific value (depending on the thickness of the film) - which is defined as the "onset temperature". The onset temperature for a 35 nm Ag is about 102 °C and for 69 nm about 203 °C. The steep increase of the resistivity of the film above the onset temperature indicates that the film is thermally unstable above this temperature. In other words, the film is dewetted. Interest-

ingly, the authors did not observe any steep increase of the resistivity within temperatures of study (up to 600 °C) once the film is thicker than 85 nm. The results are summarized in **Fig. 4.7**.

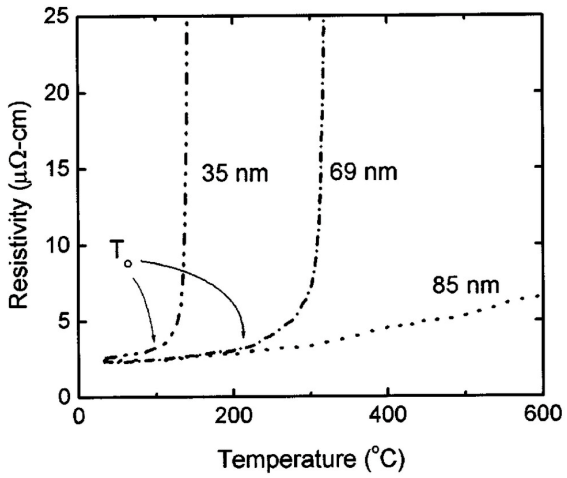

Figure 4.7 From [91]. Resistivity as a function of temperature for various film thicknesses of Ag on SiO_2 annealed in a vacuum at 0.1 °C/s.

Although the absence of onset temperature of Ag films thicker than 85 nm is dubious, and although the study was carried out on Ag films grown on SiO_2, rather than Si(111), results from H. C. Kim *et al*. are still valuable for us to consider appropriate annealing temperatures: (1) As the film is thicker, the onset temperature of dewetting will be higher. (2) Once the temperature is above the onset value, the steep increase in resistivity indicates that dewetting of the film can proceed very rapidly.

In 2002 the former lab member Professor Hongbin Yu and coworkers conducted an experiment in which they studied dewetting behavior of thin, two-step-grown Ag films on GaAs(110). [63] Thin films about or less than 6 ML are highly unstable - even in the UHV environment - that they show spontaneous dewetting which proceeds with time after they are warmed up to room temperature following low-temperature growth (see **Fig.**

5.1 in Chapter 5). Surprisingly, a thicker, 25 ML Ag shows an opposite behavior - it becomes smoother as it stays longer in UHV after warm-up to room temperature. Moreover, the 25 ML Ag film can even be smoothed further by annealing the film at 385 K (**Fig. 5.2** in Chapter 5). They observed that on the thin film ($\leqq$ 6 ML), dewetting is launched from the sites of elongated and narrow rectangular-shaped "slits" (voids) which reach down to the GaAs substrate (Ag does not "wet" GaAs). In opposite, 25 ML Ag is thick enough to completely cover the substrate without deep pits down to the substrate, which may render the film thermally stable even in an elevated temperature. In brief, the thermal stability of a thin film can be significantly improved if the film is thick enough to completely cover the substrate. By applying appropriate annealing temperature, the film can be smoothed out rather than get dewetted.

While the previous study was carried out on Ag films grown on GaAs(110), to test the thermal stability of Ag films with similar thickness on Si(111), we grew a 30 ML Ag film on Si(111) using the two-step method. The STM images in **Fig. 4.8** show that the film is thermally stable after it is annealed to 300 °C for 1 hour in UHV. The little dots on the surface after annealing possibly come from slight contamination during annealing. Therefore, to anneal a thick Ag film of several hundreds of nanometers in thickness, the film shall be heated up to above 300 °C. However, the annealing temperature shall be very carefully controlled since the film can dewet rapidly once heated up above its dewetting onset temperature.

Overall, our new method comprises two steps, which will fully circumvent the two-step process: (1) The film is grown at room temperature with a high deposition rate (30 Å/min). (2) The film is annealed at about 400 °C for 30 minutes. The film is annealed by an e-beam bombardment heating stage.

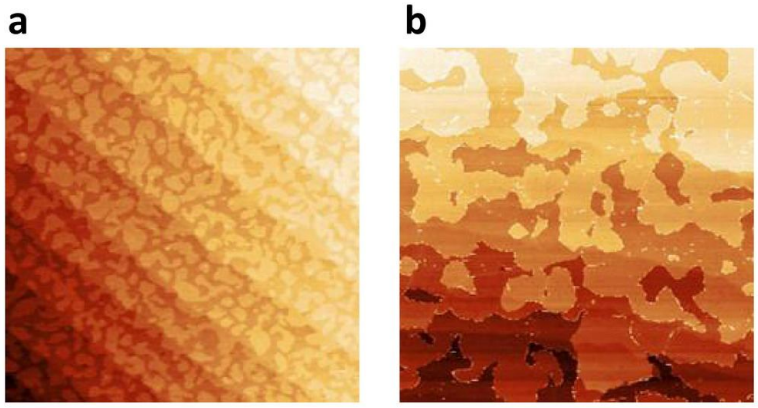

Figure 4.8 STM images of **(a)** 30 ML Ag deposited on Si(111) using the two-step method, and **(b)** the same film after annealing at 300 °C for 1 hour. The film does not dewet after annealing, indicating that it is thermally stable under a temperature of 300 °C. Image size of both **(a)** and **(b)**: 1 μm × 1 μm.

Fig. 4.9a shows the RHEED pattern of the 150 nm Ag film grown on Si(111) at room temperature with a deposition rate of 30 Å/min. **Fig. 4.9b** is the corresponding STM image of the film. As expected, the film is rough with large "mounds". However, the film is well-ordered - the mounds are round with a layered, "wedding-cake" structure. The top of mounds is atomically flat. The wedding-cake structure is the manifestation of the step barrier, which is commonly observed on the growth of Ag films as discussed in Chapter 1. A very interesting feature in RHEED of the film is that the RHEED still shows sharp streaks from the (111)-(1 × 1) surface structure. It means that the film, despite its roughness, still preserve a good crystallinity. The sharpness of the streaks indicates that the *domains* are large. In other words, These *domains* might be related to the large mounds on the thick film's surface. Because the size of the mounds (about 100 nm laterally and 5 nm in height) is very probably beyond the coherent length of the electron beam, the elec-

tron beam can only "discern" a local crystalline structure and hence gives rise to the streak pattern reflecting the (111)-(1 × 1) structure.

Here we note that the intensity along the streaks in **Fig. 4.9a** is not homogeneous - there exists a bright spot on each of the streak. This pattern has some similarity to the pattern taken on the as-grown Ag at 90 K (**Fig. 3.13a** in Chapter 3), indicating that there are some three-dimensional contribution to the diffraction pattern due to the scattering of the electron beam involving a few layers into the film along the *z* direction. The difference between this case and that of the as-grown Ag at 90 K is mainly about the size of Ag clusters on the surface. The size of mounds on the thick film is much larger (about 100 nm laterally with the height about 5 nm) than the size of nanoclusters on the as-grown Ag at 90 K (about a few tens of Å both laterally and in height). Therefore, the *domains* on the as-grown low-temperature Ag film are much smaller, giving rise to the relatively large spots in the RHEED pattern. The lack of the streak-like RHEED pattern on the as-grown Ag film at 90 K comes from the fact that the electron beam penetrates more deeply into the film due to these nanoclusters and hence the contribution from *z*-direction scattering to the RHEED pattern is enhanced and gives rise to round spots rather than elongated streaks. Finally, in a smoother, two-step film, the RHHED pattern shows streaks with more homogeneous intensity (see **Fig. 5.5a** and **Fig. 5.6a** in Chapter 5). The difference between the smooth film and the rough thick film is that a smoother film may cause less scattering from *z*-direction penetration, making the diffraction on the smooth surface more like an ideal two-dimensional case which gives rise to streaks with homogeneous intensity.

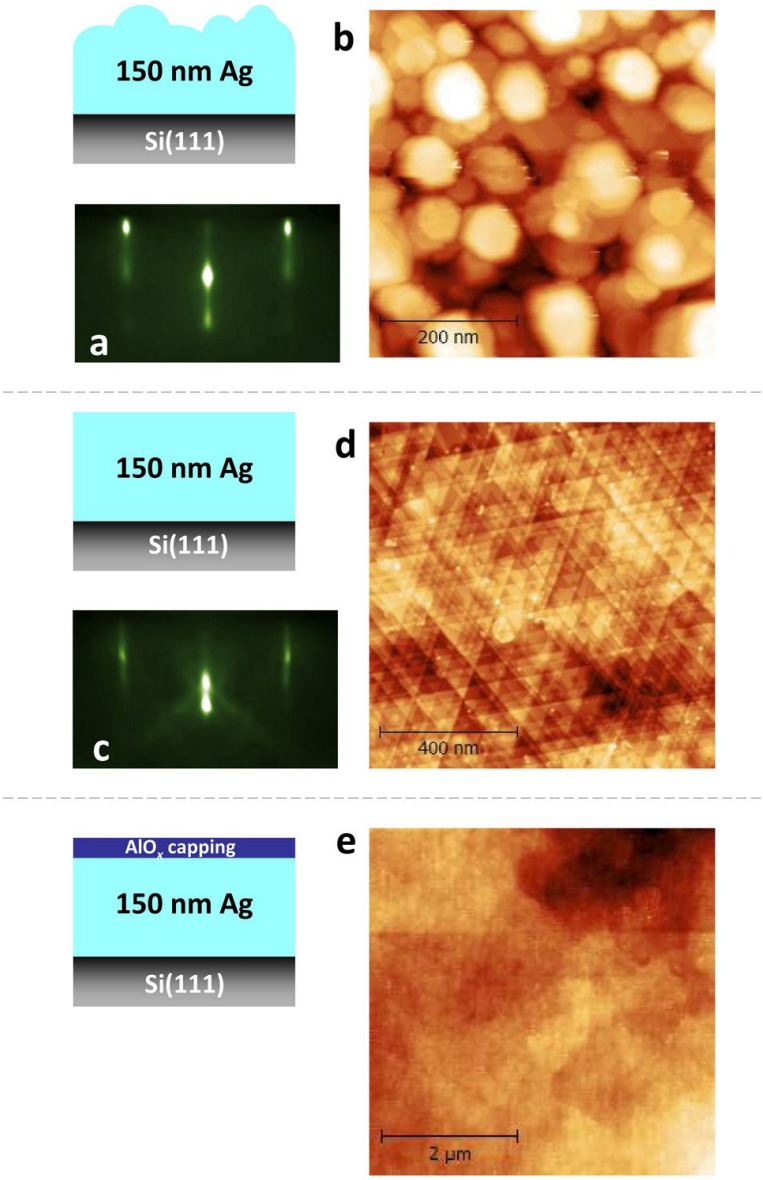

Figure 4.9 **(a)** RHEED on 150 nm Ag grown on Si(111) at room temperature with a high deposition rate, 30 Å/min . **(b)** The corresponding STM image of the rough, room-temperature-grown film. RMS roughness of the film: 1.95 nm. **(c)** RHEED on the same film after it is annealed at about 400 °C for 30 minutes. **(d)** STM image of the "smoothed" film after annealing. RMS roughness: 0.27 nm. **(e)** *Ex-situ* AFM image of the annealed 150 nm Ag film capped by a thin AlO_x layer (about 1.0 nm thick). RMS roughness is about 0.4 nm.

Fig. 4.9c and d show RHEED pattern and STM image after the thick film (150 nm) is annealed at about 400 °C in UHV, respectively. Very interestingly, the film smoothes out to the (nearly equilaterally) triangular structure after annealing. The triangular surface morphology might be the most stable state when the atoms have high enough mobility to diffuse on the surface to "smooth out" the surface before the onset of dewetting. The formation of the triangular morphology might be associated with the underlying Si steps and the strain in the Ag film originating from the Ag-Si heteroepitaxy. Interestingly, similar phenomena are also observed in the thick Pb film grown on Si(111). Therefore, the mechanism behind the formation of the triangular structure may be more related to the kinetics of the diffusion of atoms on the surface and thermodynamic stability of the triangular structure, rather than properties related to specific materials such as electronic structures of the material. One possibility that the triangular pattern is favored rather than the round-mound structure (the favored morphology following the SK mode) is that triangles form a more compact structure than mounds. As shown in the zoom-in STM image in **Fig. 4.10** on the same film, triangular "flakes" perfectly align with each other with single-layer height difference among neighboring triangles. In opposite, mounds can never form a compact structure - there are inevitably deep "crevasses" among neighboring mounds. Moreover, among equilateral polygonal structures, equilateral triangles are favored rather than other polygons such as squares and hexagons because triangles can form the most possibly compact structure. However, a complete picture to describe the mechanism of the formation of the triangular surface morphology on a thick metal film after elevated-temperature treatment needs a more thoroughly theoretical studies such as calculations and simulations to show that the equilaterally triangular structure is indeed the most stable state.

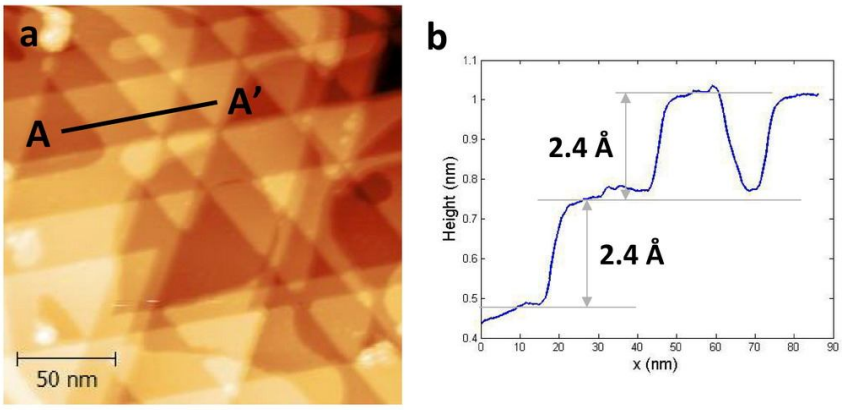

Figure 4.10 **(a)** Zoom-in STM image of 150 nm epitaxial Ag after annealing at ~ 400 °C. The arrangement of a nearly perfect equilateral triangular structure can be clearly seen. **(b)** The line profile along AA' in **(a)** shows that neighboring triangular flakes have a height difference of a single layer of Ag(111), which is about 2.4 Å.

The RHEED pattern on the thick Ag film after annealing shows Kikuchi lines, indicating that the film possess excellent crystallinity with perfect surface and perfect bulk lattice structure (see discussion in Chapter 3). To complete the study, we capped the film with a thin AlO_x overlayer (see Chapter 5 for the capping method). The *ex-situ* AFM image (**Fig. 4.9e**) of the film shows an atomically smooth morphology after capping (RMS roughness is about 0.4 nm), suggesting that the film can readily serve as an ideal platform for plasmonic study.

In this section we demonstrated a new method, with much higher efficiency compared with the time-consuming two-step method, to grow thick Ag films with atomic smoothness and nearly perfect crystallinity. There are still a lot of questions yet to answer about the growth mechanism of this method. During annealing, the role of strain in the Ag film and the interface structure between Ag and Si in this heteroepitaxial system shall be further studied. Very intriguingly, our collaborators, led by Dr. Wen-Hao Chang in

National Chiao Tung University in Taiwan, observed lasing behavior at 4 K on a nanostructure of rectangular InAsP waveguides with four layers of strained InGaAsP QDs embedded in the nanostructure, when they placed the nanostructure on our atomically smooth 150 nm Ag film (the study is out of the scope of the dissertation so I will not present the data here). We believe that in the coming future our capability in preparing high-quality thick Ag films will make huge contributions to the plasmonic community.

Annealing experiments and STM studies were carried out by my colleague Qiang Zhang. I express my gratitude to him.

Chapter 5: Capping Techniques to Stabilize Ag Films from Dewetting

In Chapter 1, we introduced a novel method called the "two-step" method to prepare atomically smooth Ag films on semiconductor substrates. In Chapter 4 we reported fast deposition at room temperature with post-growth annealing at elevated temperature to facilitate the growth of atomically smooth thick Ag films. Unfortunately, the flat morphology of these films is mostly in a metastable state, *i.e.* films will start to dewet and roughen as they find channels to move to an energetically more stable state. That means, films can degrade even in UHV at room temperature. Most atomically flat films by the two-step method cannot survive the "hostile" ambient environment. It is therefore imperative to find methods to stabilize these films in order to make them more applicable in important fields such as device manufacturing, nano-photonics and plasmonics, and biosensing. In this Chapter I am going to review studies of thin film dewetting relevant to my research and report methods successfully developed in Shih Lab to stabilize these atomically smooth epitaxial Ag films.

5.1 Dewetting of Atomically Smooth Ag Films

5.1.1 *Dewetting of Ag on GaAs(110)*

The work by Arthur R. Smith *et al.* showed the possibility of preparing atomically flat Ag films on a semiconductor substrate (see Chapter 1). [14] Hongbin Yu *et al.* further explored the stability of such thin films prepared by the same two-step technique (depositing the film at temperatures below 140 K, followed by subsequent annealing to room temperature). [63] As learned from the work done by Arthur R. Smith *et al*., when the coverage is close to the critical thickness (about 6 ML), the Ag film deposited on GaAs(110) will show flat tops with small, rectangle-shaped voids, which extend down to

the GaAs substrate. Thus, to study the evolution in UHV of the morphology of Ag films with voids, Hongbin Yu *et al.* deposited 6.4 ML Ag on *in-situ* cleaved GaAs(110) at a low temperature and annealed the film to room temperature (RT). The as-prepared Ag film showed flat tops whose thicknesses are mostly 6 ML and 7 ML, with voids (down to the substrate) interspersed over the surface. During the early stage at RT, the film evolved towards the formation of a large 7 ML area, with the consumption of the 6 ML region and also with the enlargement of the voids (**Fig. 5.1, a - c**). As the film stayed at RT for longer time it started to show the 8th, 9th and 10th layers (**Fig. 5.1, d - f**). The film slowly evolved from a 2D atomically flat structure to a 3D rough film with multilayer features.

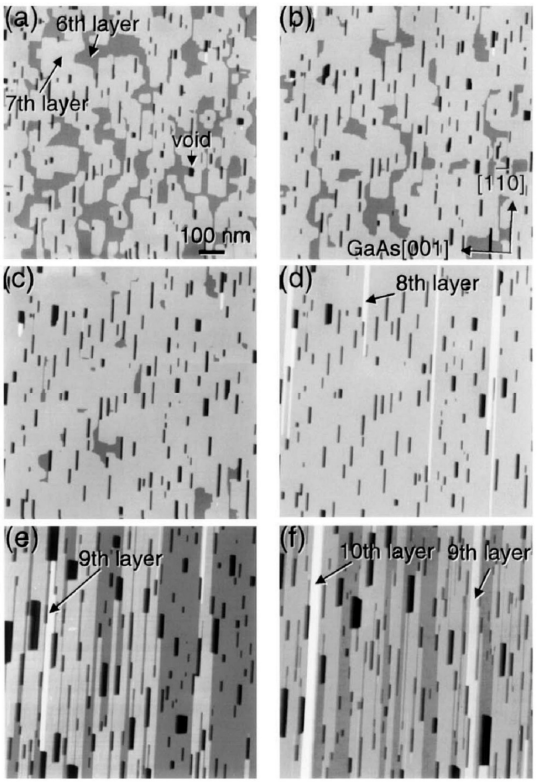

Figure 5.1 From [63]. STM images of 6.4 ML Ag on GaAs(110) taken **(a)** 162, **(b)** 292, **(c)** 422, **(d)** 1387, **(e)** 4577, and **(f)** 6363 min after warm-up to room temperature.

There are two significant features in the evolution of the Ag film with voids: (1) During the evolution, the voids are enlarged, but the density of voids does not increase. (2) Both the enlargement of voids and the formation of higher layers are highly anisotropic - they elongate more along the length rather than expand on the width.

To explain feature (1), we simply consider the formation of a void. To form a void, atoms must be continuously expelled from the void. Upward migration of Ag atoms from a void to the terrace experience a barrier which must be overcome thermodynamically. The barrier can be further reinforced considering the possibility that there exist no intermediate "shallower" voids because of the 7 ML preference due to the quantum size effect. Therefore at RT the Ag atoms are not thermodynamically mobile enough to overcome such a barrier to form new voids. To explain feature (2), M. M. R. Evans *et al.* proposed a theory in which there are two types of facets of either voids or islands and atoms on one type of the facet are experiencing less barrier to migrate upwards than atoms on the other type of the facet. [92]

The significance of the dewetting of Ag films is that it is launched from voids (or pits). Similar phenomena were also observed in Al films, which I will present in Chapter 6. It hints that, atoms aligning the edge of a void are thermodynamically more unstable and the barrier for them to migrate upwards is so small that even at RT the atoms are already mobile enough to overcome the barrier to move upwards.

The fate of Ag films will be entirely different when the coverage is increased to a degree in which a complete overlayer, which fully covers the substrate without voids, is allowed to form. As shown by Hongbin Yu *et al*. the evolution of 25 ML Ag was towards a smoother morphology when the film stayed longer at RT in a UHV environment. The film can even be smoothed further by annealing it to an elevated temperature (385 K). See **Fig. 5.2**. Due to these findings, we believed that it is possible to produce atomically

smooth films much thicker (> 50 nm) than those typically studied in two-step growth by applying appropriate annealing conditions. The relevant discussion and results have been reported in Chapter 4.

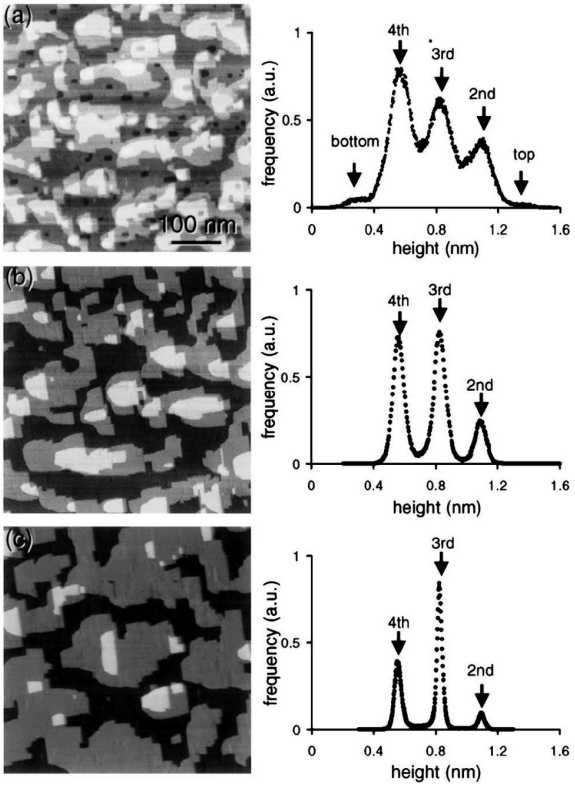

Figure 5.2 From [63]. STM images (left) and the respective height distribution (right) of 20 ML Ag on GaAs(110). **(a)** and **(b)** show that the film evolves to a smoother morphology after 13 hrs at room temperature. **(c)** was obtained after the film was annealed to 385 K for 20 min.

5.1.2 *Dewetting of Ag on Si(111) in Ambient Conditions*

Ag deposited on Si(111) by the two-step method showed a critical thickness of about 6 ML (see Chapter 1). When the coverage is higher than 6 ML, the film will completely cover the substrate with atomically flat surface (the surface is characterized by flat

terraces adorned with islands 1 ML higher and pits 1 ML lower than the terrace). Similar to the case of Ag on GaAs(110), if there are no voids on the surface, an Ag film on Si(111) will become smoother as it stays for longer time at RT in a UHV environment, as shown in **Fig. 5.3**. [37] A significant reduction in the density of both islands and pits can be observed in the STM image after the film (kept at RT) was parked in UHV for 9 days.

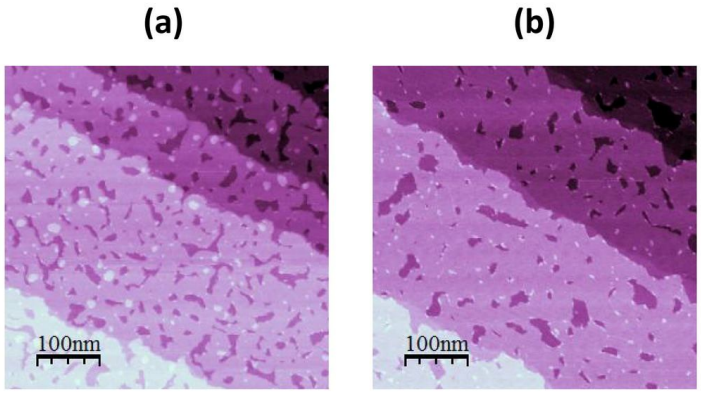

Figure 5.3 From [37]. **(a)** As-grown 10 ML Ag on Si(111). **(b)** Morphology after 9 days at room temperature, under UHV.

The reduction of the density of islands can be explained, phenomenally, by Ostwald ripening, in which larger clusters grow in expense of smaller ones. In the case of Ag islands on a terrace, the system tends to minimize the overall free energy from the edge of islands by minimizing the total length of the island edge (which is summed over all islands' edge). In this scenario small islands will decay to join either a larger island or the ascending side of the terrace. [93] Although ripening is usually a roughening process (since larger clusters accumulate), in the case of atomically smooth Ag films grown on Si(111) ripening leads to further smoothness of the film by reducing the density of small islands (in a sense, by "evaporation" of small islands).

The reduction of the density of pits can be explained by Brownian motion (random walk) of pits across individual terraces. [94, 95] The motion of pits is produced by random diffusion of atoms at the boundary wall of pits. As pits randomly walk on the terrace, they will meet to form a larger pit (the area is the sum of individual pits). As pits happen to reach the descending side of the terrace they cease to exist.

Unfortunately, even if the film can be smoothed more in UHV because of the ripening of islands and pits, it suffers overall dewetting once exposed to the atmosphere in a short scale of time. Former lab member Charlotte E. Sanders *et al.* showed that a 10 ML two-step-grown Ag film started to dewet less than one day after the film was removed from UHV! [57] The AFM image showed the emergence of pinholes surrounded by rings of mounds along the step edge. (**Fig. 5.4a**). Within a few days the film deteriorated further in the air, showing generalized roughing on terraces (**Fig. 5.4 b - d**). After five days in the air, the film was transformed to a configuration of irregular clumps tens of nanometers high. It can be considered completely dewetted at this stage.

Since an atomically smooth Ag film becomes smoother at room temperature if it is securely stored in UHV, the roughening of the film in the air is not driven by the thermal process. Possibly, chemical or other kinetic processes are drivers for ambient dewetting. Charlotte E. Sanders and coworkers also carried out X-ray photoemission spectroscopy (XPS) measurement on a 40 ML epitaxial Ag film after 36 hours exposure to the ambient environment to investigate the chemical compositions of the film. The XPS data showed no Ag oxides or sulfides within the detection limit of the measurement. It does not mean that there is no chemical reaction on the film surface, but can conservatively interpret that the oxide or sulfide layers can be no thicker than a few monolayers. Patricia A. Thiel and co-workers showed that exposure of Ag surface to trace amounts of oxygen or sulfur (say, 20 L for oxygen and a few mLs for sulfur) can already cause significant

coarsening of Ag islands with enhanced mass transport. Such accelerated mass transport results from the creation of highly mobile Ag-chalcogen clusters. [54 - 56] From these early works Charlotte E. Sanders *et al.* presumed that the dewetting of Ag films is driven mainly by the formation of highly mobile Ag oxides. [57]

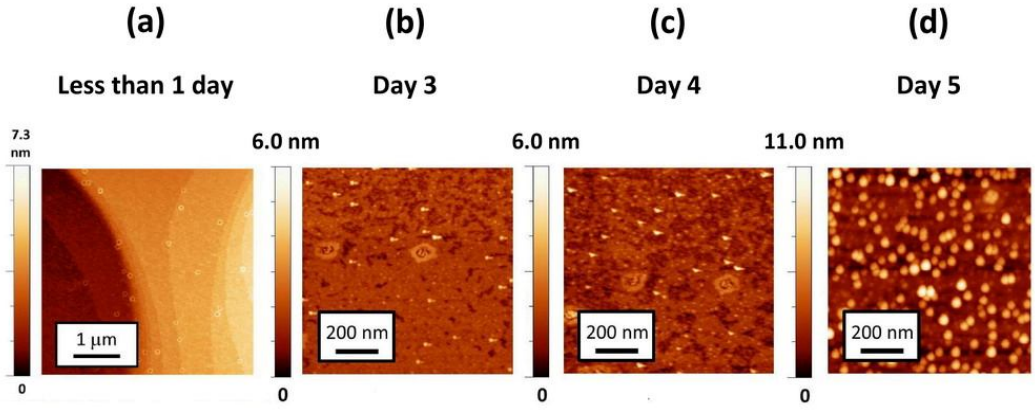

Figure 5.4 From [57]. **(a)** AFM image of 10 ML Ag on Si(111) within a few hours after removal from UHV. Pinholes surrounded by ring-shaped mounds appear. The film continues to degrade after **(b)** 3 days, **(c)** 4 days, and **(d)** 5 days out of UHV.

If oxygen or possibly water vapor in the air is the leading factor to drive Ag film dewetting in a chemical process with oxide formation, a method to solve this problem is by depositing a capping material onto a freshly grown Ag film *in-situ* to protect the film from direct exposure to the atmosphere. Such "capping" materials developed in Shih Lab include magnesium oxide (MgO) and germanium (Ge). Recently I developed a new capping technique by depositing high-purity aluminum (Al) onto an Ag film followed by subsequent oxidation at room temperature in a high vacuum environment. The capping techniques will be discussed in detail in the next two sections.

Before concluding this section, one more question we are going to answer is: does strain in Ag film resulting from Ag-Si mismatch play a role in Ag film dewetting in the atmosphere? If it does, can a capping layer still be a promising method to solve the dewetting problem? Charlotte E. Sanders and coworkers speculated that the formation of pinholes at the initial stage of dewetting might be a strain relief mechanism. [57] Such considerations can be further corroborated by other researchers from the observation of flat tops of an Ag film with pits down to the wetting layer, for the formation of pits acts as a strain relief mechanism, as discussed in Chapter 1. [26] Although a complete profiling of the strain of Ag films on Si(111) is unknown, from the observation of smoothing of the Ag film at room temperature in UHV, we may cautiously assume that the strain in an Ag film might not play a significant role thermodynamically in driving a full-scale dewetting at room temperature, and hence a capping layer to cut the contact of atmospheric molecules with the Ag film shall be sufficient to arrest dewetting.

5.2 Techniques to Arrest Dewetting of Ag Films - Al_2O_3/MgO and Ge Capping

Although atomically smooth Ag films on Si(111) can be successfully achieved by different growth methods (see Chapter 4), the fast progression of dewetting of such films in the ambient environment seriously limits their applicability in other fields of research such as plasmonics. We cannot park the films indefinitely in UHV if we wish to expand the scope of study we can do with our superb atomically smooth films. Therefore, capping methods which can effectively stabilize the film in the ambient environment are sorely needed in a variety of studies, including the successful development of semiconductor nanolasers on the Ag platform. [48]

There are two important considerations for the capping material: (1) It shall easily wet the film surface and hence form a complete overlayer (which is called "capping

layer" in this dissertation) on top of the film. The thickness of a capping layer at which it can fully cover the film shall be thin, no more than a few nanometers, in order not to affect the intrinsic properties of the underlying film. (2) It shall preserve the flatness of the film. The capping material shall not act as a driver to destabilize the film it is intended to protect from dewetting.

In this section I am going to present capping methods developed in the past by former members in the lab.

5.2.1 *Al_2O_3/MgO capping*

MgO is an appropriate material to cap Ag films for optics studies. Its transparency in the visible light regime lends merits to the application in plasmonics - it will not absorb visible light and therefore preserve the intrinsic optical properties of the underlying Ag film. [45]

To cap Ag film with MgO, we use an e-beam evaporator to deposit MgO on to a liquid N_2 cooled Ag film. The film is subsequently warmed up to room temperature after MgO deposition, similar to two-step growth. We keep the film at 90 K during deposition in order to prevent it from dewetting, which might be activated by the heating up of the film from continuous impinging of hot MgO molecules and heat radiation produced by the e-beam evaporator (Ag films will dewet at an elevated temperature, although we need to point out that dewetting might be less significant for a thicker Ag film. See Ref. [37, 57, 90]). Since all capping materials in my study are evaporated at high temperature (> 1000 °C), the two-step method is essential to grow the capping layer without damaging the Ag film.

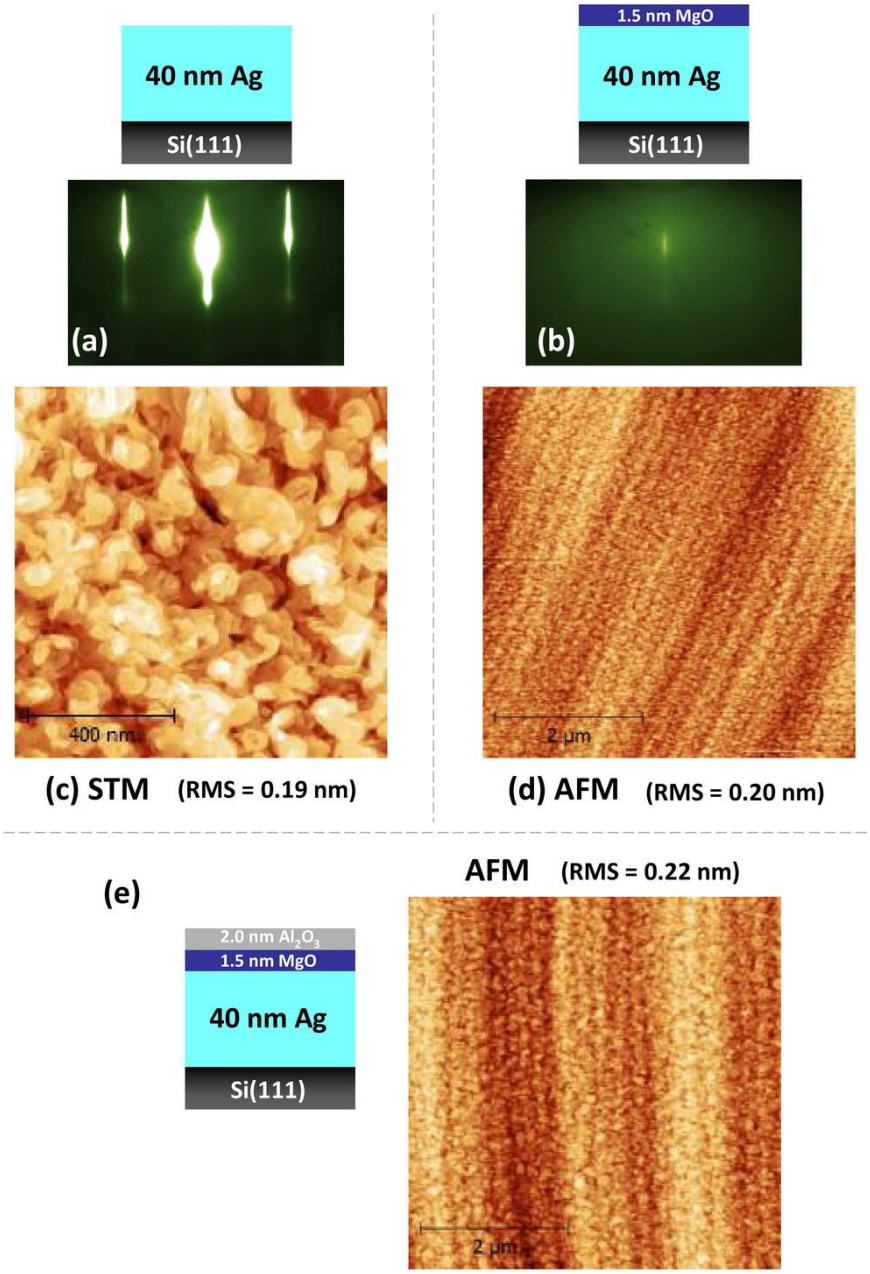

Figure 5.5 **(a)** RHEED on a 40 nm Ag film grown on Si(111). **(b)** RHEED after the film is capped by 1.5 nm MgO. The (111)-(1 × 1) pattern of the underlying Ag film does not disappear completely. **(c)** STM image of 40 nm Ag film. **(d)** AFM image taken *ex-situ* after the film is capped by 1.5 nm MgO. **(e)** AFM image acquired after the film is further capped by 2.0 nm Al_2O_3. The flatness of the film is maintained after Al_2O_3/MgO capping.

Fig. 5.5a and b are the RHHED pattern of a 40 nm Ag film before and after MgO capping. RHEED streaks of the Ag(111)-(1 × 1) structure can still be seen, though very faint, after 1.5 nm MgO capping. Possibly it is because the high energy electron beam can penetrate the thin MgO film and reach the underlying Ag surface. To compare the film morphology before and after MgO capping, we present together the STM image scanned on the Ag film before capping and the AFM image obtained after the film is capped by MgO (note that the AFM image is taken *ex-situ*), as shown in **Fig. 5.5c and d**, respectively. The room-mean-square (RMS) roughness of the Ag film, which can be determined from the STM image, is about 0.19 nm, and the RMS after MgO capping, extracted from the AFM image, is 0.20 nm. Both values are small and close to each other, confirming that the atomic smoothness of the film is preserved after MgO capping.

Unfortunately, MgO absorbs water vapor from the atmosphere and eventually induces the deterioration of the Ag film. In order to further protect the film, we deposit 2.0 nm Al_2O_3 onto the MgO-capped Ag film in a separate atomic layer deposition (ALD) furnace. The environment of ALD growth is harsh to the Ag film - the pressure in the chamber is at 10^{-9} Torr regime and the film temperature is raised to about 200 °C during deposition. Thanks to the protection by MgO capping layer, the film after Al_2O_3 growth does not roughen - it maintains the same flatness (RMS = 0.22 nm) as the one before ALD growth. See **Fig. 5.5e**. This "double" capping of Al_2O_3/MgO can satisfactorily protect the Ag film in the air for more than a year without the incurrence of dewetting while the atomic smoothness and the intrinsic optical properties of the Ag film are satisfactorily preserved. [45]

However, there are two problems in this capping method: (1) MgO is deposited by an e-beam evaporator, whose deposition rate is far more unstable than a K-cell-controlled source. The fluctuation in the deposition rate is usually so large that it is hardly to be con-

sidered reproducible. (2) As mentioned, MgO itself is not capable of protecting the Ag film from dewetting since it absorbs water vapor from the atmosphere. Even if the problem can be solved by the deposition of another capping material such as Al_2O_3, we still prefer a method only involving the deposition of a single material. It is why we later developed the Ge capping method, which will be reported in the next section.

5.2.2 *Ge capping*

To cap Ge, a Knudsen cell with a PBN crucible is used as the Ge evaporation source. The advantage of using K-cell is that it provides stable deposition with highly reproducible deposition rate. Therefore, the deposition thickness can be more precisely controlled than MgO. Ge will form a uniform and amorphous layer over the Ag film. The RHEED pattern of Ag(111) disappears - actually there is no pattern at all - after Ge deposition, confirming that the Ge film formed on top of Ag(111) is amorphous. See **Fig. 5.6a and b**. The flatness of the Ag film was satisfactorily preserved after Ge deposition, as manifested in the AFM image in **Fig. 5.6c**. The film quality can be maintained for over half a year. **Fig. 5.6d and e** show the evolution of the surface morphology of the Ag films with and without Ge capping after a few days in the air. Without Ge capping, a 20 ML Ag film on Si(111) will completely dewet after 9 days in the air, while a Ge-capped film maintains the atomic flatness more than a month. Unfortunately it seems that Ge-capped films will eventually degrade after about a year in the atmosphere. Not only the durability of Ge capping is questionable (though good enough for most *ex-situ* studies), but there are also other problems which might seriously restrict the applicability of a Ge-capped film. First, for optics applications, Ge is not an ideal material because it is a narrow-bandgap semiconductor (0.67 eV) which may cause undesired absorption in the visible wavelength regime. [86] Light propagating in a structure incorporating Ge might be

attenuated due to the absorption by Ge. Secondly, Ge is a "soft" material and can be easily dissolved in an organic solvent such as acetone. This proposes a difficulty to device fabrication since most device fabrication protocols involve a variety of organic solvents. As a result, a number of studies involving device fabrication such as transport measurement cannot be realized on a Ge-capped film.

5.3 New Capping Method - Aluminum Oxide (AlO_x) Capping

Although Ge can successfully cap our atomically smooth Ag and Pb films, it also presents its limits in fully realizing the studies in plasmonics and other fields. Therefore, it is imperative for us to develop new capping techniques to overcome these problems (visible light absorption and dissolution in organic solvents). An ideal choice will be aluminum oxide because:

(1) Aluminum oxide is a dense structure which might be quite robust to maintain the film quality in the atmosphere for longer time. By the same reasoning we expect that aluminum oxide be able to undergo device fabrication processes.
(2) Aluminum oxide is transparent to the optical range of the spectrum. The design of plasmonic structures involving aluminum oxide can better fulfill the desired enhancement of the plasmonic modes than a light-absorbing material such as Ge.

In brief, instead of Ge capping or the cumbersome Al_2O_3/MgO capping, we prefer a thin aluminum oxide, whose thickness can be precisely controlled, as the capping layer on a pristine Ag film.

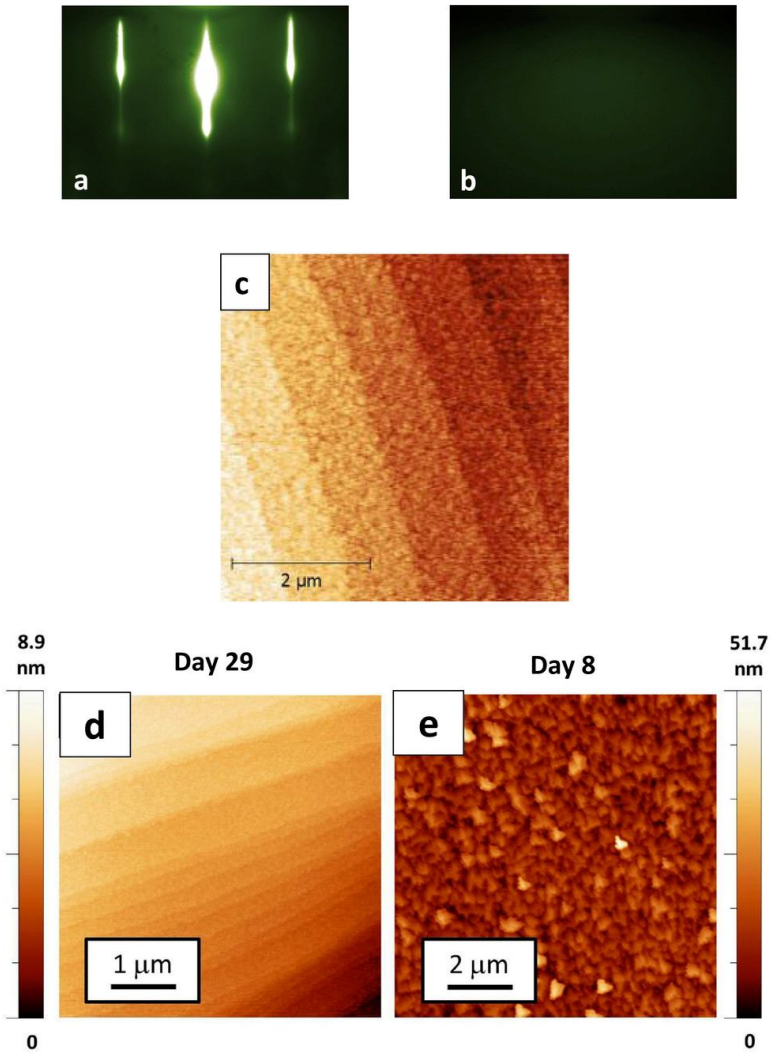

Figure 5.6 **(a)** RHEED on a 40 nm Ag film grown on Si(111). **(b)** RHEED after the film is capped by 3.0 nm Ge. The disappearance of RHEED pattern indicates that the amorphous Ge overlayer has fully covered the film. **(c)** AFM image of 40 nm Ag capped by 3.0 nm Ge, taken in the ambient environment. The RMS value is 0.19 nm. **(d)** and **(e)** are from [37]**. (d)** AFM image of a 20 ML Ag film capped by 2.0 nm Ge, taken after 29 days in the air. **(e)** AFM image of a 20 ML Ag film without any capping. The image was captured after 8 days in the air. The film was roughened towards irregular and tall clumps, which is considered to be completely dewetted.

We already mentioned the method of Al_2O_3 capping by ALD in the previous section, but two problems make it infeasible for our purpose: (1) Our facility does not allow us to transport the sample *in-situ* (*i.e.* without breaking UHV) from the MBE chamber to the ALD system. (2) As discussed, ALD growth is carried out in a hostile environment to the Ag film. A direct deposition of Al_2O_3 onto an unprotected Ag film will highly probably lead to a complete dewetting of the film.

Instead of a one-step, direct deposition of Al_2O_3, our new method consists of two steps: (1) Deposit high-purity Al from a K-cell onto Ag surface at 90 K in the MBE chamber, with a subsequent warm-up to room temperature. (2) Oxidize the Al film *in-situ* at room temperature in a strictly controlled flux of high-purity oxygen gas (exposing the sample to a partial pressure of oxygen at 10^{-6} Torr for 10 minutes). Here we only outline the procedure. See Chapter 6 for a detailed discussion of the design of this ultra-clean oxidation method.

Since the stoichiometry of such "naturally oxidized" aluminum is not really determined (more discussion will be presented in Chapter 6) [58, 60, 96, 97] I will simply denote the structure as AlO_x in this dissertation.

Our method allows the growth of the Al capping layer in a superbly clean UHV environment and by growing the Al overlayer at 90 K with subsequent warm-up to RT we assure the delicate, metastable Ag film against dewetting during the growth. The strictly controlled flow of high-purity oxygen gas in UHV allows the formation of a pure, densified native oxide layer with a uniform thickness. Overall, the AlO_x capping method we propose here can successfully overcome all problems related to the ALD growth.

Bulk Ag and Al share a common FCC structure, and the lattice mismatch is less than 1 % (lattice constant of Ag(111) is 0.409 nm and lattice constant of Al(111) is 0.405 nm). Therefore an additional advantage of deposition of Al, instead of Al_2O_3, on Ag is

that this approximately lattice-match system might lead to a desired layer-by-layer growth of Al on top of Ag. Unfortunately, the influence of interfacial strain between Al and Ag, despite the tiny mismatch between them, might complicate the growth mode. [98] Another issue of Al on Ag (or vise versa) is that the interface between Al and Ag might not be clear-cut - possibly there exists Al-Ag interfacial alloy even if Al and Ag have almost no miscibility at room temperature (and lower temperatures). [99]

Due to these complications, one important question we immediately face before achieving a well-functioning capping layer is: How much coverage of Al will be necessary to completely cover the Ag surface? Assuming that the growth of Al on Ag might follow the layer-by-layer fashion at the very early stage of growth, we first attempted to deposit only 1 ML Al onto an Ag film and studied whether this thin coverage will form a complete overlayer on the Ag surface. The results are discussed below.

5.3.1 *Oxidized 1 ML Al - 20 ML Ag - Si(111)*

To test the feasibility of aluminum oxide capping, we deposited 1 ML Al onto a 20 ML Ag film by the two-step method (deposition at 90 K with a subsequent warm-up to room temperature). After growth, the surface morphology and electronic properties of the sample were studied by STM.

Fig. 5.7a shows the RHEED pattern taken *in-situ* on the 20 ML Ag and **Fig. 5.7b** is the RHEED taken on the same film after it is capped by 1 ML Al. The (111)-(1 × 1) pattern is preserved after Al deposition, which is expected considering the (nearly) lattice matching between Al and Ag. **Fig. 5.7c and d** show STM images of the Ag film before and after Al capping, respectively. After Al capping, the surface maintains the atomic flatness of the original Ag film. However, a critical question arises: Does a 1 ML Al completely cover the underlying Ag? To clarify this question, we consider two cases regard-

ing the structure of a pit on a terrace as shown in **Fig. 5.8a and b**. **Fig. 5.8a** shows the case in which a pit is simply a place where there is no coverage of Al, and the underlying Ag is thus exposed. In **Fig. 5.8b**, a pit is a structure where the Al overlayer follows the morphology of the underlying Ag film. Therefore, if a pit happens to have a structure in **Fig. 5.8a** it means that 1 ML Al fails to completely cover the Ag film, and higher coverage shall be applied to form a complete overlayer to truly "cap" the underlying Ag film.

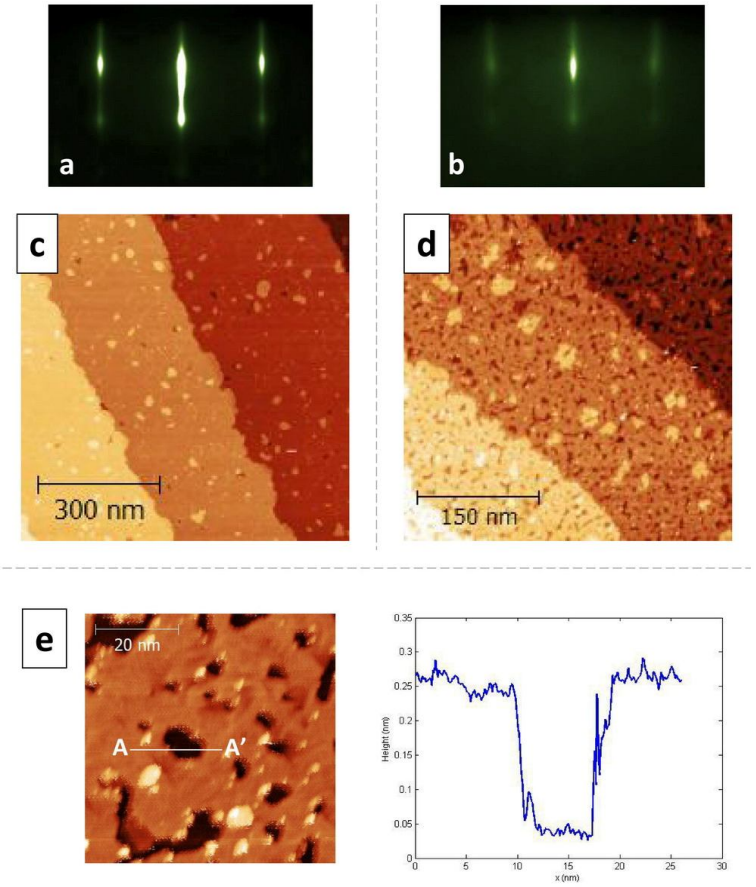

Figure 5.7 RHEED **(a)** and STM **(c)** of a 20 ML Ag grown on Si(111) by the two-step method. RHEED **(b)** and STM **(d)** of the same film after being capped by 1 ML Al. **(e)** Line profile along AA' across a pit on the terrace. The depth of the pit is about 2.3 Å.

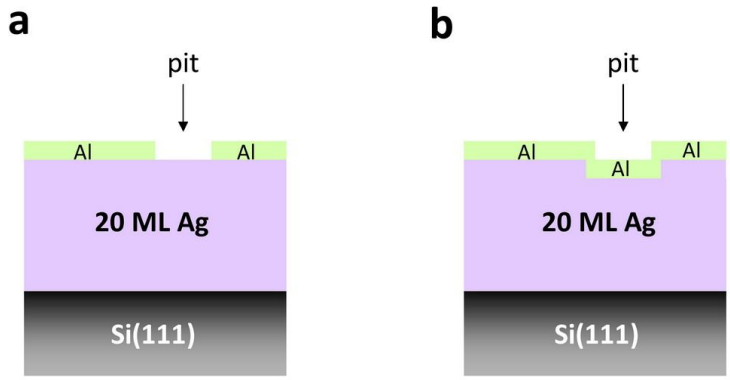

Figure 5.8 Two scenarios about the structure of a pit on the terrace of a 1 ML Al capped Ag film. **(a)** A pit is where there is no coverage of Al. The underlying Ag is exposed in this case. **(b)** A pit which simply follows the underlying morphology of the Ag film.

To determine which scenario a pit structure follows, we cannot simply measure the depth of a pit since the thickness of a single layer of Al(111) (2.34 Å) is very close to Ag(111) (2.36 Å). As shown in **Fig. 5.7e**, the depth of a pit measured from the STM image is about 2.3 Å, which is not possible to help us determine whether it is the thickness of a monolayer Ag or a monolayer Al. Instead, we need to carry out the scanning tunneling spectroscopy (STS) on a pit and on the terrace surrounding the pit to elucidate the situation.

See **Fig. 5.9**. We observe a surface state at about 0.16 eV from the dI/dV spectrum (light blue curve) taken on the pit (position 1). In contrast, no such a surface state is found on the dI/dV curve (green one) taken on the terrace (position 2). For comparison, we also draw dI/dV curves taken on an atomically smooth 20 ML Ag film (purple curve) and 6 ML Al film (black curve), respectively, in the same plot. Both films are grown by the two-step method on Si(111). The spectrum on 20 ML Ag also shows the surface state at about 0.16 eV, which is a Schockley-type surface state arising from the shift of the

s-p-band edge L_2' induced by the strain in the Ag film due to the lattice mismatch between Ag and Si. [68, 100] However, no surface state at 0.16 eV can be observed on the 6 ML Al film. The observation of the persistent surface state on the pit (position 1) of the Al capped Ag film, which is consistent with the one found on the 20 ML Ag film, indicates that the pit is a place where the underlying Ag is exposed. In contrast, the observation that there is no surface state on the terrace (position 2) suggests that the surface state of Ag is possibly overshadowed by the Al overlayer. In brief, from the analysis of the dI/dV spectra we conclude that 1 ML Al fails to completely cover the underlying Ag film. The pit is a structure not covered by Al, as shown in **Fig. 5.8a**, in which the underlying Ag is exposed.

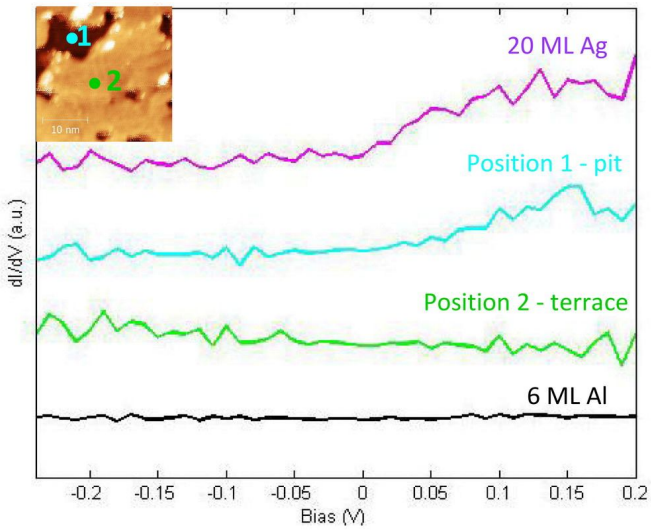

Figure 5.9 dI/dV spectra on Position 1 (light blue) and Position 2 (green) of the Al capped Ag film. The inset is the STM image indicating the positions where the dI/dV data are taken. For comparison, dI/dV spectra on a two-step-grown, atomically smooth 20 ML Ag film (purple) and 6 ML Al film (black) are shown in the same plot.

To complete the study, I oxidized the sample *in-situ* and then removed it out of UHV. The AFM image in **Fig. 5.10a** shows a very flat morphology when the sample was just removed from UHV. However, in **Fig 5.10b**, the AFM image, taken after only two days in the ambient environment, shows clumps with height ranging from 3 nm to 10 nm everywhere on the surface, indicating an ongoing dewetting process. Combined with the observation of our earlier study of STM/S, we conclude that these clumps originate from the pits which expose the underlying Ag film.

The STM measurement was carried out by my colleague Dr. Chendong Zhang. I express my gratitude to his effort.

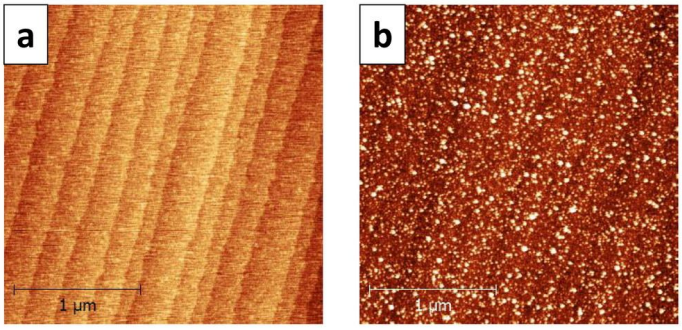

Figure 5.10 **(a)** AFM image of 20 ML Ag capped by oxidized 1 ML Al, taken immediately after the sample was removed from UHV. **(b)** AFM image of the sample after staying in the air for 3 days, The omnipresent clumps dotting the whole surface signify a dewetting process in progress.

5.3.2 *Oxidized 5 ML Al - 20 ML Ag - Si(111)*

The lesson we learned from the previous study is that 1 ML Al cannot fully cover the Ag film and thus fails to stabilize the film. To solve this problem we need to increase Al coverage, but it poses a dilemma - if the Al overlayer is thick, it will not be fully oxidized, as we are going to explain below. An incompletely oxidized Al capping film will

be completely useless in the perspective of a plamonic device operated in the optical range of the spectrum since un-oxidized, pure Al will make tremendous loss to that regime (see Chapter 2).

The main limitation to our AlO_x capping is that, we cannot control the thickness of the oxide film in our oxidation setup. The oxidation of Al is a self-limiting process in which only the topmost layers of Al will be oxidized and the oxidation process will stop once the oxide film reaches its terminal thickness, which depends on oxidation conditions such as Al temperature during oxidation, the partial pressure of oxygen and the exposure time to the oxygen gas. See Chapter 6 for a detailed review of studies related to Al oxidation. For our current purpose we need to point out that the terminal thickness of the oxide film by our oxidation method might be probably close to the thickness of native oxide formed on the surface of bulk Al(111) in the ambient environment, which is estimated to be from 14 Å to 30 Å. [101, 102]

To reconcile the necessity of increasing Al coverage with the dilemma posed by a self-limiting oxidation process, we proposed a coverage of 5 ML Al as a reasonable attempt - which might be thick enough to fully cover the underlying Ag surface while can still be (almost) fully oxidized.

Taking on the issue of Al coverage thick enough to fully cover the underlying Ag film, we noted a previous study conducted by V. Fournée *et al.* [98] about the growth of Ag on Al(111). In that study the authors showed that the deposition of 2 ML Ag on Al resulted in a rough surface with multi-layer islands, while when the deposition increased to 5 ML of Ag the surface showed a very smooth morphology - indicating the growth has switched to the layer-by-layer fashion. In other words, layer-by-layer growth can be activated by just a bit higher deposition. Even if our study was the reverse case (Al on Ag, rather than Ag on Al), and even if we did not observe the rough growth when the deposi-

tion was only 1 ML Al (see the discussion in the previous section), the study from V. Fournée *et al.* still gave us clues that a deposition of 5 ML Al might be a good guess leading to a desired layer-by-layer growth of Al which completely covers the Ag surface.

For the consideration of self-terminated oxidation, first we note that 5 ML Al is about 12 Å. Assuming that the Al overlayer can be oxidized until the self-limiting thickness is reached (about 20 Å in the atmosphere), and also assuming that the thickness of each monolayer of Al after oxidation will not deviate too much from that of the crystalline Al_2O_3 (about 2 Å of a monolayer), we speculated that 5 ML deposition might be probable to allow a full oxidation. Since Al oxidation is a complicated process involving electron transfer and the build-up of the so-called Mott potential, and since our situation, which includes the underlying Ag film, is more complicated than most studies based on bulk Al oxidation (I will present a detailed discussion of Al oxidation in Chapter 6), the reasoning simply based on the terminal oxide thickness is pretty naive, but without a further support on theory and experimental results, it is a reasonable guess for us to design the experiment to test the idea.

To test the idea of 5 ML Al capping, we conducted a similar experiment as the previous one. Here, instead of depositing 1 ML Al onto the Ag surface, we deposited 5 ML Al on a 20 ML Ag film. **Fig. 5.11a and b** show the RHEED patterns taken *in-situ* on a 20 ML Ag before and after 5 ML Al capping, respectively. The (111)-(1 × 1) crystal structure is preserved. To save time, we did not carry out STM study in this experiment. Instead, we directly oxidized the sample after Al deposition and then removed it out of UHV. The surface morphology was thereafter examined by AFM. **Fig. 5.11c** shows the AFM image of the sample just removed from UHV (RMS = 0.15 nm). **Fig. 5.11d** is the AFM image of the sample after it was stored in the atmosphere for 110 days. The RMS value is about 0.23 nm. Both images show atomic smoothness with small RMS roughness,

suggesting excellent stability of the Ag film in the ambient environment because of the protection of a thin AlO_x capping layer.

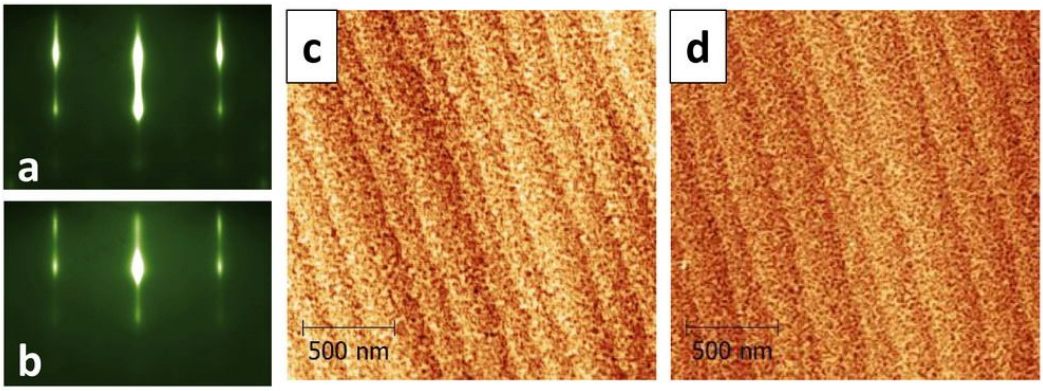

Figure 5.11 **(a)** RHEED on 20 ML Ag grown on Si(111). **(b)** RHEED after the film is capped by 5 ML Al. The (111)-(1 × 1) structure is preserved. **(c)** AFM image of 20 ML Ag capped by oxidized 5 ML Al, taken in the ambient environment immediately after the film was removed from UHV. RMS roughness of the film: 0.15 nm. **(d)** AFM image of the sample after stored in the atmosphere for 110 days. RMS roughness: 0.23 nm.

5.3.3 *Thicker (25 nm) Ag Film Capped by AlO_x*

The purpose of the development of AlO_x capping is to facilitate research in the field of plasmonics. From the previous study we show that a 5 ML Al overlayer oxidized *in-situ* can readily stabilize the underlying Ag film. To completely realize the applicability of this new capping technique, we prepared a thick Ag film (25 nm) intended for plasmonic studies, followed by 5 ML Al capping and subsequent *in-situ* oxidation. **Fig. 5.12a, b and c** show RHEED on the 25 nm Ag film, the same film with 5 ML Al capping, and the resultant AlO_x-capped film after *in-situ* oxidation, respectively. The underlying (111)-(1 × 1) pattern can still be observed after oxidation though remarkably weakened, which indicates that: (1) The newly formed oxide film is amorphous, and (2) the high en-

ergy electron beam can penetrate this thin oxide film to reflect the structure either of the non-oxidized Al or the underlying Ag surface.

Fig. 5.12d shows the AFM image of the AlO_x-capped film. The RMS roughness of the film is small (0.30 nm). Moreover, we observe in the AFM image the steps on the surface which follow the underlying Si substrate, suggesting the atomic smoothness of the film. Because of the atomic smoothness of the film, we believe that the AlO_x capping layer is very uniform (the uniformity of the oxide prepared by our growth and oxidation method is further corroborated by the superconductivity study carried out by Dr. Philip Adams' group in Louisiana State University). This uniform oxide capping layer can thus readily serve as an excellent dielectric spacer in the design of MIS plasmonic structure (see Chapter 2). However, since we cannot control the thickness of the native oxide layer, we have no way to tune the thickness of the dielectric spacer by this *in-situ* oxidation method. The problem can be easily solved by simply further capping the film with Al_2O_3 using the ALD method. Similar to Al_2O_3/MgO capping, the Ag film, already protected by AlO_x, can survive the hostile environment during ALD growth. **Fig. 5.12e** shows the AFM image of the same Ag film (already capped by AlO_x) after it was further capped by 2.0 nm Al_2O_3. The flatness of the film was perfectly preserved (RMS value is 0.33 nm).

As mentioned, Ge cannot resist against most organic solvents so it is not an appropriate material for device fabrication. In contrast, we confirmed that a thin AlO_x layer can perfectly sustain itself without being dissolved in a sonication bath in acetone, proving its sturdiness as an ideal material fully compatible with device fabrication. The fabrication of devices carried out on AlO_x-capped films is beyond the scope of this dissertation so I am not going to report the relevant data here.

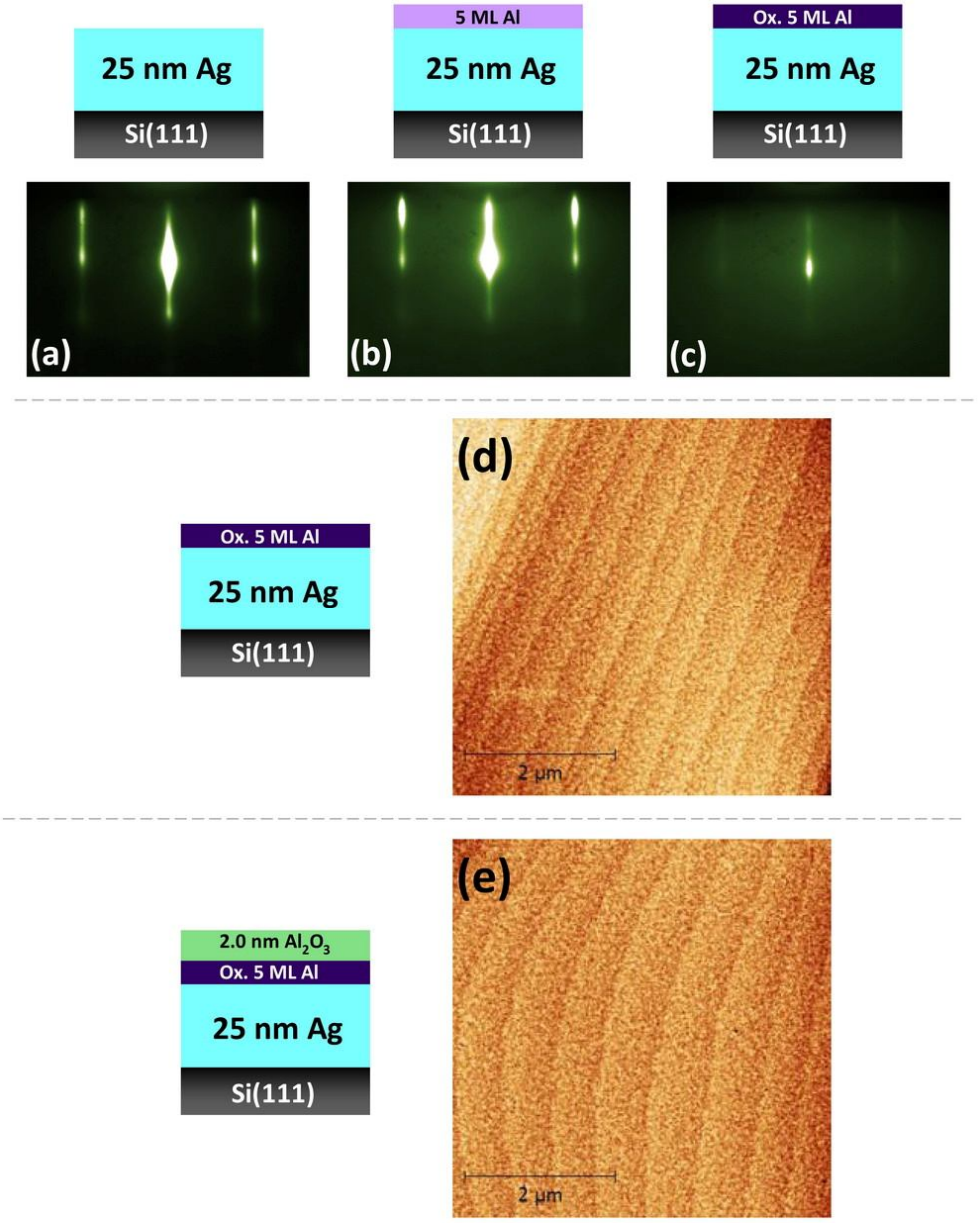

Figure 5.12 RHEED on **(a)** 25 nm Ag, **(b)** the same film from **(a)** with 5 ML Al capping, and **(c)** after *in-situ* oxidation. In **(c)**, the (111)-(1 × 1) pattern can still be seen, though much weakened. **(d)** AFM image of the AlO_x-capped Ag film. RMS roughness: 0.30 nm. **(e)** AFM image of the same film after it is further capped by 2.0 nm Al_2O_3 using ALD growth. RMS roughness: 0.33 nm.

Before concluding this chapter, we left a question yet to answer: Is 5 ML Al completely oxidized? We cannot answer this question without conducting more experiments to study the composition of the oxide layer. However, we did observe a significant enhancement of photoluminescence (PL) on the MoS_2 flakes (a transition metal dichalcogenide, or TMD, material) which were transferred to the AlO_x-capped Ag film. Since the PL measurement of the TMD material is out of the scope of this dissertation, I am not going to discuss the relevant study here.

Chapter 6: Epitaxial Growth of Atomically Smooth Al on Si(111) and Its Intrinsic Optical Properties[†]

In Chapter 2 we emphasized the significance of Al as the next-generation plasmonic material in the ultraviolet (UV) regime. The importance of preparing a premium Al platform can only be more stressed due to the intensified research interest in UV plasmonic devices these days. In this Chapter I am going to report my work with coworkers in which we demonstrate that carefully fabricated Al films will have a much lower loss than the widely cited data from Palik's handbook. Moreover, the newly obtained data of Al intrinsic optic constants from our high-quality, atomically smooth Al films provide a more reliable source for theoretical prediction of Al plasmonic nano-devices.

Once a clean Al surface is exposed to the ambient environment, an oxide film covering the topmost few layers of Al will spontaneously develop with a self-limiting thickness. Ideally, we wish the oxide film to be highly densified and universally uniform to protect the underlying metal film from dewetting and contamination. A clean and uniform oxide overlayer can also serve as an excellent spacer in the MIS structure (see Chapter 2). Thus a well-controlled oxidation process will be very important in our study. It is also important in a wide range of technological applications including device fabrication [103, 104], heterogeneous catalysis [105] and the tunnel barrier in magnetic tunnel junctions. [106, 107] In this Chapter I am going to review earlier oxidation studies and, based on their findings, propose our own design of an optimally controlled oxidation method applicable to our purpose of growing a high-quality, universally uniform oxide

[†] Part of the work in this chapter was published. See Fei Cheng *et al*. "Epitaxial Growth of Atomically Smooth Aluminum on Silicon and its Intrinsic Optical Properties" *ACS Nano* **10**, 9852 (2016). In this work I prepared atomically flat Al films for the measurement of intrinsic optical constants of Al. I also studied film growth with varied deposition rates in this work and realized atomically smooth growth of epitaxial Al films with a high deposition rate.

film as an ideal capping layer and also as a dielectric spacer. Then I am going to report our systematic study of epitaxial growth of atomically smooth Al films and their extraordinary intrinsic optical properties.

6.1 Study of Oxidation of Aluminum - Background and Review

In this section I am going to review studies on Al oxidation and draw lessons from these earlier works for us to design the optimal procedure of oxidation tailored to our superbly high-quality metal films. One important subject in my study is to cap the Ag film with an Al oxide overlayer (see Chapter 5). Therefore I am going to review the work by H. Oughaddou *et al.* which is closely related to my research. [58]

H. Oughaddou *et al.* studied the growth and oxidation of 1 ML Al deposited on Ag(111) substrate. First they deposited 1 ML Al at room temperature (RT) onto a clean Ag(111) substrate using an effusion cell with a PBN crucible. The base pressure of the growth chamber is 2×10^{-10} Torr. The deposition rate is very slow - only 0.25 ML/min. After Al deposition, the sample was exposed to oxygen at 4×10^{-6} Torr for 13 minutes at RT. The surface was continuously monitored during oxidation by Augur electron spectroscopy. The evolution of the surface composition is shown in **Fig. 6.1**, in which a very quick drop of the intensity of Al peak at 68 eV was observed (the intensity drops to zero within 1 minute) while the intensity of oxygen peak at 509 eV increased simultaneously. This illustrates that a monolayer of Al can be oxidized very rapidly once exposed to the oxygen gas, even in a low partial pressure of oxygen such as 10^{-6} Torr.

In the same study the authors also found that the Auger intensity of the Al peak shifted from 68 eV to 57 eV after oxidation. The Augur peak of Al_2O_3 occurs at 54 eV, which is discrepant from the experimental observation. Therefore they conjectured that the composition of the oxide is unlikely to be Al_2O_3. Furthermore, in the evolution profile

during oxidation (**Fig. 6.1**) they observed a drastic drop of the Ag peak. They interpreted the observation as a consequence of a thin oxygen layer covering the surface. Therefore they proposed a model of the composition profile as O/Al/Ag, and the stoichiometry of the oxide is closer to AlO than Al_2O_3. From the attenuation of the Auger signal of Ag they determined that the thickness of a single layer of oxide is about 7.9 Å. Finally the authors found that the thin oxide layer is thermally stable: the sample was heated up to 500 °C in UHV and no major change in the Auger spectrum was observed.

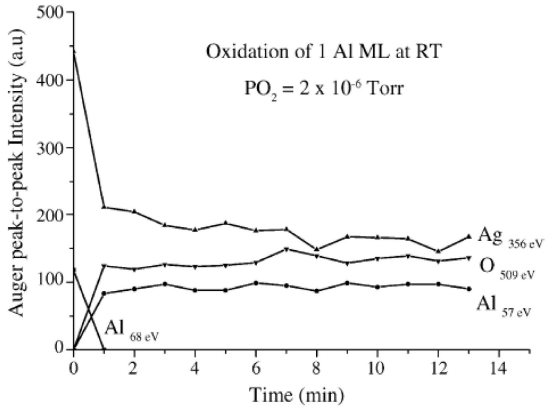

Figure 6.1 From [58]. Time dependence of the Auger peak-to-peak intensities during the oxidation process at RT.

Based on this study, the same group proposed a procedure of growing uniformly ultra-thin Al oxide layer on a metal (such as Ag) or semiconductor (such as Si) substrate: (1) Deposit 1ML Al at RT. (2) Oxidize the film at RT with at least 60 L of oxygen exposure. (3) Post-anneal the sample at 400 °C under UHV to reduce the surface roughness and make the oxide layer more uniform. In the subsequent studies they demonstrated the STM and cross-section TEM images to confirm the homogeneity of the oxide thickness. [59, 97] However, some concerns arise from their study:

(1) Without more study such as X-ray photoelectron spectroscopy on the profiling of the oxide composition it is still debatable to determine the stoichiometry of the oxide layer. In this dissertation I cautiously designate it as AlO_x.

(2) The authors indicated that the STM image of the surface after 1 ML deposition of Al on the Ag substrate showed an increase in roughness on the terraces and along step edges compared with the STM image of the bare Ag. Therefore I suspect whether one ML coverage of Al can really form a complete layer over Ag. In my study, I found that one ML deposition of Al on 20 ML Ag film cannot fully cover the underlying Ag - there are pits on the surface which expose Ag according to STM/S study (see Chapter 5 for the detail), although we need to point out that our growth condition is different from theirs (we grew the film by the two-step process while they deposited the film at RT).

(3) The authors found that the thickness of a monolayer oxide is about 7.9 Å , which is much thicker than one monolayer of crystalline Al_2O_3 (about 2 Å). Either the measurement is problematic (since they determined the thickness from the Auger signal attenuation, which is not a straightforward observation of the thickness and subject to large error) or the structure of the oxide formed by their method is very loose compared with the dense Al_2O_3.

(4) Although the authors conducted the experiment in UHV, but the pressure is not really good (2×10^{-10} Torr) considering the high reactivity of Al to oxygen. Therefore, very tiny oxidation might already occur before the sample was exposed to the oxygen gas. This sort of unintended oxidation might effect the accuracy of the measurement.

(5) Although the authors claimed that the oxide film is homogeneous in thickness, from their TEM image of oxide on Si [97] it seems not a very convincing statement.

If one monolayer Al cannot form a complete overlayer on top of an Ag film, we need to increase Al coverage further. However, the thickness of native oxide is self-limiting - the oxidation will stop once it hits the terminal thickness of the oxide. Thus we cannot grow a thick Al overlayer because it may not be completely oxidized. An understanding of the relationship between the terminal thickness and the oxidation condition is therefore imperative for us to design a workable oxidation method.

Before proceeding, we need to understand the fundamentals of the oxidation mechanism, in which the most cited theoretical model was proposed by Cabrera and Mott (CM model) more than half a century ago. [108] According to CM, Al oxidation starts with the dissociative chemisorption of O_2 from the gas phase via electron transfer from metal to the oxygen. During this process a variety of species of oxygen anions (O_2^{2-}, O_2^-, O^{2-}, O^-...) will form on the oxide surface while the counterpart Al cations will line along the oxide-metal interface. The negative oxygen anions and the positive Al cations thus generate an electric potential, called the Mott potential (V_M). Next, to grow more than the topmost oxide layer, either Al cations diffuse outwards to reach the surface and couple to the oxygen anions there or vice versa (oxygen anions diffuse inwards to meet Al cations). Such migrations of ions are mainly facilitated by the electric field established by the Mott potential. This leads to a high oxidation rate even at low temperature (such as room temperature). As the oxide film grows thicker, the rate of electron transfer across the oxide film (by tunneling or thermionic emission) decreases exponentially and fewer and fewer cations and anions can be created. Meanwhile, a thicker oxide film will diminish the capability of the Mott potential to lower the energy barriers for ions to diffuse through the oxide. Eventually these factors lead to the termination of the oxidation process.

Na Cai *et al.* carried out a systematic study on the oxidation of Al(111) surface at RT by tuning the partial pressure of oxygen, in which the oxidation was monitored by

X-ray photoelectron spectrometer. [60, 61] First the authors oxidized the clean Al(111) surface with a vey low partial pressure of oxygen, 1×10^{-8} Torr. The oxide film grows fast initially followed by a slowed regime when the film thickness approached a constant. Once no further increase of oxide thickness can be detected, the authors increased the partial pressure of oxygen. Each increase of oxygen partial pressure leads to a fast growth of the oxide film and a subsequent slow-down to a limiting thickness. A pattern of step-wise increase in the limiting thickness of the oxide film can be observed with the step-wise application of increased oxygen partial pressure, as shown in **Fig. 6.2**. Once the oxy-gen pressure reached about 1 Torr, the thickness of the oxide film remained essentially constant, irrespective of the prolonged exposure time or a further increase in oxygen pressure.

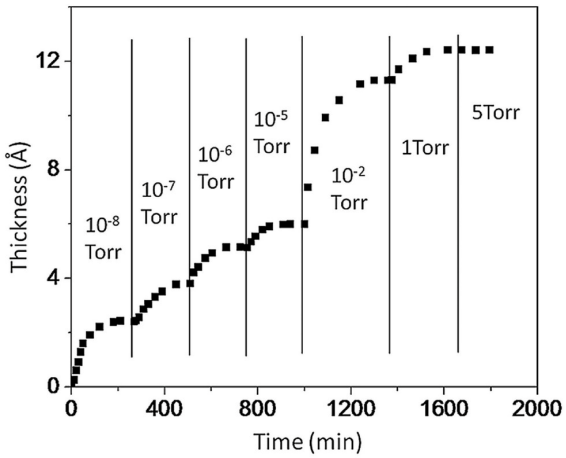

Figure 6.2 From [60]. Oxide film thickness as a function of oxidation time and oxygen gas pressure. The oxidation starts with a clean Al(111) surface which is oxi-dized first at $p(O_2) = 1 \times 10^{-8}$ Torr. The stepwise increase in oxygen pres-sure results in a corresponding increase of oxide thickness until the oxygen pressure reaches 1 Torr, beyond which the additional oxygen exposure of the surface will not lead to further oxide growth.

Instead of stepwise oxidation, the authors also carried out oxidation directly at different oxygen partial pressures. The results are shown in **Fig. 6.3**, in which they found that a similar oxide thickness can be achieved at a specific oxygen pressure no matter by the stepwise manner or by a direct application at that partial pressure. Therefore the authors suggested that the self-limiting growth of the oxide layer is predominantly determined by the oxygen pressure.

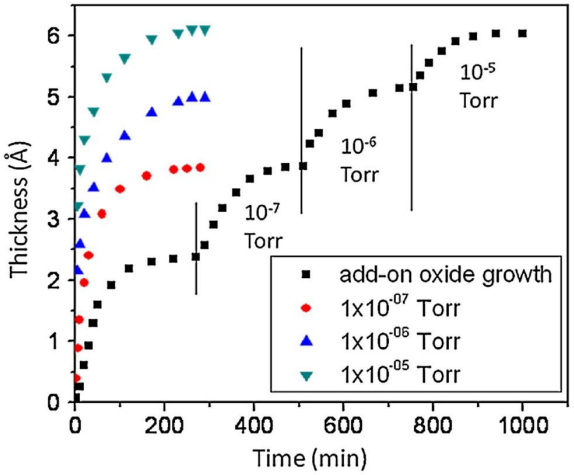

Figure 6.3 From [60]. Comparison of the oxidation process of Al(111) at varied oxygen partial pressures and the stepwise increase to different oxygen partial pressures. Both methods give a similar limiting oxide thickness at the same oxygen pressure.

In the CM model the Mott potential is determined by the metal-oxide work function Φ_m and the oxide-oxygen work function Φ_o,

$$V_M = \frac{\Phi_m - \Phi_o}{e},$$

where e is the elementary charge of electron. Since the work function is an intrinsic property, an assumption not explicitly stated in the CM model is that the Mott potential is

constant during the oxidation process. no matter what oxidation condition is incorporated. [108] But Na Cai *et al.* found from their study that the actual electrostatic potential created by the electronic species (oxygen anions and Al cations) can be much smaller than V_M at a low oxygen partial pressure. The electric potential reaches V_M only when the oxygen pressure is higher than 1 Torr.

In the same and subsequent studies they found that oxygen coverage on the oxide surface will increase with oxygen partial pressure. Eventually the maximal, saturated density of oxygen will be achieved for oxygen pressure at or beyond ~ 1 Torr. The authors conjectured that the saturation of oxygen coverage is key to the determination of the eventual self-terminating thickness of the native oxide layer. Beyond 1 Torr, the oxide thickness will not be increased further, but instead pinned at about 12.4 Å even under a higher oxygen pressure.

Oxygen adsorption seems to play an important role in determining the self-limiting thickness of native oxide. A theoretical study by Kakub D. Baran *et al.* [109] showed that oxygen adsorption energy is diminished as the oxide grows thicker, and the adsorption will be prohibited beyond a certain thickness, which is 18 Å determined by their calculation.

Na Cai *et al.* also determined the stoichiometry of the oxide film from their measurement, which is about $Al_{(2-x)}O_3$, $x \sim 0.24$ (a significant discrepancy from the result reported by H. Oughaddou *et al.*). [58, 60]

An important conclusion from the study by Na Cai *et al.* is that they implied the terminal thickness of Al native oxide will be about 12.4 Å, since the oxide will not become thicker beyond 1 Torr of oxygen partial pressure.

The measurement of the thickness of the oxide layer can be very tricky. In a study summarized by J. Evertssona *et al.* [102] the thickness of the native oxide on Al(111)

ranges from 20 Å to 30 Å, much thicker than that determined by Na Cai. *et al*. In 2015 L J Zeng *et al.* published a paper presenting a visually more straightforward measurement of the oxide thickness from the cross-section imaging of high-resolution transmission electron microscopy (TEM). [101] As shown in **Fig. 6.4** the oxide thickness can be precisely measured from the intensity profile of the cross section of the oxide film. The atomic resolution of the Al plane along the [111] direction can be clearly seen. The space between the atomic columns of the neighboring (111) plane was determined to be 2.4 Å according to the image (the same as the bulk value), confirming the accuracy of the measurement. The authors summarized the distribution of their measurements of the oxide thickness under different oxidation conditions in **Fig. 6.5**. Here they found a general tendency - the oxide will be thicker with higher oxygen partial pressure or longer exposure time. The data are summarized in **Table 6.1**. Finally, the study showed a relatively wild variation on the oxide thickness - the standard deviation can be as large as 3.7 Å.

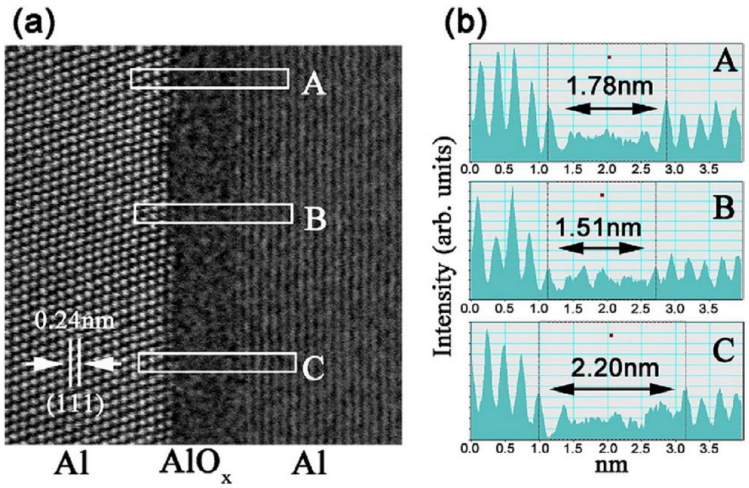

Figure 6.4 From [101]. **(a)** A high resolution scanning TEM image of the cross section of Al-oxide interface. Windows A, B, and C show the areas used to extract the intensity profile of the image. **(b)** Oxide thicknesses are measured from the intensity profiles derived from windows A, B, and C.

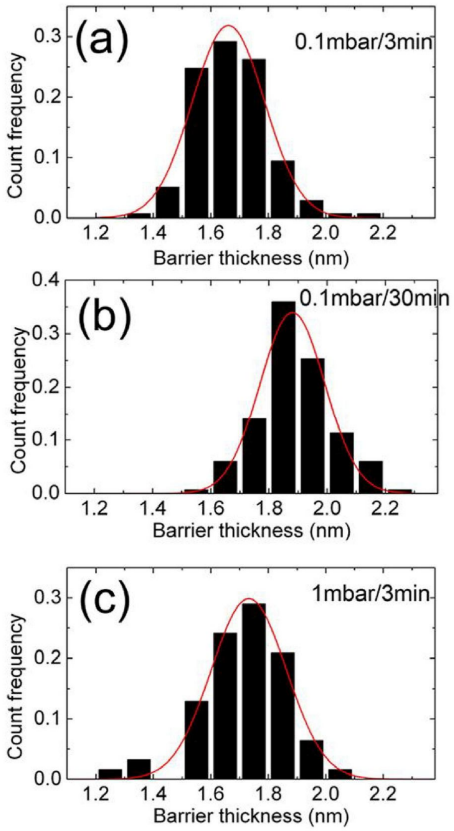

Figure 6.5 From [101]. Oxide thickness distribution measured from scanning TEM images of three samples oxidized at different conditions: **(a)** p_o/t_o ~ 0.1 mbar / 3 min, **(b)** p_o/t_o ~ 0.1 mbar / 30 min, **(c)** p_o/t_o ~ 1 mbar / 3 min. Experimental distribution is fitted with Gaussian functions, shown as the red curve superimposed on the experimental data.

Table 6.1 From [101]. Oxidation Parameters (oxygen partial pressure p_o and oxidation time t_o) and oxide thickness measurement (average oxide thickness $\langle l \rangle$ and standard deviation σ_l).

	p_o (mbar)	t_o (min)	$\langle l \rangle$ (nm)	σ_l (nm)
Sample 1	0.1	3	1.66	0.35
Sample 2	0.1	30	1.88	0.32
Sample 3	1	3	1.73	0.37

So far we only surveyed oxidation studies conducted at room temperature. We have not yet discussed the influence of temperature during oxidation. Temperature can significantly influence the behavior of oxidation and the resultant crystallinity of the oxide. L. P. H. Jeurgens *et al.* [96, 110] reported that the growth of the oxide layer will not be limited by a self-terminated thickness as the temperature during oxidation is higher than 573 K. An elevated temperature can essentially assist in electron transfer in the oxidation process by thermionic emission, and thus lifts the limit set by diminishing oxygen adsorption, which is believed to be the mechanism of self-limiting oxidation at low temperature. [60, 61, 109] Since we suspected that our metal films might dewet at elevated temperature, and also considered to simplify the experimental procedure, we only regarded carrying out oxidation at room temperature.

In summary, results of the study on Al oxidation from different groups showed discrepancies in several aspects, but some general characteristics can be drawn, as listed below:

(1) When oxidation is carried out at room temperature, the terminal thickness of the oxide layer depends on the oxygen partial pressure. However, higher oxygen pressure beyond 1 Torr will not lead to a thicker oxide layer.

(2) The rate of oxide growth is very rapid at the beginning of oxidation, followed by a slow-down when the oxide layer approaches the limiting thickness. It might take less than 1 minute to oxidize a monolayer of Al even in a low oxygen pressure such as 10^{-6} Torr.

(3) Oxidation at room temperature is a self-limiting process. If oxidation is carried out at elevated temperature (higher than ~ 600 K) the oxide will steadily grow without an apparent limiting thickness.

(4) The measurement of the thickness of the native oxide (i.e. oxide formed under the ambient environment) is tricky. The oxide layer may possess a significant unevenness with a large variation in thickness. Generally, the thickness ranges from about 14 Å to 30 Å.

(5) The stoichiometry of the oxide is debatable. It is highly unlikely to be Al_2O_3, but the true stoichiometry is yet to be determined.

(6) The oxide is amorphous. It is also uncertain whether the density of the oxide is similar to crystalline Al_2O_3 or much looser. One group found out the thickness of a monolayer of oxide to be 8 Å from their measurement [58] but it was not supported by other groups and the value is very questionable because it showed a large discrepancy from the thickness of a monolayer Al_2O_3 (about 2 Å). It is also difficult to determine a monolayer in an amorphous structure. Generally it is believed that the density of the amorphous oxide is close to the crystalline Al_2O_3 though it is yet to be clarified with more experimental data. [109, 111]

To design an appropriate oxidation procedure, we carefully considered the following factors: (the "sample" mentioned in the following descriptions can be either an Al film on a Si substrate or an Ag film capped by an Al overlayer)

(1) The oxidation should be carried out in a very clean environment, *i.e.* an UHV system to make sure that the oxide film is grown with least contamination. To fulfill this requirement we conduct the experiment in a loadlock equipped with a turbo-molecular pump to maintain the base pressure in about 8×10^{-9} Torr. The setup is shown in **Fig. 6.6**.

(2) To simplify the procedure, we oxidize the sample at room temperature. Therefore the oxidation is self-limiting.

(3) During oxidation, the leak valve is carefully opened to control the flux of high-purity oxygen gas to about 1.6×10^{-6} Torr. Since the turbo-molecular pump is kept running during oxidation, one important reason to keep the oxygen flux at such a low level is to protect the turbo-molecular pump from being overburdened. (See **Fig. 6.6**)

(4) Since the rate of oxidation is very fast before approaching a limiting thickness (**Fig. 6.3**) we only oxidize the sample for 10 minutes even in a low oxygen partial pressure of ~ 1.6×10^{-6} Torr (~ 960 L of overall exposure). According the study by Na Cai *et al.* (**Fig. 6.3**), the oxide thickness will reach about 3 Å in our oxidation condition. We believe that by our carefully administered oxidation procedure, the topmost layer of Al will be oxidized with the formation of a densified and clean oxide layer.

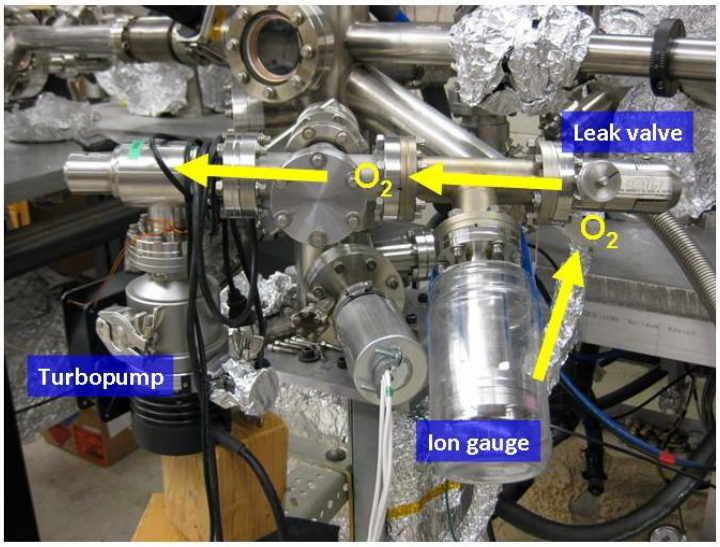

Figure 6.6 Oxidation Setup. The oxidation process is carried out in the loadlock. The setup is equipped with a leak valve and turbo-molecular pump to control the flux of oxygen gas. Yellow arrows indicate the flowing direction of the oxygen gas.

Since the limiting thickness of the native oxide is about 20 Å , we speculate that the sample will be further oxidized after removed from UHV. Since the sample is already protected by the topmost densified film of oxide, the subsequent oxidation in the atmosphere should be proceeded uniformly over the surface without contaminating the sample until the self-limiting thickness is reached.

The uniformity of the oxide layer is a critical issue in the study. From our literature survey it seems that no group can really achieve the growth of atomically uniform oxide layers. Possibly the main source to cause the variation in oxide thickness comes from surface defects and grain boundaries arising from polycrystalline Al. They will give rise to different surface energies, which might lead to the variation in the "penetration capability" of the oxide.

Our growth method can assure the atomic smoothness and single-crystallinity of the film, thus easily overcoming the problem. To demonstrate our *in-situ* oxidation procedure ("*in-situ*" means that the vacuum is not broken during the process), we oxidized a 10 ML Al which was grown on a Si(111) substrate by the two-step method. As shown in **Fig. 6.7**, after *in-situ* oxidation, the Al(111)-(1 × 1) RHEED pattern is much weaker, suggesting the formation of a thin oxide layer. The sample was subsequently removed from UHV and the surface morphology was monitored by AFM. We did not observe any feature of dewetting after the sample was stored in the atmosphere for 20 days (**Fig. 6.7d**), implying that the native oxide layer can well protect and stabilize the underlying Al film. This feature makes Al even more appealing as a plasmonic material since there is no need to cap the film with an additional material and the surface of the film can be quickly passivated by oxidation after nano-structure patterning.

We cannot fully exclude the possibility that the 10 ML Al film was eventually fully oxidized in the atmosphere, but since we successfully detected the superconductiv-

ity of the 10 ML film in another study with Dr. Philip Adams at the Louisiana State University, it is more likely that a very thin and uniform Al film exists between the substrate and the oxide, which in turn implies that the oxide formed on top of the Al film is indeed very uniform. Since the superconductivity study is beyond the scope of the dissertation, I do not report the relevant results here.

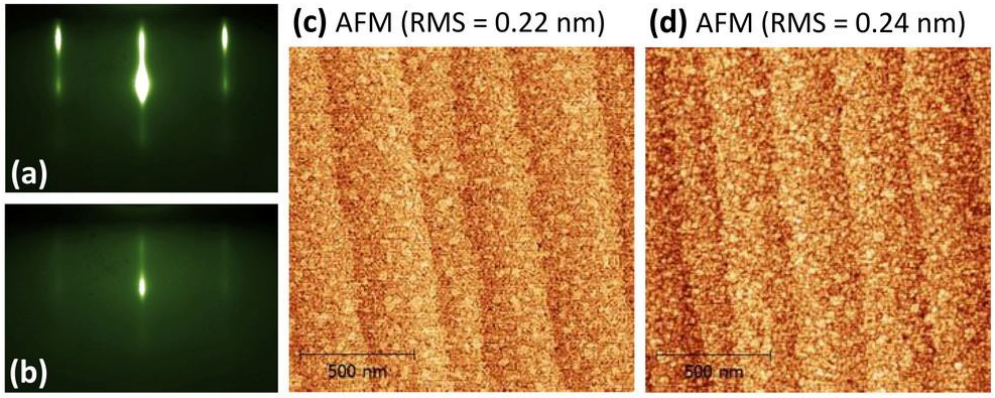

Figure 6.7 Oxidation of a two-step-grown 10 ML Al film on Si(111). **(a)** RHEED of the 10 ML Al. **(b)** RHEED after the film was oxidized. During oxidation the film was exposed to about 960 L oxygen. **(c)** AFM of the film taken *ex-situ*, after *in-situ* oxidation. **(d)** AFM of the film after it was stored in the atmosphere for 20 days.

It is difficult to determine the amount of Al deposition which can completely cap an Ag film. In Chapter 5 we reported that 1 ML Al failed to completely cover the Ag surface, while a thicker Al overlayer may not be completely oxidized by our oxidation method. Assuming that an Al overlayer can be oxidized until the self-limiting thickness is reached (about 20 Å in the atmosphere), and also assuming that the thickness of each monolayer of Al after oxidation will not significantly differ from that of the crystalline Al_2O_3, we speculated that 5 ML Al deposition will be thick enough to completely cap the

Ag surface while still essentially thin to allow a full oxidation. The relevant results are discussed in Chapter 5. However, we cannot exclude the possibility that a trace of pure Al may exist in the capping layer after oxidation. We do need to conduct more research in the future to reveal a complete picture of the profiling of the structure and composition of the oxide capping layer.

One caveat we need to give here when we try to make any prediction of our oxidation process from theory and experimental results we surveyed in this section is that our system is much more complicated than the oxidation of bulk Al. Since our system is a thin film deposited on a Si substrate or on a thin Ag film, several considerations arise:

(1) Possibly the oxidation behavior of a thin Al film will deviate from that of bulk Al, since a thin film cannot supply indefinite Al atoms for oxidation and since in the thin film regime, the influence of quantum size effect will be significant. These factors are not considered in the bulk Al study.
(2) Possibly the underlying Si substrate or Ag film will influence the behavior of Al oxidation via charge spilling or other channels of charge transfer mechanism.
(3) Possibly the atomic smoothness of our film will make our study a better comparison with most theories in this field which ignore effects of surface defects and grain boundaries to simplify the model.

It is very tricky to draw parallel conclusions from the bulk Al study to our thin film system, and the uniformity of the oxide layer, which is not really realized in most studies, is yet to be confirmed in our system, so more research considering the profiling of the composition of the oxide layer on our samples is needed in order to better understand the oxidation mechanism of thin Al films.

6.2 Epitaxial Growth of Atomically Smooth Al on Si and its Intrinsic Optical Properties

Al is an excellent plasmonic material in the UV range (See Chapter 2 for the discussion). Recently Al plasmonics emerged as a highly pursued research field in the UV and short wavelength visible regime. [112 - 114] Furthermore, a UV plasmonic nanolaser by putting GaN nanowires on an Al platform has been successfully developed recently. [50] With the fast progress in the research field of Al plasmonics the demand for an excellent Al platform can only be higher.

In this section I am going to present our work of the development of epitaxial Al thin films on Si(111) as a plasmonic platform in the UV regime. First I will present the results of the film prepared by the two-step method, similar to the work done on Ag (see Chapter 4 for details). Since preparing a thick film for plasmonics by the two-step process is very time-consuming, I will present a more conventional method of growing the film at room temperature by a high deposition rate. Finally the optical properties revealed by the spectroscopic ellipsometry measurement of all epitaxial samples will be reported.

As already reviewed in Chapter 1, epitaxial growth of Al on GaAs has been achieved earlier. [29] However, epitaxial Al on Si, in addition to be an excellent plasmonic platform, is also compatible with the manufacturing of devices such as CMOS, [115] which makes the growth methods we developed even more appealing to the plasmonic community.

6.2.1 *Epitaxial Al by the Two-step Method*

The epitaxial growth of our Al films was carried out in the molecular beam epitaxy (MBE) system with a base pressure of 3×10^{-11} Torr (see Chapter 3 for experiment method). To prepare an atomically flat Al film, we deposited Al onto a clean Si(111)-(7×7) reconstructed surface at 90 K (see Chapter 3 for the preparation of Si(111) substrate)

with subsequent annealing to room temperature (RT). We deposited 25 ML Al in each deposition cycle until we reached the target thickness. For a 100 ML Al film we repeated the two-step procedure for 4 times. The deposition rate was slow (about 0.5 Å/min) and the chamber pressure during the deposition was no higher than 1.5×10^{-10} Torr.

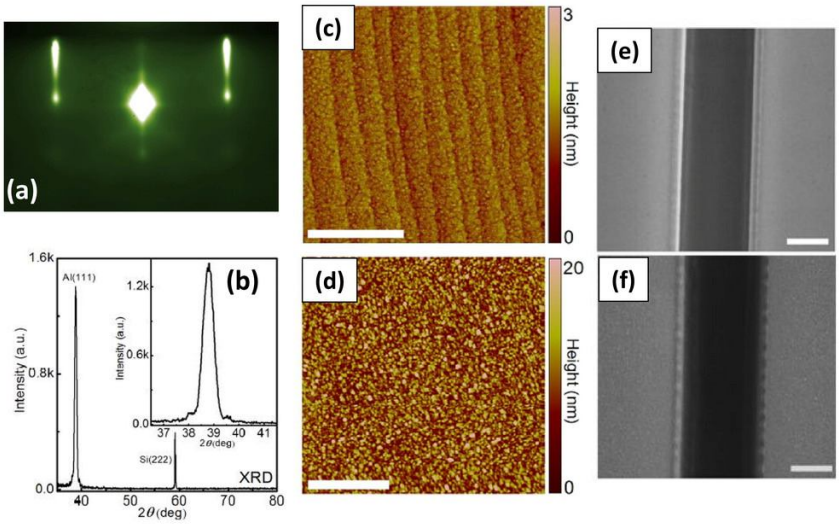

Figure 6.8 **(a)** RHEED pattern of a two-step-grown epitaxial 100 ML Al film. **(b)** XRD 2θ scan profile of the epitaxial Al film. The inset shows the enlarged Al(111) peak with a FWHM of about 0.5°. **(c)** *Ex-situ* AFM image of the epitaxial Al film (capped by about 2 nm oxide layer). RMS roughness: 0.23 nm. **(d)** AFM image of a thermally deposited polycrystalline Al film (24 nm). RMS roughness: 3.4 nm. **(e)** SEM image of the slot milled by FIB on the epitaxial Al film. **(f)** SEM image of the slot milled on the polycrystalline Al film. Scale bar on **(c)**, **(d)**, **(e)**, and **(f)**: 1 μm.

Fig. 6.8a showed the RHEED pattern taken *in-situ* on a two-step-grown 100 ML (23.5 nm) epitaxial film. The sharp, streaked pattern confirms single crystallinity of the film. Before removing the sample from UHV we carried out *in-situ* oxidation (see the previous section for details) by exposing the surface to the flux of high-purity oxygen at

1.6×10^{-6} Torr for 10 minutes. A thin, clean, and densified oxide layer will be formed on top of the Al film after oxidation. After *in-situ* oxidation, the sample was taken out of UHV and its surface was characterized by AFM in the ambient environment. The AFM image (**Fig. 6.8c**) clearly shows the stair-like structure which originates from the under-lying Si steps, confirming the uniformity and atomic smoothness of the epitaxial film by the two-step method. As a comparison, we prepared a sample of polycrystalline Al film with similar thickness (24 nm) by growing the film at RT with a high deposition rate of 2 nm/min using a conventional thermal evaporator (Denton Explorer) housed in a chamber with a base pressure of about 2×10^{-6} Torr. The RMS roughness of the polycrystalline sample, revealed by AFM, is about 3.4 nm (**Fig. 6.8d**) while the RMS of the epitaxial Al is 0.23 nm, an order smaller than the polycrystalline film.

To further investigate the crystallinity of this 100 ML epitaxial film, we carried out X-ray diffraction (XRD) analysis on the sample. As shown in **Fig. 6.8b** there is one sharp diffraction peak at 39° arising from the Al(111) crystal plane in the 2θ (30° - 80°) scan. Notably, the full-width at half maximum (FWHM) of the Al(111) peak is very small (about 0.5°), suggesting a good crystalline quality of the Al film. Since the Si(111) peak (occurring at 28.5°) is much stronger (about 3 orders higher in intensity due to a deep, several-micrometer sampling into bulk Si) than the Al(111) peak, we did not show it in order to highlight the feature of the Al(111) peak. Interestingly, we also observed a peak around 59° attributed to the Si(222) crystal plane. The observation of Si(222) is likely due to the atomic rearrangement of the topmost Si atoms on the Si(111)-(7 × 7) reconstructed surface induced by X-ray bombardment on the film.

We also investigated the performance of our carefully prepared epitaxial film a-gainst the thermally deposited film in terms of device processing such as plasmonic nano-patterning created by focused-ion-beam (FIB) milling. **Fig 6.8e and f** show the

representative scanning electron microscopy (SEM) images of slots sculpted by FIB into the epitaxial and polycrystalline films, respectively. Sharp, straight slot edges can be easily fabricated on the epitaxial film (**Fig. 6.8e**) while irregular shapes and minor structural defects are present along the slot edges on the polycrystalline film even in the optimal focused condition of the ion beam (**Fig. 6.8f**). The difficulty in creating a high-definition nano-structure on a polycrystalline film is due to the film's randomly oriented crystal grains and rough surfaces, which introduce variations in the resistance to the ion-beam milling process and thus result in ill-defined edges. This demonstration suggests that epitaxial films can better facilitate the fabrication of large-area, high-definition plasmonic nanostructures.

Thermal film deposition, XRD analysis, FIB milling, and SEM imaging were carried out by my colleague Dr. Fei Cheng.

6.2.2 *Epitaxial Al Grown by a Fast Deposition at Room Temperature*

The two-step method allows the fabrication of epitaxial films with superior quality of atomic smoothness and excellent crystallinity. However, the method is very time-consuming - it involves hours-long annealing processes and repeated cycles of growth. In this respect we need to explore a more conventional, room-temperature (RT) growth at a higher deposition rate, which is still conducted in a UHV environment and on an atomically-well-defined Si(111)-(7 × 7) substrate. This new method will eliminate the annealing process, and allow a one-shot growth, which will tremendously slash the time needed to prepare a film.

To develop this new method, we first studied the influence of the deposition rate on the surface morphology of the film. Here we designed a series of experiments in which we deposited 20 ML Al at RT onto a clean Si(111)-(7 × 7) substrate with varied

deposition rates - from 0.5 Å/min to 6.2 Å/min. AFM images shown in **Fig. 6.9a and b** represent the films deposited at 0.5 Å/min and 1.0 Å/min, respectively. The surface morphology of these two films are totally different from the two-step-grown, atomically flat one: the surface is rough, with flat-top islands separated by deep, meandering fissures. Interestingly, the morphology resembles those observed on Ag films prepared by a similar method (room temperature deposition with a low deposition rate). See Ref. [24].

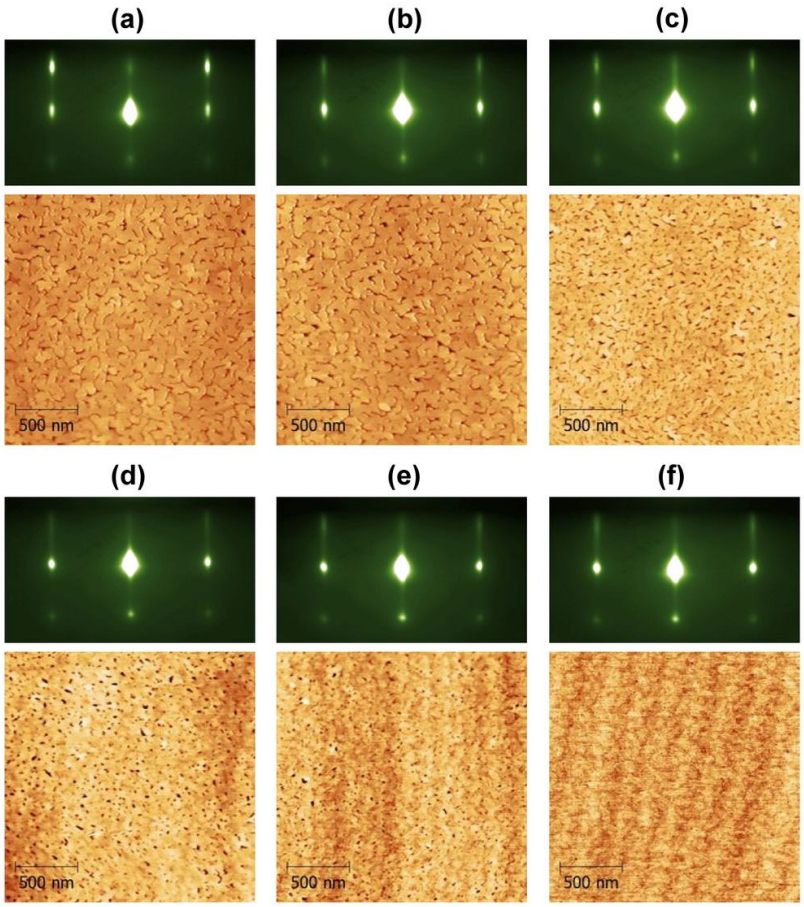

Figure 6.9 RHEED (top panel) and AFM (bottom panel) of 20 ML Al deposited on Si(111) at RT with different deposition rates: **(a)** 0.5 Å/min, **(b)** 1.0 Å/min, **(c)** 2.1 Å/min, **(d)** 3.1 Å/min, **(e)** 4.7 Å/min, and **(f)** 6.2 Å/min. RMS roughness of each film: **(a)** 0.84 nm. **(b)** 0.84 nm. **(c)** 0.39 nm. **(d)** 0.24 nm. **(e)** 0.17 nm. **(f)** 0.13 nm.

When the deposition rate increases to 2.1 Å/min, the film becomes flatter compared with those deposited at 0.5 Å/min and 1.0 Å/min, though the surface character of islands separated by grooves still retains (**Fig. 6.9c**). As the deposition rate is further jacked up, we find that the surface morphology is gradually improved: the RMS roughness of films decreases steadily with higher deposition rates. A sudden change in the surface morphology occurs when the deposition rate is raised to 3.1 Å/min - the surface is dotted with pinholes, rather than separated by deep grooves. (**Fig. 6.9d**). Eventually, when the deposition rate reaches 4.7 Å/min and 6.2 Å/min, the surface becomes very flat, with small RMS roughness which is comparable to the two-step-grown film, though tiny pinholes persist on these fast-deposited thin films (**Fig. 6.9e and f**).

Interestingly, RHEED patterns of all films in **Fig. 6.9a - f** are indistinguishable from the one taken on a film using two-step growth (see top panels in **Fig. 6.9**, RHEED on RT-grown films, and **Fig. 6.10a**, RHEED on two-step 20 ML Al). The observation of sharp diffraction patterns indicates that epitaxy is achieved in all growth conditions. RHEED is unable to inform us whether fissures or pinholes exist or not. There are two possibilities to explain the observation: (1) The size of fissures and pinholes is large compared with the coherent length of the electron beam; thus the electron beam can only discern the local crystallinity rather than the larger-area surface morphology. (2) The size of *domains* (*i.e.* the flat areas in the surface separated by grooves or discrete pinholes) is not too different on all samples (about 50 nm - 100 nm), resulting in similar size of streaks on all RHEED patterns. However, differences on the surface morphology can indeed give rise to different RHEED patterns. Take a closer look at RHEED patterns in **Fig. 6.9a and f**. The intensity on each streak of the RHEED pattern in **Fig. 6.9f** (taken on a relatively smooth film grown with the highest deposition rate in my study, 6.2 Å/min) is more uniform than in **Fig. 6.9a** (taken on a relatively rough sample grown by a low depo-

sition rate, 0.5 Å/min). This difference in RHEED patterns may arise from different surface morphologies. The film in **Fig. 6.9a** shows deep grooves (fissures) down to the wetting layer, which may cause deeper penetration of the electron beam into the film, leading to more three-dimensional scattering and hence more inhomogeneous intensity along the RHEED streak. In contrast, the flat film in **Fig. 6.9f** causes less penetration by the electron beam into the film and hence reduce the contribution of transmission electron diffraction, giving rise to RHEED streaks with more uniform intensity.

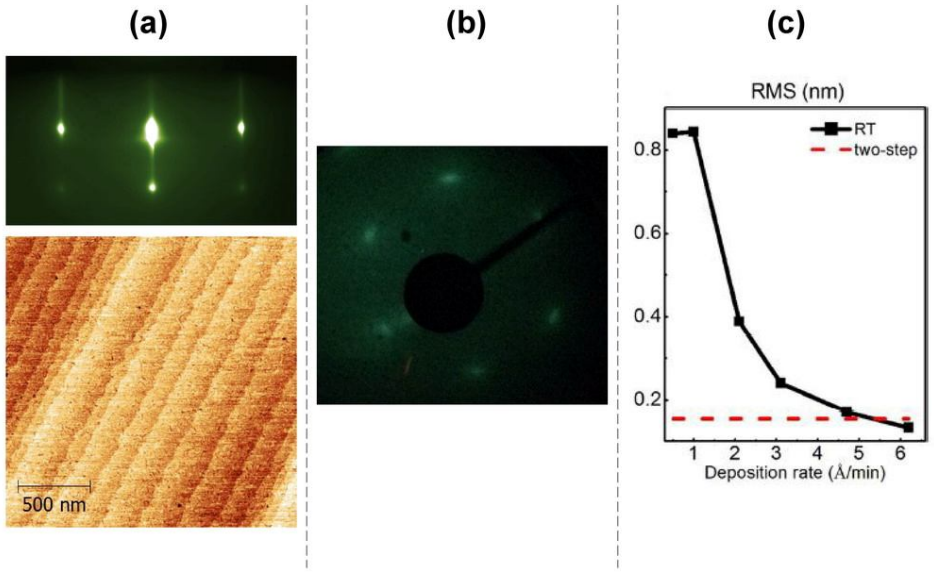

Figure 6.10 **(a)** RHEED (top panel) and AFM (bottom panel) of a two-step grown Al film (20 ML). RMS roughness of the film: 0.18 nm. **(b)** LEED of the film from **Fig. 6.9f**, 20 ML Al grown on Si(111) at room temperature with a deposition rate of 6.2 Å/min. The beam energy is 137 eV. The hexagonal LEED pattern corroborated the observation from RHEED that the film was grown epitaxially with (111)-(1 × 1) surface structure. **(c)** RMS roughness of films from **Fig 6.9a - f** extracted from the corresponding AFM image. The red dashed line represents the RMS of the two-step film in **(a)**.

Generally speaking, as long as epitaxy is maintained and local flatness is achieved, sharp streaks can be observed in RHEED. To further confirm the crystallinity of the 20 ML Al film deposited at RT by a deposition rate of 6.2 Å/min, we carry out LEED characterization on this film. Shown in **Fig. 6.10b**, the hexagonal LEED pattern suggests that the film is single-crystalline with the (111)-(1 × 1) hexagonal close packed structure (LEED was carried out by my colleague Qiang Zhang). An important lesson from this sequence of experiments is that we may possibly achieve the epitaxial growth of atomically smooth films at RT (the RMS roughness is comparable to the two-step-grown film. See **Fig. 6.10c**) without resorting to the elaborate two-step process as long as the deposition rate is high.

In order to further test whether the time-saving RT growth can be applied to grow thicker films for plasmonic applications, we deposited a film of 100 ML Al on Si(111)-(7 × 7) at RT with a high deposition rate (4.7 Å/min). To test the idea of combining the advantages of the two-step method and RT growth, we also prepared a 100 ML film which was deposited using the two-step method for the first 10 ML, followed by RT growth at a high deposition rate (4.7 Å/min) for the rest 90 ML. For comparison, a third sample of 100 ML Al was grown on an untreated Si substrate with RT growth and high deposition rate (4.7 Å/min). RHEED patterns, AFM scans, SEM images of slots milled by FIB, and XRD scannings are presented respectively for these three samples in **Fig. 6.11**. According to AFM and SEM images, the surface morphology of 100 ML Al either grown at RT or by the combination of the two-step process and RT growth is as smooth as the one grown by the two-step method (RMS roughness is similar in all films, about 0.24 - 0.26 nm), provided that the film is deposited on a carefully prepared reconstructed Si(111)-(7 × 7) substrate. Sharp, straight slot edges are observed on all epitaxial films (**Fig. 6.11b and c**).

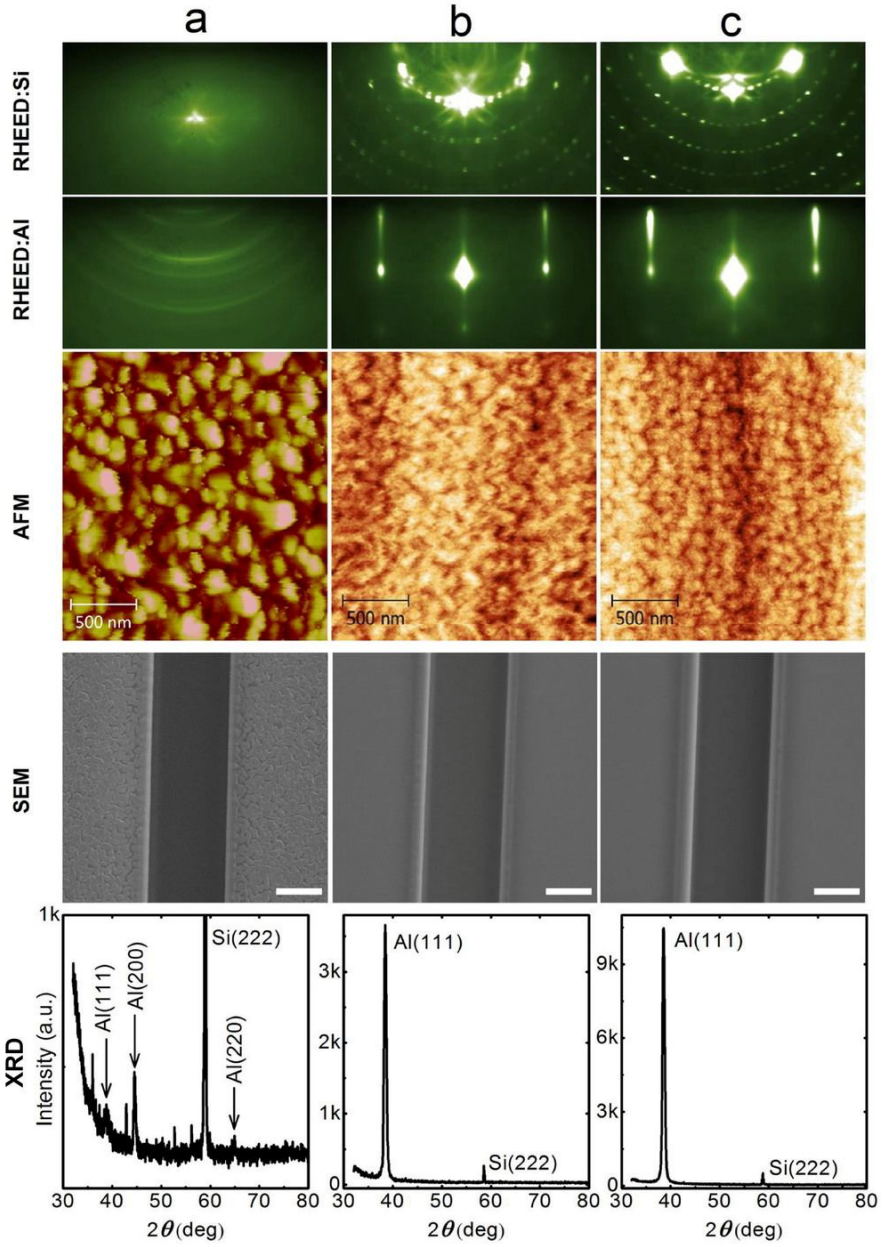

Figure 6.11 **(a)** RHEED pattern of a bare, untreated Si(111) surface, below is the RHEED of a 100 ML Al film deposited on the same Si substrate, grown at RT with a deposition rate of 4.7 Å/min. In the same column, an AFM image (RMS roughness = 6.4 nm), an SEM image of a slot milled by FIB and an XRD 2θ scan profile of this film are shown. **(b)** RHEED of a well-reconstructed Si(111)-(7 × 7) surface. Below is the RHEED of 100 ML

Al deposited at RT with a deposition rate of 4.7 Å/min on this well-reconstructed Si substrate. AFM (RMS = 0.26 nm), SEM image and XRD profile are shown in the same column. **(c)** In the right column, RHEED of a well-reconstructed Si(111)-(7 × 7) surface, RHEED of 100 ML Al deposited by the two-step method (10 ML) followed by an RT growth (90 ML) on this well-reconstructed Si, AFM (RMS = 0.24 nm), SEM, and XRD profile are presented. The Al(111) peak for samples in **(b)** and **(c)** has FWHM of about 0.55°, only 0.05° larger than that of the two-step-grown film. Scale bar on all SEM images: 1 μm.

In contrast, the surface morphology examined by AFM and crystalline quality revealed by XRD are much worse for the Al film grown on an untreated Si substrate. (**Fig. 6.11a**) The ring pattern of RHEED indicates that the film is polycrystalline (See Chapter 3 for the discussion of the interpretation of RHEED data). The RMS roughness is an order higher (6.4 nm) than epitaxial Al films grown on well-reconstructed Si(111)-(7 × 7) surface. The XRD profile on polycrystalline Al shows peaks not only from Al(111), but also from Al(200) and Al(220). The Al(111) peak is much weaker than that from epitaxial films. Despite high roughness with irregular islands from this polycrystalline Al film, interestingly, the slot milled by FIB still shows very straight, sharp edges, without significant difference from those milled on epitaxial Al films. This feature is apparently different from the observation on thermally deposited polycrystalline Al films where the slot edges are irregular with structural defects (**Fig. 6.8f**). We attribute the difference to the presence of a relatively high portion of impurities in the Al source and the hostile chamber environment (a bad vacuum of 10^{-6} Torr) of the thermal deposition equipment compared with our UHV MBE system equipped with a carefully outgassed, clean Al source.

Finally we are going to report the stability of Al films in the atmospheric environment. We note that tiny pinholes observed on thin films (20 ML) grown at RT show a time-dependent evolution when exposed to the air. The size of pinholes enlarges and the

surface roughens after the films stayed in the atmosphere for 20 days (**Fig. 6.12a and b**). Recalling the study of dewetting we discussed in Chapter 5, we notice that dewetting is usually launched around a pit due to a higher mobility of atoms aligning the periphery of the pit. These high-mobile atoms can easily overcome the barrier of migration to the top of the surface, making the enlargement of a pit a thermodynamically preferable process. However, we need to point out a significant difference of Al films from uncapped Ag films - Al films have already been capped by a thin oxide layer, which is assumed to stabilize the film from dewetting. Possibly the oxidation dynamics and the resultant oxide thicknesses along the periphery of a pit and on top of a flat terrace are different. In this scenario the oxide layer around the periphery of a pit might be so thin that atoms aligning the periphery of a pit can sufficiently overcome the migration barrier, which is not only contributed from the step edge of the pit but also from the oxide layer. In comparison, the atomically flat, single-crystalline Al film (10 ML) grown by the two-step method, which is free of pinholes and fissures, shows no deterioration during the time span of observation (which is 20 days in my study, see **Fig. 6.12c**). Interestingly, thicker (100 ML) Al films prepared either by RT growth or the two-step method followed by RT growth show no signs of dewetting after 20 days in the atmosphere, as shown in **Fig. 6.12d and e**. Since both films possess no pinholes, pits or fissures on the surface despite a rougher morphology than a two-step-grown film, there will be no energetically favorable place on the surface to initiate dewetting. Moreover, a relatively smooth surface without rough features such as pits and narrow grooves may improve the uniformity of the oxide layer, which shall better protect the underlying Al film from dewetting. Finally, as expected, the 100 ML Al film grown by the two-step method remains atomically flat after 20 days in the air (**Fig. 6.12f**), demonstrating the film's stability against dewetting in the ambient environment.

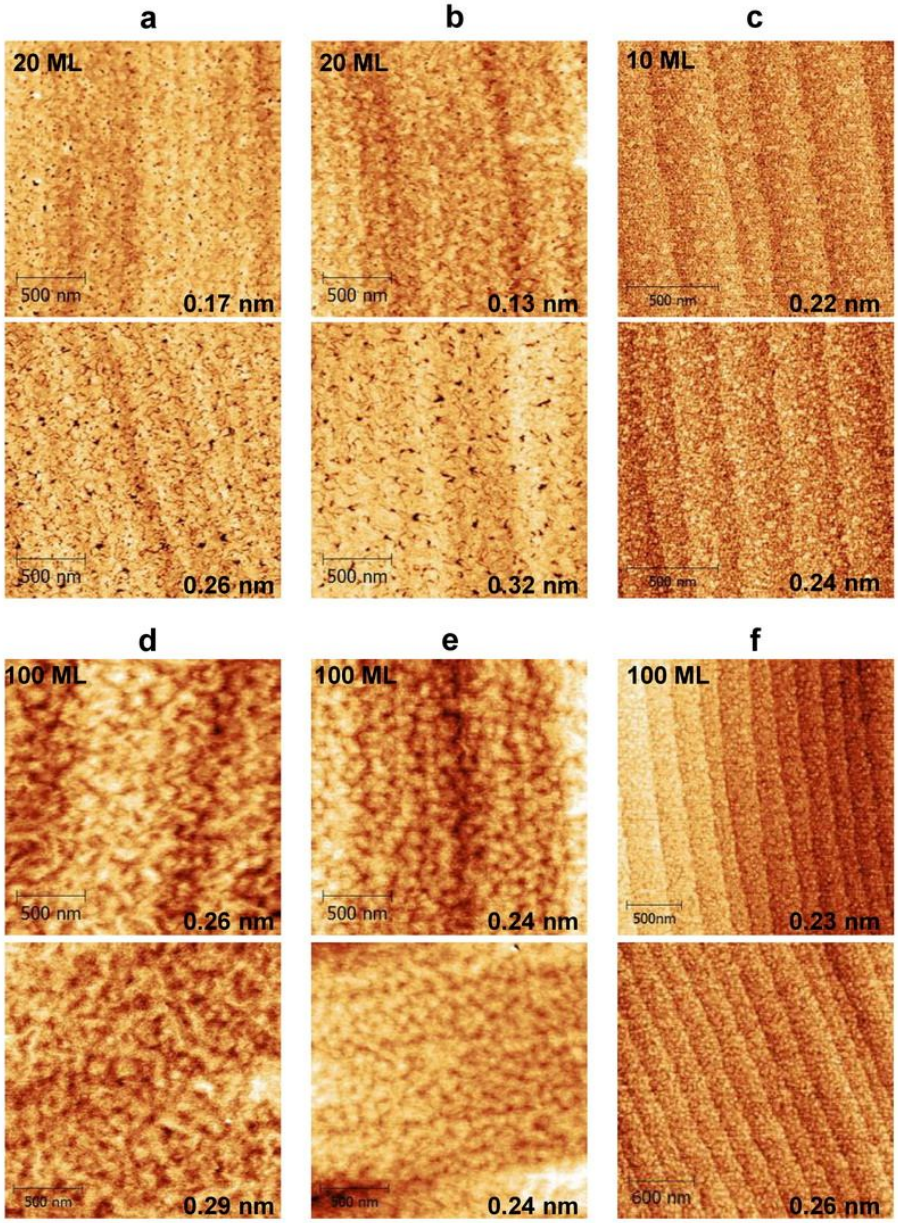

Figure 6.12 AFM images showing the evolution of the surface morphology of the Al film in the atmosphere. Each image in the top panel was taken immediately after the sample was removed from UHV. Each image in the bottom panel was taken on the same sample of the corresponding top panel after the sample was stored in the atmosphere for 20 days. The number at the top left corner of each image on the top panel indicates the thickness of the film. The number at the bottom right corner in every image denotes the RMS

value of the film. **(a)** 20 ML Al deposited at RT with a deposition rate of 4.7 Å/min. **(b)** 20 ML Al deposited at RT with a deposition rate of 6.2 Å/min. **(c)** 10 ML Al by the two-step method. **(d)** 100 ML Al deposited at RT with a deposition rate of 4.7 Å/min. **(e)** 100 ML Al deposited by the two-step method for the first 10 ML Al followed by RT growth (deposition rate = 4.7 Å/min) for the rest 90 ML. **(f)** 100 ML Al grown by the two-step method.

In summary, the two-step method still remains the best recipe to produce atomically smooth epitaxial films while RT growth with a high deposition rate can be utilized to quickly produce relatively smooth epitaxial films with good crystallinity. However, RT-grown films show worse plasmonic response than the two-step-grown films, though they are still better than thermally deposited polycrystalline films. These optical properties will be revealed by spectroscopic ellipsometry measurement, as will be discussed in the next section.

6.2.3 *Spectroscopic Ellipsometry Measurement on Epitaxial Al*

To uncover the intrinsic optical properties of our epitaxial films, we carried out and analyzed spectroscopic ellipsometry (SE) measurement [116, 117] on three such films - the first one is grown by the two-step method, the second one is prepared by RT growth with a high deposition rate (4.7 Å/min), and the third one is grown by the two-step method (first 10 ML) followed by RT growth with a high deposition rate of 4.7 Å/min (the remaining 90 ML). All three samples are epitaxial 100 ML Al (~23.5 nm) films grown on Si(111) with *in-situ* oxidation before removed from UHV. The results from the measurement are plotted against data from Palik's handbook of optical constants. [40] In contrast to Ag films, in which a capping layer is needed to prevent rapid degradation of Ag in ambient environment (see Chapter 5 for detailed discussion), epitaxial Al films can be well protected by a compact, native oxide layer on the surface simply using

our optimally controlled *in-situ* oxidation method. This native oxide layer not only prevents further oxidation, but also acts as a "natural" capping layer to stabilize the underlying film from dewetting. We confirmed, via SE measurement, that once oxidation is completed, the epitaxial Al film's pristine quality and surface smoothness do not change over a period of six months.

In our fitting we use a simple capping/Al/Si structural model for the epitaxial films (**Fig. 6.13a**). Although it is uncertain about the stoichiometry of the oxide layer, we assume it as Al_2O_3 in the model since the optical properties of oxide shall not deviate significantly from those of Al_2O_3. The fitted results for both ε_m' (real part of the dielectric function of Al) and ε_m" (imaginary part of the dielectric function) are plotted against those of a thermally deposited film compiled by Palik, as shown in **Fig. 6.13b and c**. The peak around 1.5 eV (about 800 nm) in **Fig. 6.13b and c** is the result of interband transition (IT) of Al. Outside the IT range, the contribution of ε_m" mainly comes from intraband transitions as well as electron-electron scattering, electron-phonon scattering, and electron scattering due to lattice defects and grain boundaries in the bulk. As a result, electron scattering from lattice defects and grain boundaries in atomically smooth, single-crystalline Al films grown by the two-step process will be expected to be much lower than that of thermal films. Our measurements indeed clearly show substantially lower loss than Palik's values from near-infrared to ultraviolet regime (1.5 eV to 5 eV, **Fig. 6.13c**). The imaginary part of the dielectric function ε_m" extracted from two fast-deposited films (one by one-shot growth at RT and the other by the two-step method followed by RT growth) falls in between the two-step-grown and Palik's values. This observation can be possibly explained by structural defects (voids and pinholes as discussed above) introduced during the deposition at RT. The fitting residues within the whole spectral range are also shown, which are small and centered about zero, suggesting that our model fits

the data very well. In the energy range below 1.5 eV, the errors are relatively large due to reduced detector efficiency.

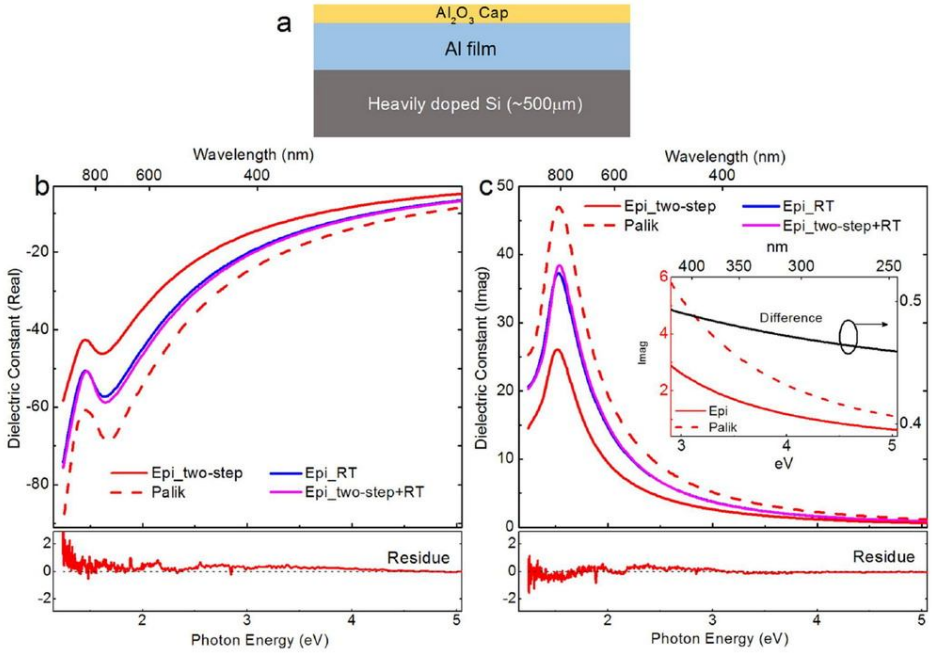

Figure 6.13 **(a)** Layered structure of the Al film with a self-limiting oxide cap. **(b)** Energy dependence of the real part of the dielectric function extracted from the SE measurement on the epitaxial Al film using the two-step growth (red solid), the one deposited at RT (blue solid), and the one deposited using the two-step method for the first 10 ML and RT growth for the following 90 ML (magenta). **(c)** Energy dependence of the imaginary part of the dielectric function extracted from the SE measurement on all three Al films. Both **(b)** and **(c)** are plotted against data taken from Palik's handbook (red dashed line), and the fitting residues for the epitaxial Al film are plotted below **(b)** and **(c)**. The inset in **(c)** highlights the comparison of the intrinsic loss within the UV regime (3 eV – 5 eV) between the two-step epitaxial film and data from Palik's handbook, indicating that the intrinsic loss in the two-step film is about half of Palik's values. The black solid line represents the difference ratio of these two datasets.

The most interesting observation in the SE measurement resides in the UV range (3 eV - 5 eV) where Al outperforms Ag and Au (See **Fig. 2.2b** in Chapter 2). As indicated by the black solid curve in the inset in **Fig. 6.13c**, the intrinsic loss in epitaxial Al by the two-step method is ~ 2 times smaller than Palik's values in the UV range. Our results of much improved, significantly low loss Al films can be very valuable in facilitating the development of UV plasmonics. In addition, out measurement, carried out on high-quality, atomically smooth epitaxial Al films, provides more reliable data on intrinsic optical constants of aluminum. We suggest the inclusion of our newly measured intrinsic optical constants in numerical simulation and theoretical prediction to more accurately guide new device design.

The SE measurement was carried out and analyzed by Junho Choi from Dr. Xiaoqin Li's group and my colleague Dr. Fei Cheng. I express my gratitude to their work.

Chapter 7: Conclusion and Future Work

In this dissertation we reported methods on growing thick, atomically smooth, epitaxial silver (Ag) and aluminum (Al) films for plasmonic research. Single crystallinity and atomic smoothness of our films assure considerable reduction of plasmonic loss. Spectroscopic ellipsometry measurements showed that our atomically smooth epitaxial Ag films have much lower values on the imaginary part of the dielectric function, ε", in the visible wavelength range of the spectrum, compared with widely cited Palik's data. Similarly, our atomically smooth epitaxial Al films possess profoundly lower values of ε" in the ultraviolet regime, up to a factor of 2 with respect to Palik's data extracted from polycrystalline films. Moreover, these high-quality Al films allow reliable measurement of intrinsic optical constants of aluminum. These newly obtained data on Al optical constants from my samples will be essential in describing ultraviolet properties of nanoparticles and nanostructures in a more accurate and comprehensive manner.

For a long time surface scientists heavily relied on the so-called two-step growth (growing the film at a low temperature with a subsequent annealing to room temperature) to prepare atomically flat metal films on semiconductor substrates, However, in the perspective of thick film growth, this method is very inefficient due to a long waiting time of annealing (at least a few hours). The situation will be aggravated if many cycles of growth need to be carried out before achieving the desired thickness. Moreover, the two-step method is best applied in the thin film regime (a few monolayers of the film) in which the quantum size effect is strong and the electronic growth mode determines the atomically smooth surface morphology of the film. Beyond a few single layers, however, the growth mode will be more dominated by kinetic mechanism in which a couple of factors, including the necessity to relieve the strain in the film due to the lattice mismatch

between the film and the substrate, the step barrier, and the mobility of adatoms, will determine the surface morphology of the film. In this scenario the film will usually roll down the path leading to a rough surface. To overcome these problems we designed a variety of growth methods, including rapid deposition at room temperature and rapid deposition at room temperature followed by annealing at an elevated temperature, which successfully achieve the growth of atomically smooth epitaxial films which are much thicker (25 - 150 nm) than the typical two-step films.

In this dissertation we also reported a clean method to oxidize Al films, in which the films are oxidized by high-purity oxygen in an ultrahigh vacuum environment. We showed that the Al films, without further capping, simply oxidized by this *in-situ* method, can retain atomic smoothness in the ambient environment for at least a few months with no sign of dewetting or contamination, assuring the applicability of the films in plasmonics and other research fields such as superconductivity study. In this dissertation we only demonstrated the successful growth of atomically smooth Al films. In the expected near future we shall testify to their performance in UV plasmonic research.

Since we only explored two-step growth and room-temperature growth in this dissertation, other growth conditions with varied deposition temperatures and deposition rates are worth a further effort. Growth on different substrates is another important topic. In this dissertation we only reported films grown on Si(111) because Si(111) wafers are conveniently available and easy to treat, on which the growth of high-quality epitaxial films can be realized. In plasmonics, transparent substrates such as mica might be more attractive because films grown on such substrates can be utilized to carry out transmission studies.

Capping techniques are never a trivial trick. Although in my study a capping layer is mainly for stabilizing the atomically smooth metal films from dewetting in the ambient

environment, capping layers themselves can have far more applications in plasmonics and surface science research. Since it is mostly dielectric materials to be used for the growth of the capping layer, this dielectric layer naturally serves as the spacer in the metal-insulator plasmonic structure. The flatness and uniformity of the dielectric capping layer is thus critical in the performance of plasmonic devices. The capping techniques I reported in the dissertation, such as Al_2O_3/MgO and AlO_x capping methods, can successfully preserve the atomic smoothness of the metal films, and at the same time, serve as an excellent spacer because of their uniformity and transparency to the visible light.

Growing a perfectly uniform, single-atomic spacer of insulator on a metal surface is the "holy grail" for many surface scientists. Once such techniques can be successfully developed, the door to a variety of studies involving light-emitting dye molecules on a metal surface will be opened. Metal causes tremendous quenching to light emission of dye molecules if dye molecules are directly placed on top of metal. If a uniform, single-atomic layer of insulator is laid down between the metal and the dye molecule, the quenching will be largely reduced while the surface plasma of the metal will greatly enhance light emission of the dye molecule. Moreover, since the insulator is only single-atomic in thickness, it allows electron tunneling between the STM tip and the underlying metal, and thus an atomic-scale mapping of the electronic and light-emission properties of dye molecules can be realized by STM. [118 - 121]

Finding appropriate materials and developing techniques to grow a single-atomic insulator film will thus be a critical job in this field. Although the capping methods we reported in the dissertation can successfully protect our atomically smooth metal films, they are all thicker than a single layer in order to completely cover the metal surface. A candidate material for single-layer insulator growth will be silicon. Although Si is semiconductor rather than a truly insulating material, its high resistivity at room and lower

temperatures may already allow it to effectively reduce the quenching by the metal to the light-emitting molecules.

Since we exclusively studied metal films on Si(111), it is natural to conceive the idea of growing Si on metal, which is just the reverse of metal on Si. Specifically, Si on Ag is a promising subject for future research. Ag can perfectly wet the Si substrate although the growth of further coverage of Ag will follow the SK mode due to the lattice mismatch between Ag and Si. However, since the purpose here is only to grow a single-atomic Si layer on Ag, if Si can well wet the Ag surface, the job is very probably achievable. A couple of groups have reported the growth of Si on Ag, in which the structure of the so-called "silicene" of the Si overlayer was extensively studied by STM. However, it seems that most of them did not really realize the growth of a universally uniform single-atomic overlayer of Si on the Ag surface. [122, 123] More efforts shall be invested in this exciting field of research.

Finally, one interesting topic for further study is about the composition and thickness of the Al oxide layer formed on the surface of the atomically smooth Al films by our *in-situ* oxidation method. Although it is not news that there exists a native oxide layer on the surface of bulk Al, the structure of the oxide and the mechanism of the self-limited oxidation process are not very well understood. The stoichiometry and the thickness of the oxide film measured from different groups are a lot of time not in agreement with each other. A major problem among the studies is that the oxide thickness is not uniform due to the rough surface of the sample and possibly not very clean environment during oxidation. Our atomically smooth Al films and clean *in-situ* oxidation method can largely overcome this problem so we believe that the oxide layer on the surface of our atomically smooth Al films shall show atomic-scale uniformity. However, our system is very different from the oxidation taking place on bulk Al. Our Al films are thin (the thickest ones we

studied in this dissertation is only 100 ML) and the electronic properties of the Si substrate, as well as the Al film itself, may play a role in the mechanism of oxidation. Therefore, we cannot directly draw conclusion from the experimental and theoretical studies on bulk Al oxidation to predict the properties of our *in-situ* oxidized Al films. In brief, the stoichiometry, uniformity and thickness of the oxide formed on the surface of our atomically smooth Al films are yet to determine. More experiments shall be conducted to reveal these intriguing properties. Moreover, we did not really know whether 5 ML Al, the thickness of Al in our AlO_x capping method, is completely oxidized or not. All these unsolved issues are worth further effort to explore and such inquiries may provide new insights into the mechanism of Al oxidation in a nanometer scale.

Bibliography

[1] John R. Arthur. Molecular Beam Epitaxy. *Surface Science* 500, **189** (2002)

[2] A.Y. Cho. Morphology of Epitaxial Growth of GaAs by a Molecular Beam Method: The Observation of Surface Structures. *Journal of Applied Physics* **41**, 782 (1970)

[3] A.Y. Cho. GaAs Epitaxy by a Molecular Beam Method: Observation of Surface Structure on the (001) Face. *Journal of Applied Physics* **42**, 2074 (1971)

[4] A.Y. Cho and I. Hayashi. Epitaxy of Silicon Doped Gallium Arsenide by Molecular Beam Method. *Metallurgical Transactions* **2**, 777 (1971)

[5] A.Y. Cho and I. Hayashi. P-N Junction Formation During Molecular Beam Epitaxy of Ge-doped GaAs. *Journal of Applied Physics* **42**, 4422 (1971)

[6] A.Y. Cho and H. C. Casey. GaAs-$Al_xGa_{1-x}As$ Double-Heterostructure Lasers Prepared by Molecular Beam Epitaxy. *Applied Physics Letter* **25**, 288 (1974)

[7] Mohamed Henini (editor). *Molecular Beam Epitaxy: From Research to Mass Production*. 1st Ed. Elsevier Science, MA, USA (2012)

[8] Hung-Ying Chen, Hon-Way Lin, Chang-Hong Shen, and Shangjr Gwo. Structure and Photoluminescence Properties of Epitaxially Oriented GaN Nanorods Grown on Si(111) by Plasma-Assisted Molecular Beam Epitaxy. *Applied Physics Letter* **89**, 243105 (2006)

[9] S. H. Xin, P. D. Wang, Aie Yin, C. Kim, M. Dobrowolska, J. L. Merz, and J. K. Furdyna. Formation of Self-Assembling CdSe Quantum Dots on ZnSe by Molecular Beam Epitaxy. *Applied Physics Letter* **69**, 3884 (1996)

[10] F. Hatami, N. N. Ledentsov, M. Grundmann, J. Bohrer, F. Heinrischsdor, M. Beer, D. Bimberg, S. S. Ruvimov, P.Werner, U. Gosele, J. Heydenreich, U. Richter, S. V. Ivanov, and B. Ya. Radiative Recombination in Type-II GaSb/GaAs Quantum Dots. *Applied Physics Letters* **67**, 656 (1995)

[11] O. Baklenov, D. L. Hu_aker, A. Anselm, D. G. Deppe, and B. G. Streetman. Influence of Al Content on Formation of InAlGaAs Quantum Dots Grown by Molecular Beam Epitaxy. *Journal of Applied Physics* **82**, 6362 (1997)

[12] Hans Luth. *Solid Surfaces, Interfaces and Thin Films*. 5th Ed. Springer, Berlin, Heidelberg, Germany (2010)

[13] Zhenyu Zhang and Max G. Lagally. Atomistic Processes in the Early Stages of Thin-Film Growth. *Science* **276**, 377 (1997)

[14] Arthur R. Smith, Kuo-Jen Chao, Qian Niu, and Chih-Kang Shih. Formation of Atomically Flat Silver Films on GaAs with a "Silver Mean" Quasi Periodicity. *Science* **273**, 226 (1996)

[15] Yiyao Chen, M. W. Gramlich, S. T. Hayden, and P. F. Miceli. The Critical Role of a Buried Interface in the Stranski-Krastanov Growth of Metallic Nanocrystals: Quantum Size Effects in Ag/Si(111)-(7 × 7). *Physical Review Letters* **114**, 035501 (2015)

[16] Pavel Sobotík, Ivan Ošt'ádal, Josef Mysliveček, Tomáš Jarolímek, and František Lavický. Transition from 2D To 3D Growth during Ag/Si(111)-(7 × 7) Heteroepitaxy. *Surface Science* **482** - 485, 797 (2001)

[17] J. Tersoff and F. K. LeGoues. Competing Relaxation Mechanisms in Strained Layers. *Physical Review Letters* **72**, 3570 (1994)

[18] J. Vrijmoeth, H. A. van der Vegt, J. A. Meyer, E. Vlieg, and R. J. Behm. Surfactant-Induced Layer-by-Layer Growth of Ag on Si(111): Origins and Side Effects. *Physical Review Letters* **72**, 3843 (1994)

[19] Erik Cox, Maozhi Li, Po-Wen Chung, C. Ghosh, T. S. Rahman, C.J. Jenks, J. W. Evans, and P. A. Thiel. Temperature Dependence of Island Growth Shapes During Submonolayer Deposition of Ag On Ag(111). *Physical Review B* **71**, 115414 (2005)

[20] Maozhi Li, P.-W. Chung, E. Cox, C. J. Jenks, P. A. Thiel, and J. W. Evans. Exploration of Complex Multilayer Film Growth Morphologies: STM Analysis and Predictive Atomistic Modeling for Ag on Ag(111). *Physical Review B* **77**, 033402 (2008)

[21] Karsten Bromann, Harald Brune, Holger Röder, and Klaus Kern. Interlayer Mass Transport in Homoepitaxial and Heteroepitaxial Metal Growth. *Physical Review Letters* **75**, 677 (1995)

[22] Zhenyu Zhang, Qian Niu, and Chih-Kang Shih. "Electronic Growth" of Metallic Overlayers on Semiconductor Substrates. *Physical Review Letters* **80**, 5381 (1998)

[23] Luca Gavioli, Kevin R. Kimberlin, Michael C. Tringides, John F. Wendelken, and Zhenyu Zhang. Novel Growth of Ag Islands on Si(111): Plateaus with a Singular Height. *Physical Review Letters* **82**, 129 (1999)

[24] C.-S. Jiang, Hongbin Yu, C.-K. Shih, and Ph. Ebert. Effect of the Si Substrate Structure on the Growth of Two-Dimensional Thin Ag Films. *Surface Science* **518**, 63 (2002)

[25] Lin Huang, S. Jay Chey, and J. H. Weaver. Metastable Structures and Critical Thicknesses: Ag on Si(111)-7 × 7. *Surface Science* **416**, L1101 (1998)

[26] Masaru Miyazaki and Hiroyuki Hirayama. Thickness- and Deposition Temperature-Dependent Morphological Change in Electronic Growth of Ultra-Thin Ag Films on Si(111) Substrates. *Surface Science* **602,** 276 (2008)

[27] Hiroyuki Hirayama. Growth of Atomically Flat Ultra-Thin Ag Films on Si Surfaces. *Surface Science* **603**, 1492 (2009)

[28] Hong Liu, Y.F. Zhang, D.Y. Wang, M.H. Pan, J.F. Jia, and Q.K. Xue. Two-Dimensional Growth of Al Films on Si(111)-7 × 7 at Low-Temperature. *Surface Science* **571**, 5 (2004)

[29] Shi-Wei Lin, Jau-Yang Wu, Sheng-Di Lin, Ming-Cheng Lo, Ming-Huei Lin, and Chi-Te Liang. Characterization of Single-Crystalline Aluminum Thin Film on (100) GaAs Substrate. *Japanese Journal of Applied Physics* **52**, 045801 (2013)

[30] Bo-Tsun Chou, Yu-Hsun Chou, Yen-Mo Wu, Yi-Cheng Chung, Wei-Jen Hsueh, Shih-Wei Lin, Tien-Chang Lu, Tzy-Rong Lin, and Sheng-Di Lin. Single-Crystalline Aluminum Film for Ultraviolet Plasmonic Nanolasers. *Scientific Reports* **6**, 19887 (2016)

[31] Ekmel Ozbay. Palmonics: Merging Photonics and Electronics at Nanoscale Dimensions. *Science* **311**, 189 (2006)

[32] Paul R. West, Satoshi Ishii, Gururaj V. Naik, naresh K. Emani, Vladimir M. Shalaev, and Alexandra Boltasseva. Searching for Better Plasmonic Materials. *Laser & Photonics Reviews* **4**, 795 (2010)

[33] Chun-Hsien Chou and Fang-Chung Chen. Plasmonic Nanostructures for Light Trapping in Organic Photovotaic Devices. *Nanoscale* **6**, 8444 (2014)

[34] William L. Barnes, Alain Dereux, and Thomas W. Ebbesen. Surface Plasmon Subwavelength Optics. *Nature* **424**, 824 (2003)

[35] John D. Jackson. *Classical Electrodynamics*, 3rd Ed. John Wiley & Sons, Inc. USA (1999)

[36] Shangir Gwo and Chih-Kang Shih. Semiconductor Plasmonic Nanolasers: Current Status and Perspectives. *Reports on Progress in Physics* **79**, 086501 (2016)

[37] Charlotte E. Sanders. *Tailoring Nanoscale Metallic Heterostructures with Novel Quantum Properties*. Ph.D Dissertation. The University of Texas at Austin (2013)

[38] Stefan A. Maier. *Plasmonics: Fundamentals and Applications*. Springer (2007)

[39] P. B. Johnson and R. W. Christy. Optical Constants of the Noble Metals. *Physical Review B* **6**, 4370 (1972)

[40] Edward D. Palik. *Handbook of Optical Constants of Solids*. Academic Press (1997)

[41] E. Kretschmann and H . Raether. Radiative Decay of Non-Radiative Surface Plasmons Excited by Light. *Zeitschrift für Naturforschung A* **23**, 2135 (1968)

[42] T. W. Ebbesen, H. J. Lezec. H. F. Ghaemi, T. Thio, and P. A. Wolff. Theory of Extraordinary Optical Transmission Through Subwavelength Hole Arrays. *Nature* **391**, 667 (1998)

[43] Bo-Hong Li, Charlotte E. Sanders, James McIlhargey, Fei Cheng, Changzhi Gu, Guanhua Zhang, Kehui Wu, Jisun Kim, S. Hossein Mousavi, Alexander B. Khanikaev, Yu-Jung Lu, Shangjr Gwo, Gennady Shvets, Chih-Kang Shih, and Xianggang Qiu. Contrast Between Surface Plasmon Polariton-Mediated Extraordinary Optical Transmission Behavior in Epitaxial And Polycrystalline Ag Films in The Mid- And Far-Infrared Regimes. *Nano Letters* **12**, 6187 (2012)

[44] J. A. Dionne, L. A. Sweatlock, H. A. Atwater, and A. Polman. Planar Metal Plasmon Waveguides: Frequency-Dependent Dispersion, Propagation, Localization, and Loss Beyond the Free Electron Model. *Physical Review B* **72**, 075405 (2005)

[45] Yanwen Wu, Chendong Zhang, N. Mohammadi Estakhri, Yang Zhao, Jisun Kim, Matt Zhang, Xing-Xiang Liu, Greg K. Pribil, Andrea Alu, Chih-Kang Shih, and Xiaoqin Li. Intrinsic Optical Properties and Enhanced Plasmonic Response of Epitaxial Silver. *Advanced Materials* **26**. 6106 (2014)

[46] R. F. Oulton, V. J. Sorger, D. A. Genov, D. F. P. Pile and X. Zhang. A Hybrid Plasmonic Waveguide for Subwavelength Confinement and Long-Range Propagation. *Nature Photonics* **2**, 496 (2008)

[47] Rupert F. Oulton, Volker J. Sorger, Thomas Zentgraf, Ren-Min Ma, Christopher Gladden, Lun Dai, Guy Bartal, and Xiang Zhang. Plamon Lasers at Deep Subwavelength Scale. *Nature* **461**, 629 (2009)

[48] Y.-J. Lu, J. Kim, H.-Y. Chen, C. Wu, N. Dabidian, C. E. Sanders, C.-Y. Wang, M.-Y. Lu, B.-H. Li, X. Qiu, W.-H. Chang, L.-J. Chen, G. Shvets, C.-K. Shih, and S. Gwo. Plasmonic Nanolaser Using Epitaxially Grown Silver Film. *Science* **337**, 450 (2012)

[49] Yu-Jung Lu, Chun-Yuan Wang, Jisun Kim, Hung-Ying Chen, Ming-Yen Lu, Yen-Chun Chen, Wen-Hao Chang, Lih-Juann Chen, Mark I. Stockman, Chih-Kang Shih, and Shangjr Gwo. All-Color Plasmonic Nanolasers with Ultralow Threshold: Autotuning Mechanism for Single-Mode Lasing. *Nano Letters* **14**, 4381 (2014)

[50] Qing Zhang, Guangyuan Li, Xinfeng Liu, Fang Qian, Yat Li, Tze Chien Sum, Charles M. Lieber, and Qihua Xiong. A Room Temperature Low-Threshold Ultraviolet Plasmonic Nanolaser. *Nature Communications* **5**, 4953 (2014)

[51] Yu-Hsun Chou, Bo-Tsun Chou, Chih-Kai Chiang, Ying-Yu Lai, Chun-Ting Yang, Heng Li, Tzy-Rong Lin, Chien-Chung Lin, Hao-Chung Kuo, Shing-Chung Wang, and Tien-Chang Lu. Ultrastrong Mode Confinement in ZnO Surface Plasmon Nanolasers. *ACS Nano* **9**, 3978 (2015)

[52] Yu-Hsun Chou, Yen-Mo Wu, Kuo-Bin Hong, Bo-Tsun Chou, Jheng-Hong Shih, Yi-Cheng Chung, Peng-Yu Chen, Tzy-Rong Lin, Chien-Chung Lin, Sheng-Di Lin, and Tien-Chang Lu. High-Operation-Temperature Plasmonic Nanolasers on Single-Crystalline Aluminum. *Nano Letters* **16**, 3179 (2016)

[53] Jinfa Ho, Jun Tatebayashi, Sylvain Sergent, Chee Fai Fong, Satoshi Iwamoto, and Yasuhiko Arakawa. Low-Threshold Near-Infrared GaAs-AlGaAs Core-Shell Nanowire Plasmon Laser. *ACS Photonics* **2**, 165 (2015)

[54] Patricia A. Thiel, Mingmin Shen, Da-Jiang Liu, and James W. Evans. Adsorbate-Enhanced Transport of Metals on Metal Surfaces: Oxygen and Sulfur on Coinage Metals. *Journal of Vacuum Science and Technology A* **28**, 1285 (2010)

[55] Patricia A. Thiel, Mingmin Shen, Da-Jiang Liu, and James W. Evans. Coarsening of Two-Dimensional Nanoclusters on Metal Surfaces. *The Journal of Physical Chemistry C* **113**, 5047 (2009)

[56] Mingmin Shen, Da-Jiang Liu, C. J. Jenks, P. A. Thiel, and James W. Evans. Accelerated Coarsening of Ag Adatom Islands on Ag(111) due to Trace Amounts of S: Mass-Transport Mediated by Ag-S Complexes. *The Journal of Chemical Physics* **130**, 094701 (2009)

[57] Charlotte E. Sanders, Chendong Zhang, Gary L. Kellogg, and Chih-Kang Shih. Role of Thermal Processes in Dewetting of Epitaxial Ag(111) Film on Si(111). *Surface Science* **630**, 168 (2014)

[58] H. Oughaddou, S. Vizzini, B. Aufray, B. Ealet, J.-M. Gay, J.-P. Bibérian, and F. A. d'Avitaya. Growth and Oxidation of Aluminum Thin Films Deposited on Ag(111). *Applied Surface Science* **252**, 4167 (2006)

[59] S.Vizzini, H. Oughaddou, J. Y. Hoarau, J. P. Bibérian, and B. Aufray. Growth of Ultrathin Aluminum Oxide on Ag(111). *Applied Physics Letter* **95**, 173111 (2009)

[60] Na Cai and Guangwen Zhou. Tuning the Limiting Thickness of a Thin Oxide Layer on Al(111) with Oxygen Gas Pressure. *Physical Review Letters* **107**, 035502 (2011)

[61] Na Cai, Guangwen Zhou, Kathrin Müller, and David E. Starr. Effects of Oxygen Gas Pressure on the Kinetics of Alumina Film Growth During the Oxidation of Al(111) at Room Temperature. *Physical Review B* **84**, 125445 (2011)

[62] Kevin M. McPeak, Sriharsha V. Jayanti, Stephan J. P. Kress, Stefan Meyer, Stelio Iotti, Aurelio Rossinelli, and David J. Norris. Plasmonic Films can Easily be Better: Rules and Recipes. *ACS Photonics* **2**, 326 (2015)

[63] Hongbin Yu, C. S. Jiang, Ph. Ebert, X. D. Wang, J. M. White, Qian Niu, Zhenyu Zhang, and C. K. Shih. Quantitative Determination of the Metastability of Flat Ag Overlayers on GaAs(110). *Physical Review Letters* **88**, 016102 (2002)

[64] H. Ehrenreich and H. R. Philipp. Optical Properties of Ag and Cu. *Physical Review* **128**, 1622 (1962)

[65] B. R. Cooper, H. Ehrenreich and H. R. Philipp. Optical Properties of Noble Metals. II. *Physical Review* **138**, A494 (1965)

[66] H. Ehrenreich, H. R. Philipp, and B. Segall. Optical Properties of Aluminum. *Physical Review* **132**, 1918 (1963)

[67] Robert LaVilla and H. Mendlowitz. Optical Constants of Aluminum in Vacuum Ultraviolet. *Physical Review Letters* **9**, 149 (1962)

[68] Jisun Kim. *Study of Quantum Thin Films: Phase Relationship, Surface Reactivity, and Coherent Coupling*. Ph.D Dissertation. The University of Texas at Austin (2011)

[69] G. Binnig and C. F. Quate. Atomic Force Microscopy. *Physical Review Letters* **56**, 930 (1986)

[70] Chih-Wen Yang, Ren-Feng Ding, Shih-Hsiu Lai, Hsien-Shun Liao, Wei-Chiao Lai, Kuang-Yuh Huang, Chia-Seng Chang, and Ing-Shouh Hwang. Torsional Resonance Mode Atomic Force Microscopy in Liquid with Lorentz Force Actuation. *Nanotechnology* **24**, 305702 (2013)

[71] Ing-Shouh Hwang, Chih-Wen Yang, Ping-Hsiang Su, En-Te Hwu, and Hsien-Shun Liao. Imaging Soft Matters in Water with Torsional Mode Atomic Force Microscopy. *Ultramicroscopy* **135**, 121 (2013)

[72] Chih-Wen Yang. *Study and Applications of Flexural Mode and Torsional Mode Atomic Force Microscopy*. Ph.D Dissertation. National Taiwan University (2007)

[73] Y. Martin, C. C. Williams, and H. K. Wickramasinghe. Atomic Force Microscope-Force Mapping and Profmng on a Sub 100 Å Scale. *Journal of Applied Physics* **61**, 4723 (1987)

[74] Ricardo Garcia and Alvaro San Paulo. Attractive and Repulsive Tip-Sample Interaction Regimes in Tapping-Mode Atomic Force Microscopy. *Physical Review B* **60**, 4961 (1999)

[75] G. Binnig, H. Rohrer, Ch. Gerber, and E. Weibel. 7 × 7 Reconstruction on Si(111) Resolved in Real Space. *Physical Review Letters* **50**, 120 (1983)

[76] C. J. Chen. *Introduction to Scanning Tunneling Microscopy*. New York: Oxford University Press (1993)

[77] J. Bardeen. Tunnelling From a Many-Particle Point of View. *Physical Review Letters* **6**, 57 (1961)

[78] J. B. Pentry. *Low Energy Electron Diffraction*. Academic Press (1974)

[79] Ayahiko Ichimiya and Philip I. Cohen. *Reflection High Energy Electron Diffraction*. Cambridge University Press (2004)

[80] F Tang, T Parker, G-C Wang, and T-M Lu. Surface Texture Evolution of Polycrystalline and Nanostructured Films: RHEED Surface Pole Figure Analysis. *Journal of Applied Physics D: Applied Physics* **40**, R427 (2007)

[81] Stéphane Andrieu and Patrick Fréchard. What Information can be Obtained by RHEED Applied on Polycrystalline Films? *Surface Science* **360**, 289 (1996)

[82] Dmitri Litvinov, Thomas O'Donnell, and Roy Clarke. In-Situ Thin-Film Texture Determination. *Journal of Applied Physics* **6185**, 2151 (1999)

[83] Thomas Hartsfield, Michael Gegg, Ping-Hsiang Su, Matthew R. Buck, Jennifer A. Hollingsworth, Chih-Kang Shih, Marten Richter, Han Htoon, and Xiaoqin Li. Semiconductor Quantum Dot Lifetime Near an Atomically Smooth Ag Film Exhibits a Narrow Distribution. *ACS Photonics* **3**, 1085 (2016)

[84] Logeeswaran VJ, Nobuhiko P. Kobayashi, M. Saif Islam, Wei Wu, Pratik Chaturvedi, Nicholas X. Fang, Shih Yuan Wang, and R. Stanley Williams. Ultrasmooth Silver Thin Films Deposited with a Germanium Nucleation Layer. *Nano Letters* **9**, 178 (2009)

[85] Deen Gu, Cheng Zhang, Yi-Kuei Wu, and L. Jay Guo. Ultrasmooth and Thermally Stable Silver-Based Thin Films with Subnanometer Roughness By Aluminum Doping. *ACS Nano* **8**, 10343 (2014)

[86] Ben Streetman and Sanjay Banerjee. *Solid State Electronic Devices* (6th edition). Prentice Hall (2005)

[87] Prashant Nagpal, Nathan C. Lindquist, Sang-Hyun Oh, and David J. Norris. Ultrasmooth Patterned Metalsfor Plasmonics and Metamaterials. *Science* **325**, 594 (2009)

[88] Nathan C. Lindquist, Timothy W. Johnson, David J. Norris, and Sang-Hyun Oh. Monolithic Integration of Continuously Tunable Plasmonic Nanostructures. *Nano Letters* **11**, 3526 (2011)

[89] Jong Hyuk Park, Palak Ambwani, Michael Manno, Nathan C. Lindquist, Prashant Nagpal, Sang-Hyun Oh, Chris Leighton, and David J. Norris. Single-Crystalline Silver Films for Plasmonics. *Advancec Materials* **24**, 3988 (2012)

[90] K. Thürmer, E. D. Williams, and J. E. Reutt-Robey. Dewetting Dynamics of Ultrathin Silver Films on Si(111). *Physical Review B* **68**, 155423 (2003)

[91] H. C. Kim, T. L. Alford, and D. R. Allee. Thickness Dependence on the Thermal Stability of Silver Thin Films. *Applied physics Letters* **81**, 4287 (2002)

[92] M. M. R. Evans, B. Y. Han, and J. H. Weaver. Ag Films on GaAs(110): Dewetting and Void Growth. *Surface Science* **465**, 90 (2000)

[93] Karina Morgenstern, George Rosenfeld, and George Comsa. Decay of Two-Dimensional Ag Islands on Ag(111). *Physical Review Letters* **76**, 2113 (1996)

[94] M. Esser, K. Morgenstern, G. Rosenfeld, and G. Comsa. Dynamics of Vacancy Island Coalescence on Ag(111). *Surface Science* **402 - 404**, 341 (1998)

[95] Karina Morgenstern, Georg Rosenfeld, Bene Poelsema, and George Comsa. Brownian Motion of Vacancy Islands on Ag(111). *Physical Review Letters* **74**, 2058 (1995)

[96] L. P. H. Jeurgens, W. G. Sloof, F. D. Tichelaar, and E. J. Mittemeijer. Structure And Morphology of Aluminum-Oxide Films Formed by Thermal Oxidation of Aluminum. *Thin Solid Films* **418**, 89 (2002)

[97] S. Vizzini,, H. Oughaddou, C. Léandri, V. K. Lazarov, A. Kohn, K. Nguyen, C. Coudreau, J.-P. Bibérian, B. Ealet, J.-L. Lazzari, F. Arnaud d'Avitaya, and B. Aufray. Controlled Growth of Aluminum Oxide Thin Films on Hydrogen Terminated Si(001) Surface. *Journal of Crystal Growth* **305**, 26 (2007)

[98] V. Fournée, J. Ledieu, T. Cai, and P. A. Thiel. Influence of Strain in Ag on Al(111) and Al on Ag(100) Thin Film Growth. *Physical Review B* **67**, 155401 (2003)

[99] S. H. Kim, Jikeun Seo, Y. Shin, W. Kim, C. Y. Park, S.-J. Oh, J. M. Seo, H. G. Min, and J.-S. Kim. Initial Growth of Ultrathin Ag Films on an Al(111) Surface. *Physical Review B* **63**, 085414 (2001)

[100] Georg Neuhold and Karsten Horn. Depopulation of the Ag(111) Surface State Assigned to Strain in Epitaxial Films. *Physical Review Letters* **78**, 1327 (1997)

[101] L J Zeng, S Nik, T Greibe, P Krantz, C M Wilson, P Delsing, and E Olsson. Direct Observation of the Thickness Distribution of Ultra Thin AlO_x Barriers in Al/AlO_x/Al Josephson Junctions. *Journal of Physics D: Applied Physics* **48**, 395308 (2015)

[102] J. Evertssona, F. Bertram, F. Zhang, L. Rullik, L.R. Merte, M. Shipilin, M. Soldemo, S. Ahmadi, N. Vinogradov, F. Carlà, J. Weissenrieder, M. Göthelid, J. Pan, A. Mikkelsen, J.-O. Nilsson, and E. Lundgren. The Thickness of Native Oxides on Aluminum Alloys and Single Crystals. *Applied Surface Science* **349**, 826 (2015)

[103] Sung-Min Yoon, Shin-Hyuk Yang, Sang-Hee Ko Park, Soon-Won Jung, Doo-Hee Cho, Chun-Won Byun, Seung-Youl Kang, Chi-Sun Hwang and By-oung-Gon Yu. Effects of ZnO Channel Thickness on the Device Behavior of Nonvolatile Memory Thin Film Transistors with Double-Layered Gate Insulators of Al_2O_3 and Ferroelectric Polymer. *Journal of Physics D: Applied Physics* **42**, 245101 (2009)

[104] Carey M. Tanner, Ya-Chuan Perng, Christopher Frewin, Stephen E. Saddow, and Jane P. Chang. Electrical Performance of Al_2O_3 Gate Dielectric Films Deposited by Atomic Layer Deposition on 4*H*-SiC. *Applied Physics Letter* **91**, 203510 (2007)

[105] H. J. Freund and E. Umbach, *Adsorption of Ordered Surfaces of Ionic Solids and Thin Films*. Springer, Heidelberg (1993)

[106] J. S. Moodera, L. R. Kinder, J. Nowak, P. LeClair, and R. Meservey. Geometrically Enhanced Magnetoresistance in Ferromagnet-Insulator-Ferromagnet Tunnel Junctions. *Applied Physics Letter* **69**, 708 (1996)

[107] R. S. Liu, L. Michalak, C. M. Canali, L. Samuelson, and H. Pettersson. Tunneling Anisotropic Magnetoresistance in Co/AlO_x/Au Tunnel Junctions. *Nano Letters* **8**, 848 (2008)

[108] N. Cabrera and N. F. Mott. Theory of the Oxidation of Metals. *Reports on Progress in Physics* **12**, 163 (1949)

[109] Jakub D. Baran, Henrik Grönbeck, and Anders Hellman. Mechanism for Limiting Thickness of Thin Oxide Films on Aluminum. *Physical Review Letters* **112**, 146103 (2014)

[110] L. P. H. Jeurgens, W. G. Sloof, F. D. Tichelaar, and E. J. Mittemeijer. Growth Kinetics and Mechanisms of Aluminum-Oxide Films Formed by Thermal Oxidation of Aluminum. *Journal of Applied Physics* **92**, 1649 (2002)

[111] C. Lanthony, J. M. Ducéré, M. Djafari Rouhani, A. Hemeryck, A. Estève, and C. Rossi. On the early stage of aluminum oxidation: An Extraction Mechanism via Oxygen Cooperation. *The Journal of Chemical Physics* **137**, 094707 (2012)

[112] Alberto Moscatelli. Plamonics: The Aluminum Rush. *Nature Nanotechnology* **7**, 778 (2012)

[113] Mark W. Knight, Lifei Liu, Yumin Wang, Lisa Brown, Shaunak Mukherjee, Nicholas S. King, Henry O. Everitt, Peter Nordlander, and Naomi J. Halas. Aluminum Plasmonic Nanoantennas. *Nano Letters* **12**, 6000 (2012)

[114] Mark W. Knight, Nicholas S. King, Lifei Liu, Henry O. Everitt, Peter Nordlander, Naomi J. Halas. Aluminum for Plasmonics. *ACS Nano* **8**, 834 (2014)

[115] Bob Y. Zheng, Yumin Wang, Peter Nordlander, and Naomi J. Halas. Color-Selective and CMOS-Compatible Photodetection Based on Aluminum Plasmonics. *Advanced Materials* **26**, 6318 (2014)

[116] James N. Hilfiker, Neha Singh, Tom Tiwald, Diana Convey, Steven M. Smith, Jeffrey H. Baker, and Harland G. Tompkins. Survey of Methods to Characterize Thin Absorbing Films with Spectroscopic Ellipsometry. *Thin Solid Films* **516**, 7979 (2008)

[117] Craig M. Herzinger, and Blaine D. Johs. *Dielectric Function Parametric Model, and Method of Use*. Google Patents (1998)

[118] Elizabeta Ćavar, Marie-Christine Blüm, Marina Pivetta, François Patthey, Majed Chergui, and Wolf-Dieter Schneider. Fluorescence and Phosphorescence from Individual C_{60} Molecules Excited by Local Electron Tunneling. *Physical Review Letters* **95**, 196102 (2005)

[119] S. W. Wu, N. Ogawa, and W. Ho. Atomic-Scale Coupling of Photons to Single-Molecule Junctions. *Science* **312**, 1362 (2006)

[120] Chi Chen, Ping Chu, C. A. Bobisch, D. L. Mills, and W. Ho. Viewing the Interior of a Single Molecule: Vibronically Resolved Photon Imaging at Submolecular Resolution. *Physical Review Letters* **105**, 217402 (2010)

[121] S. W. Wu and W. Ho. Two-Photon-Induced Hot-Electron Transfer to a Single Molecule in A Scanning Tunneling Microscope. *Physical Review B* **82**, 085444 (2010)

[122] Daniele Chiappe, Carlo Grazianetti, Grazia Tallarida, Marco Fanciulli, and Alessandro Molle. Local Electronic Properties of Corrugated Silicene Phases. *Advanced Materials* **24**, 5088 (2012)

[123] Junki Sone, Tsuyoshi Yamagami, Yuki Aoki, Kan Nakatsuji, and Hiroyuki Hirayama. Epitaxial Growth of Silicene on Ultra-Thin Ag(111) Films. *New Journal of Physics* **16**, 095004 (2014)